PhD-FSTM-2025-082
The Faculty of Science, Technology and Medicine

DISSERTATION

Defence held on 01/08/2025 in Luxembourg

to obtain the degree of

DOCTEUR DE L'UNIVERSITÉ DU LUXEMBOURG

EN *Physique*

by

Alba Viejo Rodríguez

Born on 15th July 1996 in Langreo, (España)

ULTRAFAST OPTOACOUSTICS ON MULTIFUNCTIONAL CAVITIES

Dissertation defence committee

Dr Daniele Brida, dissertation supervisor
Professor, Université du Luxembourg

Dr Andreas Michels, Chairman
Professor, Université du Luxembourg

Dr Paolo Vavassori
Group leader, CIC nanoGUNE

Dr Michele Celebrano
Professor, Politecnico di Milano

Dr Crina Cojocaru
Professor, Universitat Politècnica de Catalunya

“Pensando la Regenta en aquella niña que había sido ella, la admiraba y le parecía que su vida se había partido en dos, una era la de aquel angelillo que se le antojaba muerto. La niña que saltaba del lecho a obscuras era más enérgica que esta Anita de ahora, tenía una fuerza interior pasmosa para resistir sin humillarse las exigencias y las injusticias de las personas frías, secas y caprichosas que la criaban”

— *Leopoldo Alas Clarín, La Regenta*

Contents

Acknowledgments

When I first arrived in Luxembourg, I was eager to start this PhD. In the end, following my will to do this was the one and only motivation for moving out of Spain. Suddenly, within the first weeks, I thought how lucky I was to be so welcomed and surrounded since my day of arrival, and I slowly started to understand how important your surroundings, your friends, or just a place are in order to successfully finish a PhD. In fact, they are what saved me from failing on numerous occasions.

I want to be fair to myself and keep the acknowledgments quite raw and real, with no sugarcoating and no empty gratitude messages just for compromise or academic diplomacy. I daydreamed so many times about finishing the thesis, imagining how I would feel and how grateful I would be for my supervisor, who I always thought I would portray as a mentor. Well, I guess that was always just a daydream, since the reality was quite far from my probably naive idea of being a scientist. I experienced and witnessed what I thought was the dark side of science, but what I later learned to be the norm: disdain, shouting, mockery, sexism, racism... and a long list of personal experiences that, without a doubt, will always live with me. These contributed to making me see science in a disgusting way, far from its real purpose of finding solutions to natural questions, and more like a rude (mainly) male ego competition with no morals or ethics.

Usually, when reading thesis acknowledgments, I see how people feel grateful (or at least that is what they write) for their host institution, their supervisors, or their grants. Again, I guess you will have to imagine those parts, since very few words of gratitude come to my mind.

Do not get me wrong, I do not think the whole scientific world is rotten, or I would not like to think so. There have always been a few people in my mind who kept me believing there is still some hope. I would like to thank them, as I see them as references. I would like to start with

Prof. Pablo Alonso González, who gave me the chance to work in his lab during my bachelor thesis and made me see research as something exciting, which strongly contributed to my decision to pursue a PhD. Along with him, I met Gonzalo, who has accompanied me throughout these four years, the person who actually found the open position in Luxembourg and persuaded and helped me to get the opportunity. He has been personally very important to me and someone I have always admired as a scientist. Finally, Markus, who I now consider a good friend but was once just a postdoc in the group, he represents all the good things science should mean and gave me hope that there are still good people in this field.

I would not like readers to think this was just a disastrous experience. Hopefully, I can also show that during these years I met amazing people who made these four years worth leaving my beautiful region, Asturias.

I would like to thank my colleagues with whom I shared frustrations and challenges, but who, with time, also became good friends. Kilian, who closely followed me during my early PhD years and who without doubt helped shape me into the scientist I am today. Thomas, whose way of working and patience I have always admired, and who made me realize that friendship between a German and a Spanish was possible. Ricardo, whose warmth made the group feel like an actual group rather than just people sharing a workspace. I have always described you to others as peculiar, but in the most positive way one can imagine, showing me kindness and affection. Lastly, I would like to thank the rest of the people, even though we didn't spend much time together: in particular, Pirmin, Majdi, Armel, and Kosmas. To you and all the new members of the group, I wish you all the best.

Almost in my last year of the PhD, I had the amazing chance to visit another university located in what I would describe as "almost the North Pole", Umeå, Sweden. There I reunited with my favourite Chinese, Tlek, and together with Lucrezia they accompanied me during those three months, which were probably some of the most difficult times of my PhD. I would also like to thank all the people I met there who were always really nice: Susu, Sajjad, Daniel, Nils and all the members of the group.

When I think about the people I met during these years at the university, Shameek and Ashik always come to my mind. They welcomed me from the first week I joined, inviting me to every type of event and introducing me to so many people. They contributed to making these years quite fun. Xu and Najiya, who were always a joy to meet and with whom I shared many PhD frustrations, also provided me with a lot of moral support.

During these years abroad I also had a bit of Spain (or Madrid) in Luxembourg. Many of my memories here are with you guys: Jaime, Pablo, Sergio, Edu, Miguel, Arias, Pablito... but I would like to give a special mention to the girls, Ana, Palo, and Cris. From all of them, Javi and Yael were my biggest support and the reason I can call Luxembourg my home. I already miss seeing you every day at home for dinner and our daily podcast. A todos vosotros, chicos, gracias. Me siento afortunada de que la vida nos haya juntado y hayamos disfrutado estos años juntos. Espero vernos pronto.

Being in Luxembourg gave me the chance to meet people from places I would otherwise never have interacted with. Especially Deniz and Ahmet, whose warmth reminded me of what I like to think Spanish people are. With you I discovered new music, had fun, and felt we were from the same place, even though our mother tongues were different, I guess that is the Mediterranean alliance. The same with Viola, probably the most caring person I have met, always gathering people for home-cooked food. Thank you for always worrying and taking care of me. Julia, a more recent but funny addition to my international friends, I guess it was easier with you, since I consider you more Asturian than Argentinian. I also do not want to forget about Luca, Andrea, Eléonore, María, Anne...

Parte de mí nunca ha abandonado Asturias, sin duda gracias a la gente que siempre está ahí cada vez que vuelvo, aunque solo sea una vez al año. Tengo la suerte de poder presumir de amistades de la infancia, de hace tantos años, que me han visto crecer y que me conocen demasiado bien. Blanca, siento que siempre hemos crecido juntas. El mismo día que me mudé a Luxemburgo tú también lo hacías a Múnich. Me alegra poder seguir cada cambio a tu lado a pesar del tiempo y la distancia. Jesús, Aida y Lucía, quienes probablemente más me hayan escuchado quejarme estos años, muchas veces sin saber qué decir, pero que siempre han sido un apoyo enorme. Con vosotros me sigo riendo de las mismas tonterías que hace años, como si el tiempo no pasara, aunque ahora tengamos que afrontar la vida adulta.

Me gustaría también agradecer a mis padres, Rosa María y José Luis, que, aunque muchas veces desde el miedo a lo desconocido hayan dudado de mis decisiones, siempre me han acompañado y se han preocupado por darme todo lo mejor.

Finally, I would like to thank Andrea, who has been not only one of the best colleagues but also mi compañero de vida. Thank you for holding my hand in my weakest moments, for always being by my side, for your patience, and for trusting on me even more than I trust myself. I truly feel that meeting you has made me a better person and has filled my life with joy.

1

Introduction

Controlling solid-state systems can be achieved by addressing different microscopic degrees of freedom, such as electronic charges, lattice vibrations (phonons), or spins. Each of these subsystems interacts on characteristic timescales and can be selectively excited using modern ultrafast optical techniques [1]. This thesis is particularly concerned with the excitation of lattice vibrations and their subsequent coupling to spin dynamics in magnetic materials.

The ability to control magnetism at ultrafast timescales is not only of fundamental interest but also of high technological relevance. Magnetic order underpins a wide range of applications across medicine, chemistry, and biology, from imaging techniques to biosensors. However, the focus here is on the technological implications for data storage devices, including hard-disk drives and magnetic random-access memories (MRAMs). These devices form the backbone of our digital society, where the demand for data storage continues to grow at an unprecedented pace. Current projections estimate that the global data volume will reach values on the order of 175 zettabytes (10^{21} bytes) within the next few years. This rapid increase in stored information has been addressed by constructing ever larger data centers. While effective in the short term, this approach is neither sustainable nor efficient: data centers consume vast amounts of energy, and their demand continues to rise faster than improvements in energy efficiency. Thus, a fundamental challenge emerges, how to design faster and more energy-efficient data storage technologies that can meet the needs of a data-driven world.

Magnetic recording technologies provide an appealing path forward. Today, typical read/write times in magnetic devices are on the order of $\sim$10 ns. However, from the perspective of solid-state physics, this limitation is technological rather than fundamental. Spin dynamics in magnetic materials can occur on picosecond timescales (1–100 ps), orders of magnitude faster than current devices can exploit. Overcoming this gap requires novel approaches to manipulate magnetic order at ultrashort timescales. The central idea that motivates this thesis is to achieve control of the magnetic order of solids via their lattice vibrations. Ultrafast lasers offer a unique tool in this regard: by generating coherent acoustic phonons, one can couple elastic deformations to the spin system and potentially manipulate magnetization at picosecond timescales [2]. This approach promises not only to deepen our understanding of spin–lattice interactions but also to pave the way for new concepts in ultrafast magnetic data storage and processing. In this context, the work presented here investigates the acoustic response of magnetic materials under ultrafast optical excitation, with the aim of exploring and exploiting the interplay between lattice vibrations and spin dynamics.

Understanding and controlling the interaction between light and matter lies at the heart of many advances in modern physics and technology. Over the past decades, the development of ultrafast laser sources has enabled researchers to explore these interactions at their natural timescales, opening new horizons in fields as diverse as quantum optics, condensed matter physics, and nanoscale imaging. Femtosecond and picosecond lasers have made it possible not only to probe the elementary processes that govern electron, phonon, and spin dynamics, but also to manipulate these excitations with remarkable precision. Among these phenomena, opto-acoustics—the study of how light can generate, detect, and modulate sound waves at ultrafast timescales—has emerged as a particularly active field, where a plethora of fundamental processes can be harnessed to address a broad range of possible applications . When short laser pulses are absorbed in a material, they induce transient thermal and electronic stresses that launch coherent acoustic phonons. These GHz–THz strain waves, confined within nanostructured geometries, serve as both diagnostic tools and active components in hybrid photonic–acoustic systems. The ability to generate and control such acoustic waves offers opportunities for ultrafast signal processing, high-resolution sensing, and even strain-assisted magnetization control in magnetic materials. At the same time, nanostructuring of materials offers a powerful strategy to tailor the propagation, damping, and coupling of these acoustic modes. By modifying the geometry, composition, and boundary conditions of a structure—for example by detaching a thin film from its substrate or incorporating it into a metal–insulator–metal (MIM) architecture—it is possible to significantly alter its opto-acoustic response. These engineered nanocavities provide unique platforms to study multiphysics coupling between photons, phonons, and possibly magnons, with implications for the development of next-generation functional materials and devices.

This thesis investigates the ultrafast acoustic response of nanostructured metal systems, with a focus on two model platforms: being the first polycrystalline freestanding nickel cavities fabricated via laser delamination, and the second MIM cavities supporting optical epsilon-near-zero (ENZ) modes. In both systems, femtosecond pump–probe spectroscopy is used to excite and monitor acoustic resonances with sub-picosecond resolution. Through a combination of time-domain measurements, Fourier analysis, and numerical simulations, we extract the key parameters governing acoustic lifetimes, confinement, and energy dissipation. In parallel to these core studies, this work also explores a complementary project in the field of optical biosensing. Specifically, we present the design and optical characterization of a Segmented Refractive Optical Element (SROE) intended for use in ultrafast Raman-based protein sequencing. While distinct in application, this component shares with the rest of the thesis a common reliance on custom-designed optics and nonlinear light–matter interactions, illustrating the versatility of ultrafast optics tools across different scientific domains.

Altogether, the results presented in this thesis contribute to a deeper understanding of how ultrafast laser pulses interact with structured matter, both from a fundamental perspective and with a view towards enabling future applications in magneto-acoustics, integrated photonics, and biophotonics.

Outline of this work

This thesis is organized into seven chapters that progressively build on the physical concepts, experimental methods, and analytical tools used to investigate light–matter interactions in these multifunctional nanostructures.

In **Chapter 2**, we introduce the theoretical and experimental background of ultrafast opto-acoustic phenomena, focusing on the generation and detection of coherent acoustic phonons in solids, in particular metals. We discuss how nanostructuring methods, such as the fabrication of suspended cavities, can be used to tailor acoustic damping and confinement. Particular emphasis is placed on the interplay between acoustics, optics, and magnetism, laying the groundwork for exploring multi-physics platforms like magneto-acoustic resonators.

Chapter 3 provides an in-depth overview of the ultrafast optical techniques employed throughout this work. We describe the principles of pump–probe spectroscopy and nonlinear optical processes such as second- and third-harmonic generation and white light generation. Optical parametric amplifiers (OPAs), used as tunable sources in both the visible and near-infrared range, are introduced along with a custom-designed experimental setup tailored for femtosecond time-resolved spectroscopy.

In **Chapter 4**, we present a detailed study of the acoustic response of freestanding nickel cavities fabricated using laser delamination, a novel fabrication method that could potentially substitute expensive and time-consuming litographic techniques for nanopatterning. These structures are compared to nickel films in direct contact with the substrate. The acoustic dynamics are characterized using pump–probe spectroscopy and analyzed through Fourier transform techniques, while finite-element simulations are employed to interpret the observed behavior in terms of resonant modes and quality factors. Our analysis demonstrates the superior performance of the free-standing cavities, providing first evidence that the laser delamination technique is a viable alternative for next-generation opto-acoustic resonators. Moveover, controlling the propagation of acoustic pulses in a material like nickel is a necessary first step towards a laser-driven control of magnetic states on ultrafast timescales.

Chapter 5 extends the investigation to a different class of structures—metal–insulator–metal (MIM) cavities. These systems support epsilon-near-zero (ENZ) modes that enhance optical field confinement, providing an interesting platform for the generation and propagation of acoustic phonons. Again, pump–probe spectroscopy is used to probe the system's response, with comparisons drawn to the behavior observed in the nickel cavities.

Chapter 6, we shift focus to a complementary project that intersects with photonics and molecular biology. This chapter discusses the design, fabrication, and optical characterization of a Segmented Refractive Optical Element (SROE), a custom optical component developed for ultrafast Raman-based amino acid sequencing. This work forms part of a larger HORIZON 2020 collaboration and highlights the role of optics in emerging biotechnological applications.

Chapter 7 summarizes the main findings of the thesis, reflecting on their broader implications for the development of multifunctional nanodevices and outlining future directions for research at the intersection of optics, acoustics, and magnetism.

2

Light-matter interaction in multifunctional nanostructures

The ability to detect and control the properties of light beams is at the heart of state-of-the-art technologies in a variety of fields, such as telecommunications, sensing, imaging and characterization of novel materials. In particular, significative efforts are being made towards the development of miniaturized optical components able to manipulate light at the nanoscale, potentially paving the way for more efficient and more performant next-generation devices.

This chapter builds the foundational context for interpreting the acoustic dynamics reported later in this thesis, especially in the case studies of nickel opto-acoustic cavities and epsilon-near-zero (ENZ) metal-insulator-metal (MIM) resonators presented in Chapter 4 and Chapter 5, respectively. These discussion is based on several review works on photoacoustics, more in particular in acoustic phonons generated by ultrafast laser action [3], [4], and will provide as well a context for future promising technologies relaying on the combination of opto-acoustics with magnetic systems [5].

2.1 Principles and applications of ultrafast opto-acoustics

The development of pulsed laser sources has enabled the study of ultrafast light-induced coherent acoustic phonons (CAPs), which has become a significant area of research in condensed matter physics and ultrafast optics.

When an ultrashort laser pulses is absorbed by a material, the spatio-temporal characteristics of the resulting acoustic waves generated no longer depend on the pulse duration. Instead, the dynamics are limited by the characteristic timescales of energy transfer within the medium, for example on the order of a few ps for electron-phonon scattering, and by the volume over which this transfer occurs, generally constrained by the material's optical penetration depth, here referred as ξ [6]. As a result, coherent strain pulses can be generated using a pump laser pulse with time durations shorter than a picosecond, such as the 220 fs pulses used in this work. The detection of the resulting mechanical perturbation is typically performed using a time-delayed probe pulse, monitoring the transient reflectivity (or transmittivity) of the sample. This pump–probe scheme, wherein a femtosecond pump pulse excites the system and a probe pulse reads the response via changes in reflectivity or transmittivity, is discussed in detail in Chapter 3, Section 3.1.

The ability to optically excite and detect coherent acoustic phonons in solids opens the door to a wide range of applications, particularly in the micro-electronics and opto-mechanical industries. CAP generation and propagation have been extensively studied in metals [7], semiconductors [8] and quantum wells [9]. This thesis focuses on metallic nanostructures and multilayered systems, where the geometry and boundary conditions strongly influence the acoustic dynamics.

In metals, the interaction with a femtosecond laser pulse is highly localized within the first 20 to 30 nm beneath the surface. After absorbing a photon, electrons occupy a strongly out-of-equilibrium state, reaching temperatures of several thousand kelvin within a few hundred femtoseconds, while the lattice remains initially unaffected [10]. To describe this process, the Two-Temperature Model (TTM) [11] provides a quantitative robust framework to explore the subsequent dynamics of energy transfer between these subsystems [12]. The electrons temperature $T_e(z,t)$ (with z indicating the penetration coordinate within the material) then relaxes by transferring energy to the lattice, which responds in a slower way increasing its temperature $T_l(z,t)$ on a picosecond timescale. The coupled differential equations governing these dynamics are:

$$C_e(T_e)\frac{\partial T_e}{\partial t} = -G(T_e - T_l) + S(z,t) \tag{2.1}$$

$$C_l\frac{\partial T_l}{\partial t} = G(T_e - T_l) \tag{2.2}$$

where C_e and C_l are the electronic and lattice heat capacities, G is the electron-phonon coupling constant and $S(z,t)$ represents the energy source term from the absorbed laser pulse. This rapid, non-equilibrium heating generates a transient stress field $\sigma(z,t)$ in the material. In metals, the total stress is composed of two main contributions [13]:

$$\sigma(z,t) = \gamma_e C_e \Delta T_e(z,t) + 3B\beta\Delta T_l(z,t) \tag{2.3}$$

The first term ($\sigma_e(z,t)$) arises from the electronic pressure, dominant in the sub-picosecond regime, while the second term $\sigma_l(z,t)$ corresponds to the thermoelastic stress due to delayed lattice heating and thermal expansion. Here, γ_e is the electronic Gr*ü*neisen parameter, B the bulk modulus and β the thermal expansion coefficient.

These stresses launch coherent strain waves $\eta(z,t)$, which propagate through the material at the longitudinal sound velocity C_a. For a cavity, for example a thin metallic film on top of a substrate, the strain waves reflects at interfaces, forming acoustic echoes. These echoes can be detected optically due to their effect on the dielectric function ϵ, via the photoelastic effect and surface displacement. In time-domain measurements, the result is a periodically modulated reflectivity (or transmittivity) signal. For simple geometries, such as thin films or slabs, the CAP dynamics can be described by the one-dimensional inhomogeneous wave equation:

$$\frac{\partial^2 u}{\partial t^2} - C_a^2 \frac{\partial^2 u}{\partial z^2} = \frac{1}{\rho} \frac{\partial \sigma(z,t)}{\partial z} \tag{2.4}$$

The resonant eigenfrequencies of the longitudinal confined acoustic modes in a film of thickness H are given by:

$$f_n = \frac{C_a}{2H} n, \quad n = 1, 2, 3, \ldots \tag{2.5}$$

Figure 2.1 illustrates the spatio-temporal evolution of a coherent acoustic pulse in a metallic thin film excited by an ultrashort laser pulse. Following the optical pump absorption near the surface (within the optical penetration depth), a localized thermal stress is generated. This launches a broadband acoustic strain pulse that propagates through the material. The schematic shows how the wave packet travels, reflects at the material/substrate interface, and gives rise to oscillatory strain fields confined within the film. The degree of reflection or transmission at the film–substrate boundary plays a critical role in determining the damping of the acoustic modes, which we explore in more detail in the following chapters through both experimental and numerical analyses.

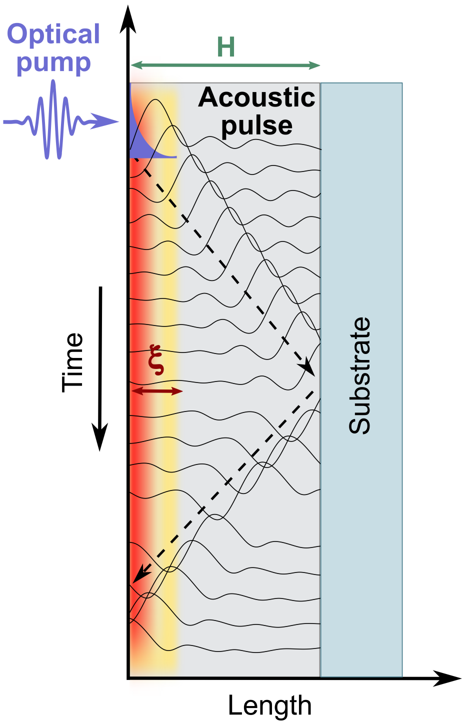

Figure 2.1: *Schematic representation of coherent acoustic phonon generation and propagation in a thin film upon femtosecond optical excitation. An ultrafast pump pulse is absorbed near the surface of the film, leading to a sudden temperature rise and subsequent stress profile (ξ is the typical distance over which the absorbed pump energy is deposited). This triggers the generation of an acoustic pulse that propagates, with a sound velocity C_a, through the film thickness H and reflects at the substrate interface. The dashed black line represent the propagation direction of the strain wavefront, while the solid black lines show the evolving strain distribution over time. Figure adapted from [14].*

These theoretical concepts form the physical foundation for the experiments and analysis presented in the following chapters. In particular, they are crucial for understanding the behavior of confined acoustic phonons in freestanding nickel cavities and MIM (metal–insulator–metal) structures, whose acoustic responses are analyzed through Fourier-transform techniques.

2.2 Structuring in opto-acosustic coupling

Micro and nanostructuring plays a pivotal role in tailoring opto-acoustic coupling, allowing for unprecedented control over the generation, propagation, and detection of coherent acoustic phonons. When ultrafast laser pulses interact with structured metals, the confinement and geometric modulation of the structure strongly affect both the spatial profile of the generated acoustic waves and their spectral content.

At the nanoscale, the absorption of femtosecond pump pulses in confined geometries—such as thin films, suspended membranes, or multilayered structures leads to non-equilibrium electronic heating and subsequent stress generation localized within tens of nanometers of depth. This generates a localized strain profile capable of launching GHz–THz broadband acoustic wavepackets into the structure and surrounding media [15]. In particular, ultrafast photoacoustics in metallic structures such as the ones discussed in this thesis, leverages geometric confinement to support discrete acoustic eigenmodes. These structures act as optical-acoustic resonators, where the interplay between structural thickness, acoustic impedance mismatch at interfaces, and reflection conditions (total or partial reflection) determines the modal landscape and damping characteristics.

The introduction of periodic or confined nanostructures [16], such as nano-disks, nano-cubes, or phononic lattices—introduces additional coupling mechanisms through hybridization and collective behavior. For instance, 2D phononic crystals made from aluminum nano-cubes on a metallic substrate have shown to support guided collective modes at frequencies up to 8 GHz, mimicking the acoustic phonon modes of atomic lattices [17]. Moreover, indirect opto-acoustic transduction is enabled by photoexcitation of vibrational modes in individual nanoparticles, such as gold nanorods or disks, which can then couple their motion to the surrounding substrate, launching propagating bulk or surface acoustic waves [18]. These effects are particularly important for high-frequency sensing, imaging, and signal processing applications, where control over wave directivity, localization, and coupling is crucial.

In nickel structures, such as the cavities studied in this thesis, the geometry and boundary conditions significantly alter the acoustic mode spectrum and lifetime. The removal of the substrate in suspended geometries enhances the reflection at the metal/air interface, possibly reducing acoustic damping and increasing the lifetime of phonon modes, factors directly verified in Chapter 4 using Fourier analysis and multiphysics simulations. In metal-insulator-metal (MIM) cavities, nanostructuring enables the coexistence of photonic and phononic modes within a confined architecture, supporting multi-physical interactions such as photon–phonon coupling and potential magneto-acoustic coupling when combined with ferromagnetic metals. These structures not only enhance the generation of strain waves but also offer control over the detection sensitivity via cavity-enhanced reflectivity changes, as outlined in multi-layer interface reflectivity studies such as the one presented in Chapter 5.

Such capabilities make nanostructured systems highly promising for advanced GHz optomechanical devices, non-destructive testing, surface acoustic wave filtering, and magneto-opto-acoustic phenomena.

2.3 Towards multi-physics cavities

As briefly mentioned in the previous section, coupling of acoustic pulse with magnetic material platforms offers interesting opportunities towards light-driven magnetization control. In general, magneto-optics studies the interaction of light with magnetic systems, often leading to modifications in both the magnetic and optical properties of the medium. A classic example is the Faraday rotation, where linearly polarized light experiences a rotation of its polarization plane when transmitted through a ferromagnetic material [19]. This phenomenon arises because circularly polarized components with opposite helicity experience different refractive indices in a magnetized medium. Similarly, the magneto-optical Kerr effect (MOKE) describes polarization rotation for reflected light [20], widely used in ultrafast magneto-optical studies of thin films and nanostructures.

Importantly, magneto-optics is not only about probing magnetization but also about controlling it. In a seminal study, Beaurepaire et al. showed that ultrashort laser pulses can transiently alter the magnetic state of nickel, initiating the field of ultrafast magnetism [21]. These results opened promising routes for developing optically driven memory and logic devices operating at femtosecond timescales and offering potential breakthroughs in data processing speed and energy efficiency.

From a fundamental perspective, magneto-optical dynamics involve a variety of physical processes including electron–phonon coupling, incoherent heating, coherent spin-wave excitation, and angular momentum transfer [22], [14]. These mechanisms operate on overlapping timescales, making it challenging but essential to disentangle them for technological advancement. However, the major bottleneck remains the typically weak magnitude of magneto-optical signals, with Kerr rotations often in the milliradian range. To overcome this, one strategy is to enhance light–matter interactions by integrating magnetic systems with plasmonic or dielectric nanostructures, which increase local field intensities and introduce new coupling channels [23]. In this context, magneto-acoustic cavities emerge as an exciting class of multi-physics platforms. The freestanding nickel structures fabricated and analyzed in this thesis together with metal-insulator-metal (MIM) architectures are promising candidates for strain-assisted magnetization control. Femtosecond laser pulses absorbed in the metal generate coherent acoustic phonons, which propagate through the structure and modulate the magnetization via inverse magnetostriction.

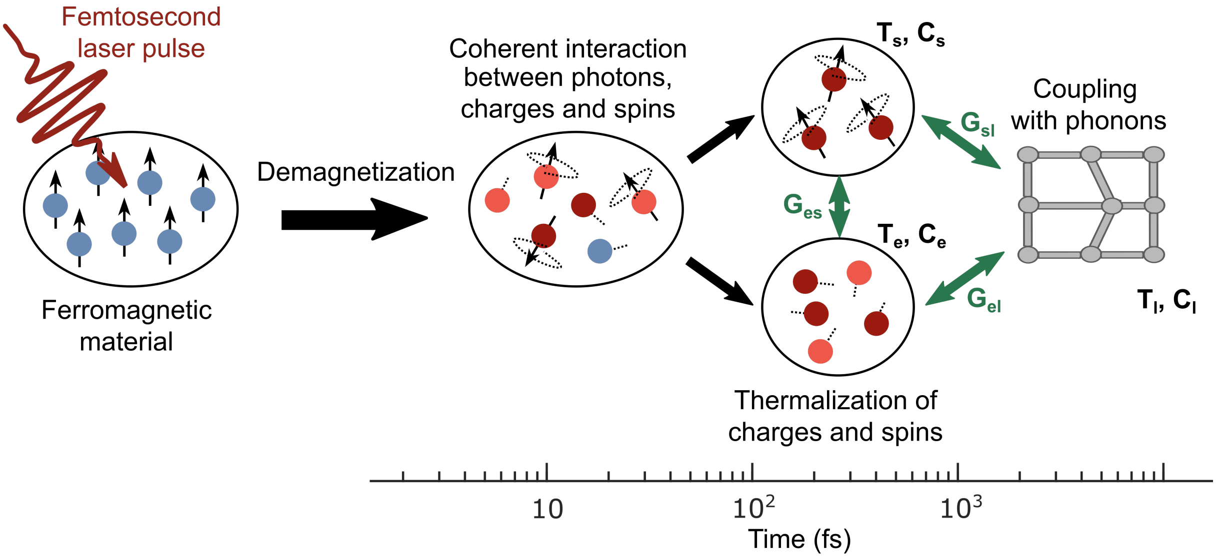

Figure 2.2: *Schematic representation of a sequence of mechanisms triggered in a ferromagnetic material by a femtosecond laser pulse. The initial excitation leads to coherent interactions between the laser field and the spin-polarized electron system, resulting in demagnetization. This coherent step is followed by the thermalization of the charges and spins, which interact together with the lattice through coupled baths described by three temperatures* T_e*,* T_s *and* T_l *and coupling constants* G_{es}*,* G_{el} *and* G_{sl} *(e: electrons, s: spins, l: lattice). Figure adapted from [24].*

This ultrafast magneto-acoustic coupling enables mechanical strain to influence magnetic anisotropy on a picosecond timescale, offering a novel route to control spin systems with high temporal precision. It has been demonstrated that strain pulses can excite spin precession, modulate domain configurations, or even assist magnetization reversal [24]. In Figure 2.2 a sequence of various processes upon optical excitation of a ferromagnetic material is represented. The incident femtosecond laser pulse initiates a coherent interaction with the spin and charge systems, leading to an immediate demagnetization [21]. This is followed by a cascade of energy redistribution events: first between electrons and spins, then, for longer delays, between these subsystems and the lattice. These energy flows are described by a multi-temperature model, where T_e, T_s, and T_l represent the electronic, spin, and lattice temperatures, respectively, and C_e, C_s, and C_l their corresponding heat capacities. The couplings between these reservoirs, denoted by G_{es}, G_{el}, and G_{sl}, govern the relaxation dynamics [25], [26].

The suspended nature of the laser-delaminated nickel cavities, free from substrate damping, supports long-lived acoustic modes that are ideal for coupling with magnetic excitations.

These hybrid effects are not only of fundamental interest but also pave the way for functional devices, such as tunable spin oscillators [27], acoustic spin injectors, or GHz magneto-acoustic memory elements [28]. The compactness, optical accessibility, and geometric tunability of these nanocavities make them excellent candidates for next-generation integrated magneto-optic and acousto-magnetic systems.

Thus, this thesis lays the groundwork for exploring multi-functional structural architectures that leverage ultrafast opto-acoustic and magneto-optical interactions, bringing us closer to the realization of integrated nanophotonic–spintronic platforms.

3

Ultrafast tools for investigating light-matter interactions

Understanding the dynamics that govern light-matter interactions on ultrafast timescales is crucial to explore fundamental processes in condensed matter physics. Many electronic and phononic dynamics in materials occur on femtosecond and picoseconds timescales. Therefore, there is a need for experimental techniques capable of capturing these fast dynamics events. Ultrafast laser-based methods have proved to be indispensable when controlling and tracking such dynamics. Among these methods, pump-probe spectroscopy stands as a well-established technique. This technique is based on two pulses, a pump pulse to excite the system and a delayed probe pulse to monitor its relaxation dynamics. This technique enables time-resolved measurements of transient changes in optical reflectivity or transmission of different materials. A detailed discussion of pump–probe spectroscopy is presented in Section 3.1.

However, enabling these capabilities relies on the generation and manipulation of ultrashort light pulses. Nonlinear optical effects, such as second-harmonic generation (SHG), third-harmonic generation (THG), and white-light generation (WLG), are essential for producing ultrafast broadband sources used in spectroscopy (Section 3.2). For ultrafast spectroscopic applications where a broadband tunability is required the implementation of optical parametric amplifiers (OPAs) is crucial.

3.1 Pump-probe spectroscopy

Ultrafast spectroscopy has evolved till become a distinct research field on its own, originating from the development of chirped pulse amplification (CPA) by D. Strickland and G. Mourou in 1985 [29]. This technique made it possible to amplify ultrashort laser pulses enabling the generation of femtosecond, 10^{-15} s, or even attosecond, 10^{-18} s, pulses. Years later, in 2018, this discovery was awarded with the Nobel Prize in Physics.

In the early 1990s, the field rapidly gained interest till current days, with over 1500 yearly publications citing "ultrafast spectroscopy" or "femtosecond spectroscopy" as keywords [30]. This academic interest probed the potential of ultrafast laser techniques across disciplines having a strong impact on modern physics, chemistry, and biology [31].

The need for such tools arises from the inherent temporal limitations of human perception and conventional electronics, constrained to milliseconds and nanoseconds time scales, respectively. Human vision integrates visual stimuli over tens to hundreds of milliseconds [32], while electronics are limited to nanosecond response time due to charge carrier mobility [33]. To explore in real-time faster events, such as molecular vibrations [34] or electron dynamics [35], it is necessary to employ light pulses that match with the phenomena period that we want to track, typically in the femtosecond domain. These light pulses not only observe but can also initiate dynamic processes in the a sample, enabling the tracking of ultrafast processes.

Historically, the first time-resolved optical experiment was attributed to Eadweard Muybridge in 1878. Muybridge managed to capture different phases of a horse in motion during a race using a set of cameras equipped with fast mechanical shutters. By the early 20^{th} century, the evolution of the camera allowed microsecond, 10^{-6} s, resolution, and by 1899, H. Abraham and T. Lemoine introduced the first pump-probe experiment. Two light pulses were used, the "pump" to excite the sample and a delayed "probe" to measure a time-dependent response [36].

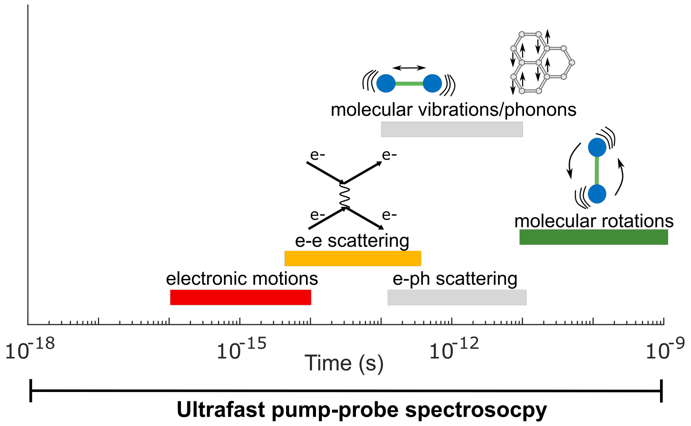

Figure 3.1: *Characteristic timescales of elementary processes in condensed matter physics probed by ultrafast pump–probe spectroscopy. This scheme highlights the wide temporal range accessible with ultrafast laser techniques, spanning from attoseconds (10^{-18} s) to nanoseconds (10^{-9} s). Ultrafast pump–probe spectroscopy enables the investigation of phenomena such as electron–electron (e–e) scattering, electron–phonon (e–ph) coupling, molecular vibrations, lattice phonons, and molecular rotations. Figure adapted from [37].*

For the following years, time-resolved spectroscopy resolution was limited by nanosecond, 10^{-9} s, pulse duration. Broadband lasers in combination with nonlinear optics made it possible to generate and measure ultrashort laser pulses with durations down to femtoseconds, 10^{-15} s, [38]. This scientific breakthrough made it possible to exploit pump probe spectroscopy to explore ultrafast phenomena, previously inaccessible, in condensed matter physics. As shown in Figure 3.1, a broad spectrum of physical processes fall within the temporal resolution of ultrafast pump–probe spectroscopy.

Ultrafast optical spectroscopy gathers all the experimental techniques that use sequences of ultrashort light pulses, with duration ranging from attosecond, 10^{-18} s, to picosecosecond, 10^{-12} s, to investigate photoinduced processes in atoms, molecules, nanostructures or solids [39].

As discussed earlier, the development of this field is closely connected with ultrafast laser technologies, since ultrashort laser pulses are required. For the purposes of this thesis, the ultrashort pulses used were generated by a commercial *Light Conversion* ® CPA Ytterbium (Yb) *PHAROS* laser system, centered around 1030 nm, with a pulse width of 220 fs and a pulse energy of 200 μm [40], [41]. These systems are known for their stability, efficiency and high average power, making them ideal for solid-state pump-probe experiments. However, as just mentioned, an intrinsic limitation is their fixed emission wavelength. By exploiting nonlinear optical effects we can tune this frequency over a broad spectral range or shorten the time duration of the output pulses. These optical effects and their implementations are discussed in detail in Section 3.2.

Having now established the role of ultrashort light pulses in enabling pump-probe spectroscopy, we can focus on how these pulses are used to study dynamic processes. In particular, for this thesis, we target the ultrafast response different solids by measuring transient changes in reflectivity or transmittivity. A pictorial representation of the pump-probe technique is shown in Figure 3.2, panel (a). Complementary, to intuitively describe pump-probe spectroscopy, we can model our sample as a two-level energy system, consisting of a ground state $|0\rangle$ and an excited state $|1\rangle$ (see Figure 3.2, panel (b)). At equilibrium (τ<0) the whole electron population is at ground state, giving rise to the steady-state optical response of the sample. Upon arrival of the pump beam (t=0), here considered to be resonant with the $|0\rangle \rightarrow |1\rangle$ transition, electrons are excited from the ground state to the excited state. Transient changes in the optical response of the system can be monitored by the probe pulse, here considered for simplicity to be also resonant with the $|0\rangle \rightarrow |1\rangle$ transition. In our toy model, a probe arriving at $t = \tau_2$ would experience a reduction in absorption, due to the lower number of available electrons in the ground state after pump excitation. Moreover, stimulated emission from the excited state would also contribute to the overall reduction of absorptivity (ground state bleaching). For longer time delays ($t = \tau_3$) the sample has almost fully relaxed back to equilibrium. By scanning the delay time between the pump and probe pulses the temporal evolution can be reconstructed, yielding information about the relaxation pathways.

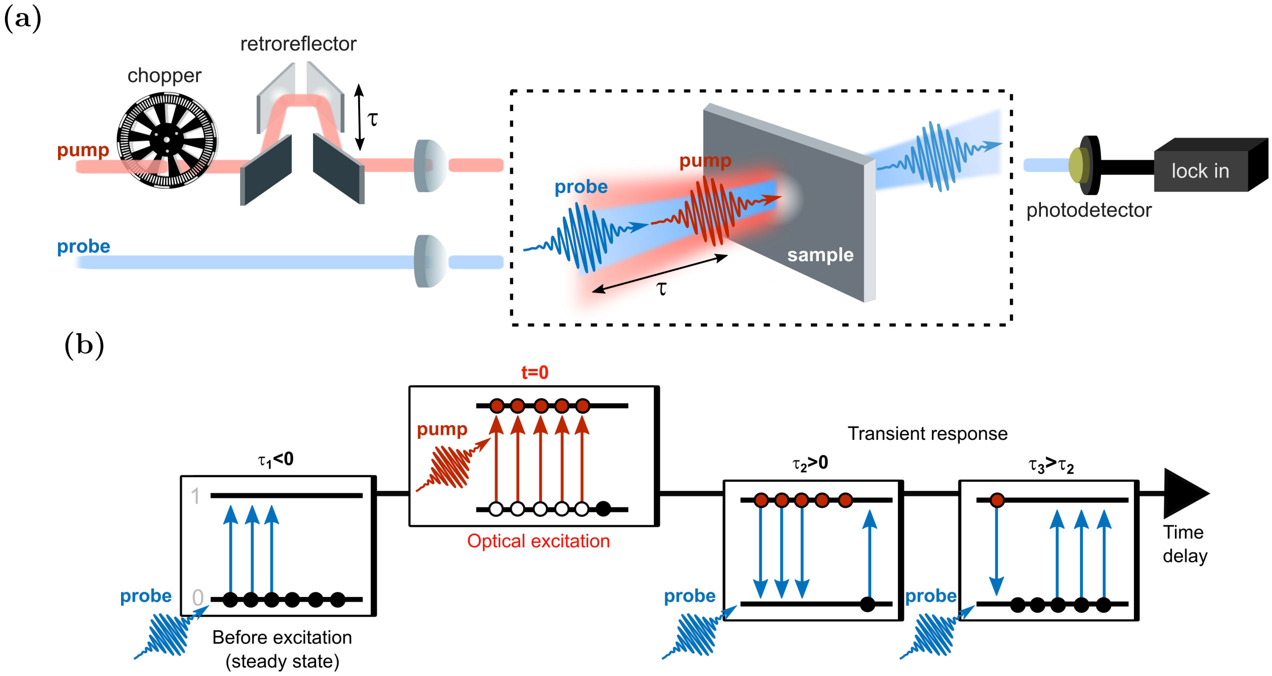

Figure 3.2: *(a) Schematic representation of an energy degenerate pump-probe configuration. A frequency modulated pump pulse excites the system while a probe pulse allows to track the relaxation dynamics after a time* τ*. Both pulses are focused on the sample and the differential transmittance (or reflectance) signal is measured by a photodetector. (b) Schematic modeling of a pump-probe experiment on a two-level system. Upon arrival, the pump pulse creates an out of equilibrium population in the state* $|1\rangle$*, affecting the transmittance of the probe beam at the energy associated to the* $|0\rangle \rightarrow |1\rangle$ *transition. By stroscopically measuring the differential transmittance at various time delays* τ*, the relaxation dynamics can be studied. Figure adapted from [42].*

From an experimental perspective, there are some requirements to take into consideration to successfully perform pump-probe measurements. Temporal and spatial precision are necessary to probe ultrafast phenomena. Therefore, to ensure interaction, the pump and probe beams must be spatially overlapped on the sample. Given that both beams exhibit Gaussian intensity profiles and to ensure that the probe samples a uniformly excited region, the pump beam spot size is usually kept significantly larger than the probe beam spot size.

In parallel, temporal overlap between pump and probe should be fulfilled, ensuring that both pulses arrive at the sample simultaneously. This temporal overlap is achieved by directing the pump beam through a retroreflector mounted on a translation stage, allowing precise control over the optical path length[43], [44].

In terms of excitation conditions, the pump fluence, i.e. the energy per unit area, is usually set at least two orders of magnitude higher than that of the probe. This ensures that the pump effectively initiates a measurable response, while the probe remains noninvasive.

Finally, to isolate the pump-induced signal from noise, modulation techniques are required. The most common methods to do so is with a mechanical chopper or by using an electro-optic modulator such as a Pockels cell. Both approaches periodically switch the pump beam on and off, causing the probe to alternately interrogate the sample in its excited and unexcited states. To extract this modulated signal, the output of the probe beam is fed into a photodetector connected to a lock-in amplifier. The lock-in amplifier selectively amplifies only those signals synchronized with the pump modulation frequency, filtering out broadband noise and improving the signal-to-noise ratio.

3.2 Nonlinear optics

Nonlinear optics [45], [46] is the study of light-matter interactions in which the optical properties of a material are modified by the incident light intensity. Unlike linear optics, where the material's response is independent of the light intensity, nonlinear optics emerge when the response of a material system to an applied optical field depends in a nonlinear manner on the strength of the optical field. In this case, the strong electromagnetic field is typically achievable by pulsed lasers.

In linear regimes, the induced polarization $\vec{P}(t)$, which represents the dipole moment per unit volume of a material, is directly proportional to the applied electric field $\vec{E}(t)$, described by the relation:

$$\vec{P}(t) = \varepsilon_0 \chi^{(1)} \vec{E}(t), \tag{3.1}$$

Here, ε_0 is the vacuum permittivity and $\chi^{(1)}$ is the linear susceptibility of the medium.

However, when the electric field intensity becomes sufficiently high, above approximately 10^8 W/cm^2, this linear approximation does not longer apply. Instead, the polarization must be expressed as a power series in the electric field:

$$\vec{P}(t) = \varepsilon_0 \left[\chi^{(1)}\vec{E}(t) + \chi^{(2)}\vec{E}^2(t) + \chi^{(3)}\vec{E}^3(t) + \cdots \right] = \vec{P}^{(1)}(t) + \vec{P}^{(2)}(t) + \tilde{P}^{(3)}(t) + \cdots \tag{3.2}$$

Each higher-order term corresponds to a different class of nonlinear optical phenomena. The second-order term, governed by $\chi^{(2)}$, gives rise to effects such as second-harmonic generation (SHG), sum-frequency generation (SFG), and difference-frequency generation (DFG). These processes can only occur in non-centrosymmetric media, where the material lacks inversion symmetry. The third-order term, governed by $\chi^{(3)}$, includes phenomena such as third-harmonic generation (THG), self-phase modulation (SPM), and four-wave mixing (FWM). Unlike second-order effects, these can occur in both centrosymmetric and non-centrosymmetric materials.

These nonlinear processes play a central role in ultrafast optics, particularly in generating new frequencies, compressing pulses, or producing broadband continua.

3.2.1 Second harmonic (SHG) and third harmonic (THG) generation

Second harmonic generation is an example of second-order nonlinear optical process.It occurs when a laser beam with an electric field expressed as

$$\vec{E}(t) = Ee^{-i\omega t} + \text{c.c.} \tag{3.3}$$

interacts with a nonlinear material that exhibits a non-zero second-order susceptibility $\chi^{(2)}$. Starting from the second-order contribution to the nonlinear polarization:

$$\vec{P}^{(2)}(t) = \varepsilon_0 \chi^{(2)} \vec{E}^2(t) \tag{3.4}$$

The resulting second-order nonlinear polarization for second harmonic can be written as:

$$\vec{P}^{(2)}(t) = 2\varepsilon_0 \chi^{(2)} EE^* + \varepsilon_0 \chi^{(2)} E^2 e^{-i2\omega t} + \text{c.c.} \tag{3.5}$$

Conceptually, SHG can be visualized as two photons of frequency ω combining through a virtual energy level to generate a single photon at frequency 2ω. Importantly, SHG only occurs in non-centrosymmetric media, as materials with inversion symmetry exhibit $\chi^{(2)} = 0$. Therefore, SHG is not observed in liquids, gases or amorphous solids like glass. In practice, a commonly used nonlinear crystal for SHG is β-barium borate (BBO).

In addition to SHG, second-order processes also include sum-frequency generation (SFG) and difference-frequency generation (DFG). These occur when the input electric field contains two distinct frequency components:

$$\vec{E}(t) = E_1 e^{-i\omega_1 t} + E_2 e^{-i\omega_2 t} + \text{c.c.} \tag{3.6}$$

Substituting into the second-order polarization (eq. 3.4) the nonlinear polarization is given by

$$\begin{aligned}\tilde{P}^{(2)}(t) = \varepsilon_0\chi^{(2)}\big[&E_1^2 e^{-2i\omega_1 t} + E_2^2 e^{-2i\omega_2 t} + 2E_1E_2 e^{-i(\omega_1+\omega_2)t} \\ &+ 2E_1E_2^* e^{-i(\omega_1-\omega_2)t} + \text{c.c.}\big] + 2\varepsilon_0\chi^{(2)}(E_1E_1^* + E_2E_2^*)\end{aligned} \tag{3.7}$$

Each term corresponds to a different second-order nonlinear effect:

$$P(2\omega_1) = \varepsilon_0\chi^{(2)}E_1^2 \quad \text{(SHG)} \tag{3.8}$$

$$P(2\omega_2) = \varepsilon_0\chi^{(2)}E_2^2 \quad \text{(SHG)} \tag{3.9}$$

$$P(\omega_1+\omega_2) = 2\varepsilon_0\chi^{(2)}E_1E_2 \quad \text{(SFG)} \tag{3.10}$$

$$P(\omega_1-\omega_2) = 2\varepsilon_0\chi^{(2)}E_1E_2^* \quad \text{(DFG)} \tag{3.11}$$

These processes are illustrated in the energy-level diagram in Figure 3.3, where solid lines represent ground states and dashed lines correspond to virtual intermediate states.

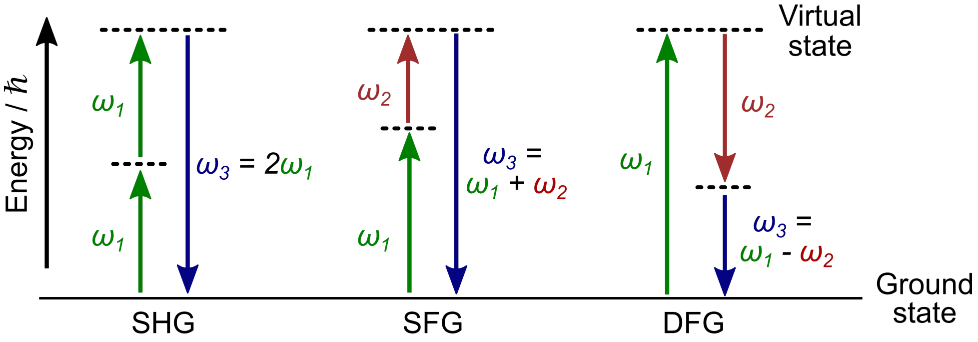

Figure 3.3: *Energy level diagram illustrating second harmonic generation (SHG), sum frequency generation (SFG) and difference frequency generation (DFG), all of which are second-order nonlinear optical processes.*

Moving to the third-order nonlinear processes, the polarization is governed by:

$$\vec{P}^{(3)}(t) = \varepsilon_0 \chi^{(3)} \vec{E}^3(t) \tag{3.12}$$

Assuming the incident field contains three distinct frequency components:

$$\vec{E}(t) = E_1 e^{-i\omega_1 t} + E_2 e^{-i\omega_2 t} + E_3 e^{-i\omega_3 t} + \text{c.c.} \tag{3.13}$$

The cubic term $\vec{E}^3(t)$ gives rise to a large number of frequency components—up to 44 in the general case. A key process within this category is third harmonic generation (THG), where three photons at frequency ω combine to produce a photon at 3ω. Unlike second-order effects, THG is allowed in both centrosymmetric and non-centrosymmetric media, making it broadly applicable to materials such as glass, silicon, and other isotropic dielectrics. The energy-level representation of THG is shown in Figure 3.4.

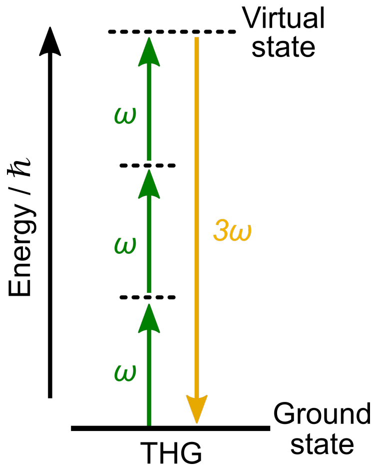

Figure 3.4: *Energy level diagram describing third harmonic generation (THG).*

3.2.2 White light generation (WLG)

Another nonlinear process of significant relevance for this thesis is white light generation (WLG) [2], [18]. In general, WLG refers to the creation of extremely broadband optical spectra, often spanning from the visible to the near-infrared, by propagating an ultrashort, high-intensity pulse through a centrosymmetric medium such as a sapphire or yttrium aluminum garnet (YAG). In particular, YAG is commonly chosen for white light generation because it is well-suited to Yb-based systems with longer pulses, operating at higher repetition rates and longer wavelengths, in contrast to Ti:Sa (titanium-sapphire) based systems [47], [48]. A reference spectrum generated by propagation of a 1030 nm femtosecond pulse through a 4-mm-thick YAG crystal is shown in Figure 3.5. This broadband output is commonly referred to as a supercontinuum.

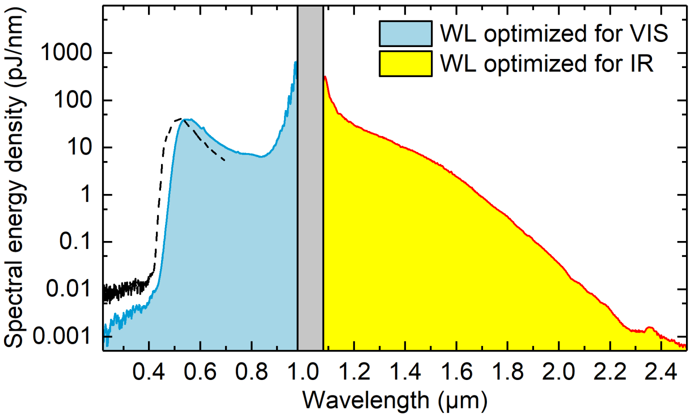

Figure 3.5: Broadband white light spectrum generated by focusing a 1030 nm femtosecond pulse into a 4-mm-thick YAG crystal. The resulting supercontinuum spans from the visible (blue area) to the near-infrared range approximately (yellow area). The gray area includes the pump wavelength of 1030 nm. The shape and bandwidth of the spectrum depend strongly on the input pulse energy, duration, and the nonlinear properties of the crystal. Figure taken from [47].

The underlying physical mechanisms of WLG are complex and highly sensitive to the input pulse parameters, such as energy and time duration, and to the nonlinear optical properties of the material. Among the key contributing effects, the optical Kerr effect plays a central role. This third-order nonlinear process induces a change in the refractive index of a material in response to the intensity of the applied optical field. This is typically described by introducing a nonlinear refractive index n_2, such that the time dependent refractive index $n(t)$ is written as:

$$n(t) = n_0 + n_2 I(t) \tag{3.14}$$

where n_0 is the steady-state value refractive index and $I(t)$ is the intensity the incident field. Due to this time-dependent refractive index, a laser pulse experiences a phase shift proportional to its instantaneous intensity value. In turn, this causes an instantaneous frequency shift, process known as self-phase modulation (SPM):

$$\Delta\omega(t) \propto n_2 \frac{dI(t)}{dt} \tag{3.15}$$

leading to the creation of new spectral components. Together with SPM other nonlinear processes such as self-focusing (focusing of the laser beam due to the optical Kerr effect) contribute to WLG in bulk crystals.

A detailed discussion of these phenomena goes beyond the scope of this thesis and can be found in [49]. The relevance of WLG in the context of this work is two-fold. First of all, WLG spectra can be used as broadband probe pulses in the context of a pump-probe experiment. Moreover, WLG is commonly employed to obtain a broadband seed beam for optical parametric amplification, as discussed in the next Section 3.3.

3.3 Optical parametric amplification (OPA)

Optical parametric amplifiers (OPAs) [50],[51] are nonlinear optical devices based on second-order effects that enable the generation and amplification of ultrashort pulses across a broad and continuously tunable spectral range, typically covering the visible to mid-infrared (mid-IR) regions [52]. As discussed by Manzoni et al. [53], the OPA process transfers energy from a high-frequency and high-intensity pump pulse to a lower-frequency and lower-intensity signal pulse, resulting in the generation of an additional beam called the idler, while conserving both energy and momentum.

One of the main limitations of commercially available femtosecond laser sources is their operation at a fixed central wavelength with modest tunability. This presents a disadvantage, particularly in pump–probe spectroscopy, where flexible spectral control over both pump and probe beams is essential to resonantly excite or probe specific dynamics. Nonlinear optical techniques, in particular optical parametric amplification, provide means to overcome this limitation by generating widely tunable ultrashort pulses [54].

The principle of OPA relies on a second-order nonlinear interaction in a suitable crystal, such as BBO. A pump photon with angular frequency ω_p interacts with a signal photon ω_s to generate a third photon, the idler ω_i, under the condition of energy conservation:

$$\hbar\omega_p = \hbar\omega_s + \hbar\omega_i \tag{3.16}$$

This is accompanied by the momentum conservation (or phase-matching) condition:

$$\vec{k}_p = \vec{k}_s + \vec{k}_i \tag{3.17}$$

where $\vec{k}_j$ are the wave vectors of the pump, signal, and idler beams. The process is effectively a type of difference frequency generation (DFG), where a high-frequency pump photon transfers its energy to lower-frequency signal and idler photons via virtual absorption and stimulated emission.

A special case arises under the degeneracy condition, when signal and idler frequencies are equal:

$$\omega_s = \omega_i = \frac{1}{2}\omega_p \tag{3.18}$$

For efficient amplification, the phase-matching condition $\Delta k = k_p - k_s - k_i = 0$ must also be satisfied. This is typically achieved by adjusting the orientation of the nonlinear crystal.

In summary, efficient parametric amplification relies on several factors including the nonlinear crystal [55], [56], crystal thickness, and phase-matching condition [53]. OPAs allows for continuously tunable amplification over broad spectral ranges and can also support the generation of shorter pulses than the pump by amplifying broadband seed signals. This capability makes OPAs ideal for applications that demand both spectral and temporal flexibility.

A schematic of the OPA interaction, showing energy and momentum conservation, is provided in Figure 3.6.

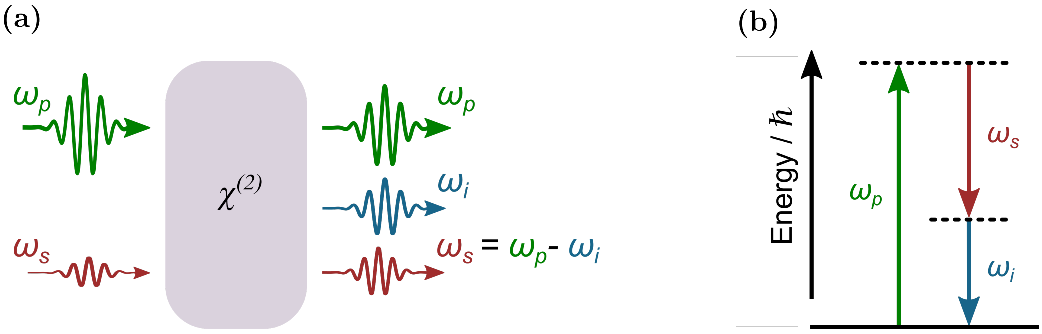

Figure 3.6: Principles of optical parametric amplification.(a) Scheme of the OPA process: an intense pump beam with angular frequency ω_p amplifies a weak signal beam (ω_s) and creates an idler beam ($\omega_i = \omega_p - \omega_s$, DFG) in the process. (b) photon energy balance in the OPA process.

3.3.1 Visible (VIS) and visible to near-infrared (VIS-NIR) OPAs

For the purpose of this thesis two OPAs, visible (VIS) and visible to near-infrared (VIS-NIR), were used as pump sources to perform the transient reflection measurements later discussed in Chapter 5. These OPAs were originally built by former students at the *University of Konstanz* and later realigned and optimized in Luxembourg by my colleague Thomas Deckert. In the following, we describe the wavelength ranges covered by each system and provide a brief overview of their corresponding experimental configurations.

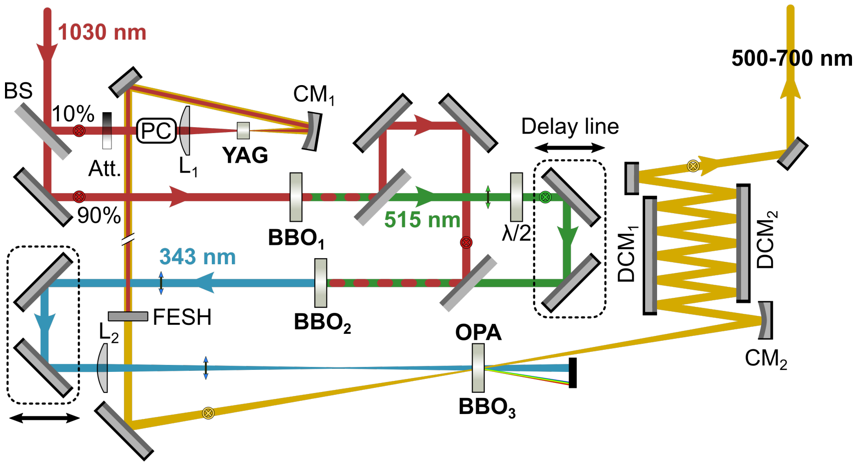

Figure 3.7: Sketch of the VIS NOPA covering the 500-700 nm spectral range. The fundamental (1030 nm) is divided into pump and signal branches. The pump branch undergoes third harmonic generation via two BBO crystals to produce 343 nm light. The signal branch generates a white-light continuum in a YAG crystal. Both beams are spatially and temporally overlapped in a BBO crystal for parametric amplification. Curved and chirped mirrors provide beam collimation and dispersion compensation, respectively. Figure adapted from [57].

Starting with the visible NOPA (non-degenerate optical paramtetric amplifier), whose sketch is shown in figure Figure 3.7 and generates a broadband covering ranges from 500 to 700 nm. In detail, a Yb:KGW laser *PHAROS, Light Conversion* ® operating at 50 kHz repetition rate provides 230 fs pulses at 1030 nm central wavelength (fundamental) with 100 µJ pulse energy. A beam splitter divides the driving pulses into a pump and seed, or signal, branch in a 9:1 ratio, respectively. The intense reflection subsequently passes two nonlinear frequency conversion steps for generating the TH (343 nm) pump pulses. Firstly, the fundamental is frequency-doubled in a 2-mm-thick β-barium borate (BBO$_1$) crystal cut at $\theta = 24^\circ$. The resulting SH (515 nm) is subsequently upconverted to the TH with the residual fundamental in a 2-mm-thick BBO$_2$ crystal cut at $\theta = 32^\circ$. Simultaneously, the signal branch, corresponding to the weaker portion of the fundamental, is focused (L$_1$ f = 100 mm) into a 3-mm-thick YAG crystal for WL generation. A variable attenuator (att.) and an iris allow to adjust the pumping power density and numerical aperture, respectively, ensuring stability and avoiding multi-filamentation. A short-pass filter (FESH) removes the residual fundamental from the seed to suppress unwanted nonlinear interactions during amplification. Finally, the TH pump and WL seed pulses are individually focused into a nonlinear crystal (L_2 f = 200 mm) to meet in space and time for parametric amplification (BBO_3). The crystal is placed approximately 30 mm behind the pump focus to harness self-focusing and limit the divergence of the pump beam. The amplified signal is collimated by a curved mirror (CM_2), and dielectric chirped mirrors (DCM_1 and DCM_2) are used for dispersion compensation.

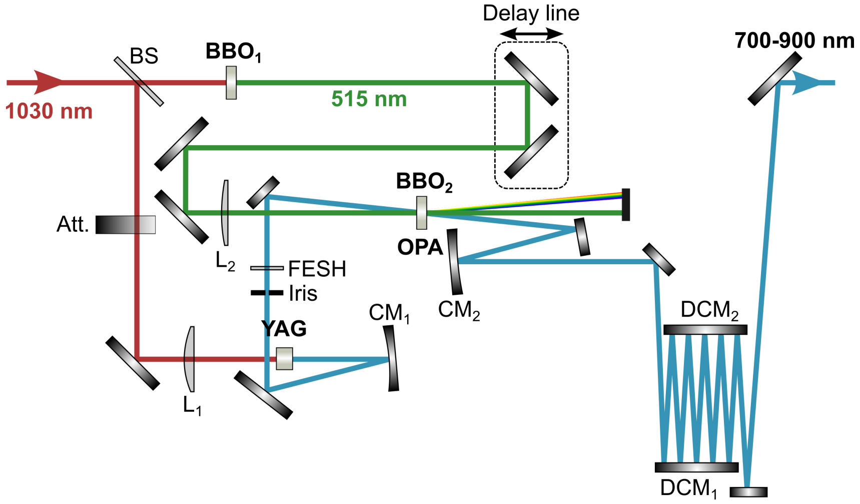

Figure 3.8: Sketch of the VIS-NIR NOPA covering the 700-900 nm spectral range. The fundamental (1030 nm) is divided in two branches, pump and signal. The pump branch is frequency-doubled (515 nm) in a BBO crystal. The signal branch generates a white light continuum in a YAG crystal. Both beams are focused into a BBO crystal for parametric amplification. The amplified output is collimated and dispersion-compensated using curved and chirped dielectric mirrors, respectively. Figure adapted from [47].

A schematic of the VIS-NIR NOPA is shown in Figure 3.8. This system shares the same Yb:KGW laser as the visible OPA as both are mounted on the same optical table. A portion of the laser fundamental, 1030 nm, is used for supercontinuum generation in a 2-mm-thick YAG crystal. As the just described VIS OPA, a variable attenuator (att.) is used to tune the pulse energy to achieve optimum conditions. The generated WL is collimated by a curved mirror (CM_1) and spectrally filtered with a short pass filter (FESH) to avoid amplification of residual infrared light. The remaining portion of the pump beam is frequency doubled in a 2-mm-thick BBO_1 crystal ($\theta = 34°$), yielding 515 nm pulses for pumping the OPA. A variable delay line allows fine temporal synchronization between pump and seed. The pump beam is then focused (L_1 f = 200 mm) several centimeters before the nonlinear crystal used for amplification, a 1.5-mm-thick BBO_2 crystal. Broadband amplification is achieved at the phase matching angle of $\theta = 24°$. The broadband amplified signal is collimated by a second curved mirror (CM_2) and dispersion is compensated using dielectric chirped mirrors (DCM_1 and DCM_2). The resulting spectrum ranges from 700 to 900 nm, offering excellent tunability in the visible to near-infrared.

The spectra covered by both OPAs is represented in Figure 3.9 in violet the VIS NOPA covering wavelengths from 500 to 700 nm and in green the NIR NOPA ranging from 700 to 900 nm.

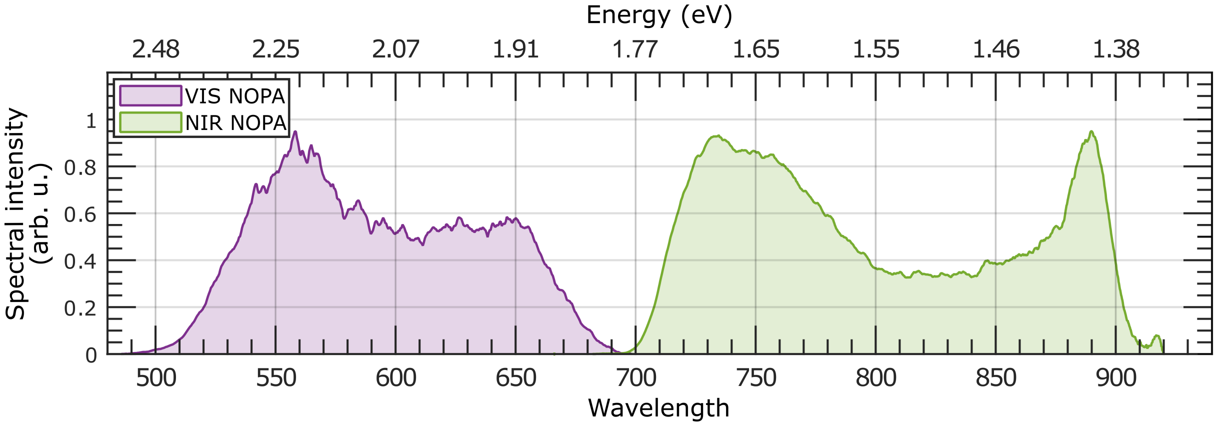

Figure 3.9: Ultra-broadband spectra intensity of VIS NOPA, in violet, and VIS-NIR NOPA, in green. Figure adapted from [58].

3.4 Custom-made experimental setup

To perform the ultrafast measurements presented in next Chapter 4, a custom-made pump probe spectroscopy setup was developed. A schematic layout of the setup is shown in Figure 3.10.

From right to left, the system is based on a Yb:KGW laser (*PHAROS, Light Conversion* ®), that delivers 220 fs pulses at a central wavelength of 1030 nm, with an average power of 20 W at a 100 kHz repetition rate. In this setup, 500 mW of the total power will be used. The initial beam, s-polarized, is split by a dielectric beam splitter (BS), 70:30, into two arms conforming the pump and probe lines.

The pump line is directed through a retroreflector mounted on stage, indicated as delay line, to provide precise temporal overlap with the probe. The pump beam is obtained by frequency-doubling the laser fundamental, 1030 nm, using a 2-mm-thick β-barium borate (BBO) crystal ($\theta = 34°$), producing pulses at 515 nm. The corresponding second-harmonic spectrum is shown in Figure 3.11, panel (a). The pump beam is modulated at half the laser repetition rate, 50 kHz, using a Pockels cell (PC). This device rotates the polarization of every other pulse, enabling alter-

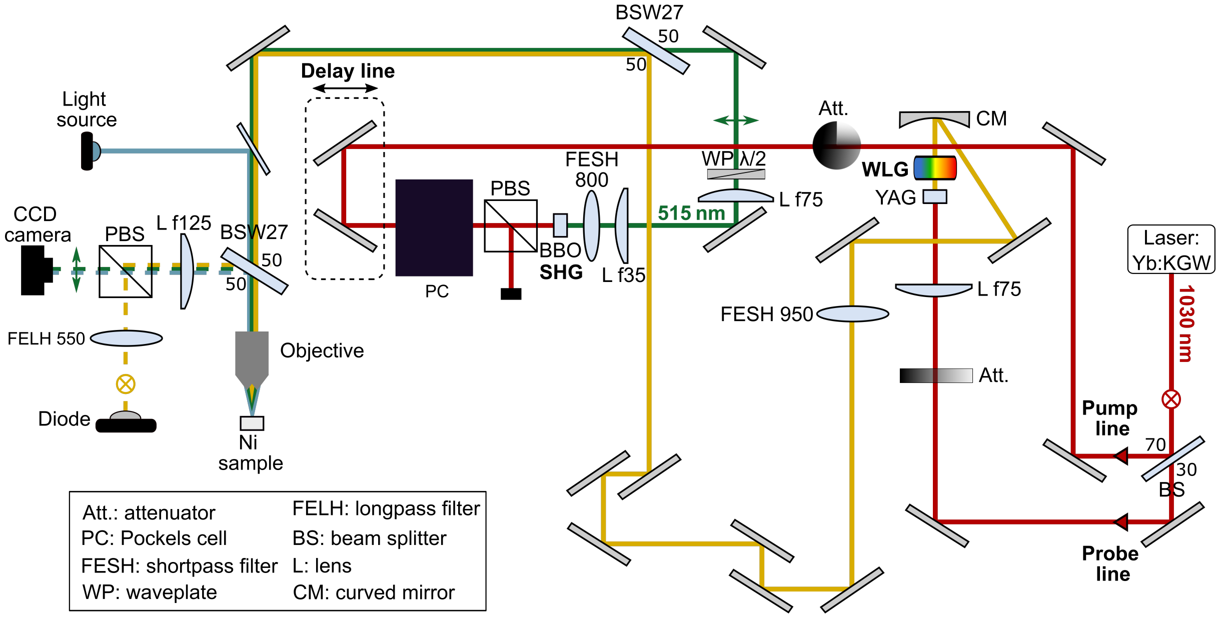

Figure 3.10: *Schematic representation of the custom-built femtosecond pump–probe spectroscopy setup used for time-resolved reflectivity measurements on solid-state samples. A Yb:KGW laser (1030 nm, 220 fs, 100 kHz) provides the fundamental pulse, which is split into two arms: pump and probe. The pump, in red, is frequency-doubled to 515 nm using a BBO crystal (SHG) and modulated at 50 kHz with a Pockels cell (PC). It is then directed through a delay line for temporal control before being focused onto the sample with a reflective objective. The probe beam, in mustard, is converted into a white-light continuum (500–950 nm) using a YAG crystal (WLG), collimated, and directed toward the sample. Both beams are spatially and temporally overlapped at the sample, where the probe monitors the pump-induced changes. The reflected probe is recollected by the same objective, separated via a polarizing beam splitter (PBS), and detected by a photodiode for lock-in detection. A CCD camera enables beam alignment and imaging of the sample.*

nating excitation of the sample between excited and unexcited states. This modulation scheme facilitates lock-in detection with high signal-to-noise discrimination, as described in Section 3.1. The pump beam is then collimated and focused onto the sample surface using a reflective objective (NA = 0.4). This configuration was selected to ensure uniform excitation over the region sampled by the probe, especially critical when targeting microstructures.

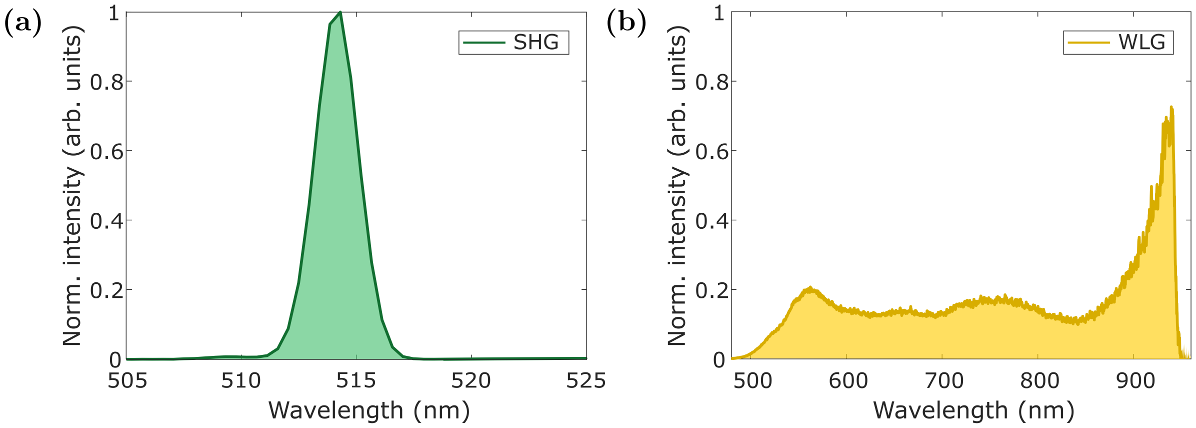

Figure 3.11: *(a) Normalized intensity of the SHG spectrum, pump. (b) Normalized intensity of the WL spectrum, corresponding to the probe.*

The probe beam is a white-light supercontinuum, generated by tightly focusing a small portion of the 1030 nm fundamental beam into a 6-mm-thick Yttrium Aluminum Garnet (YAG) crystal. This produces a broadband spectrum ranging from 500 to 950 nm, with an approximate duration of 200 fs (see spectrum in Figure 3.11, panel (b). After generation, the white-light beam is collimated and filtered. After SHG and WLG both pump a probe beams are collinear till sample interaction. The probe beam is therefore focused onto the sample following the same optical path as the pump beam. However, the focused spot size is significantly smaller than that of the pump spot to ensure that it interrogates a homogeneously excited region. After reflection from the sample, the probe beam is recollected and recollimated by the same objective. It is then passed through a polarizing beamsplitter (PBS), which filters the orthogonally polarized (p-polarized) pump. The reflected s-polarized probe is finally detected by a photodiode connected to a lock-in amplifier. Details about each beam spot size as well as fluence values and other measurement parameters are addressed in next Chapter, in Subsection 4.2.1.

The objective serves a second role. Apart from perpendicularly focusing both beams onto the sample, it also serves imaging purposes. With the help of an external light source, a lamp, and a CCD camera one can verify at real time that the beams overlap positions is centered on the region of interest.

In conclusion the setup enables sub-picosecond temporal resolution and broadband spectral sensitivity.

4

Low-damped acoustic modes in nickel cavities

In this chapter we investigate the experimental and numerical analysis of the opto-mechanical response of nickel acoustic cavities, i.e. freestanding nanostructures, designed to support long-lived acoustic resonances. These structures consist of suspended polycrystalline nickel thin films, fabricated through controlled picosecond laser delamination [59] using focused pulses transmitted through a SiO_2 substrate. The aim of these dome-shaped structures is to prove their efficiency in enhancing material properties relevant to opto-acoustic applications.

In here we report the dynamics of coherent acoustic phonons optically excited by femtosecond laser pulses and monitored via time-resolved reflectivity measurements. To assess the performance of these freestanding structures, we compare their acoustic response to that of reference samples, where the nickel film remains in direct contact with the substrate [60], [61].

By combining Fourier transform analysis of the pump-probe experimental data with numerical simulations, we prove that for suspended nickel cavities high-frequency (> 10 GHz) longitudinal acoustic pulses resonate inside the structure for longer time delays and present significantly reduced damping compared to the reference, nickel film on SiO_2.

These findings suggest that picosecond laser-induced delamination offers an efficient and scalable fabrication route for the realization of micro-structured, low-loss acoustic resonators, promising for opto-acoustic applications [62].

4.1 Freestanding polycrystalline nickel cavities

In mechanical and material engineering, the development of low-damping resonators is of critical importance for a variety of emerging technologies, ranging from ultralow noise opto-mechanical quantum technologies [63] to energy efficient magneto-acoustics in spintronic devices [64]. These demands have driven extensive research into acoustic wave engineering, with particular attention to minimizing energy dissipation and enhancing wave propagation. One effective strategy involves the elimination of the substrate [65], [66].

In this context, patterned cavities support a unique combination of multiple excitations such as magnetic [66], optical [67], and acoustics [68], focusing our studies on the two last domains (see Subsection 4.1.1). The fabrication of these structures was achieved using laser delamination, a recently developed technique, where laser pulses are focused through a glass substrate to selectively detach a thin nickel film from the substrate, achieving closed, dome-shaped cavities. When properly controlled, this process enables on-demand patterning of suspended membranes on areas down to the microscale, thereby enabling the development of opto-acoustic devices that would require very complex and time-consuming processing by using more conventional lithography techniques.

The opto-mechanical response of these cavities is studied upon ultrafast pump-probe spectroscopy, which enables both the excitation and time-resolved detection of coherent acoustic dynamics. In this study, we focus on understanding the acoustic properties of freestanding Ni film cavities proving, experimentally and numerically, that the suspended Ni membrane indeed displays a lower damping than that of the unexposed film. These findings are detailed and discussed in the following Section 4.2.

4.1.1 Foundations for opto-acoustic cavity engineering

In recent years, considerable research efforts have been devoted to the fabrication, characterization and theoretical modeling of metallic cavities that support optical, acoustic or magnetic excitations. These structures serve as promising platforms towards next generation devices. Among them, freestanding ferromagnetic cavities, particularly those based on nickel, are of notable interest due to their ability to support coherent mechanical oscillations while enabling optical and magnetic coupling.

From a design and fabrication perspective, V. Temnov et al. introduced reliable methods based on controlled thermomechanical spallation and delamination to achieve reproducible metallic cavities [69],[69]. These techniques motivated the fabrication method employed to develop the cavities presented in this study.

On the characterization side, J. Bigot and collaborators have extensively explored ultrafast excitation and detection of acoustic and magnetic dynamics in nickel cavities using pump-probe spectroscopy excitation [61], [66]. In particular, their results demonstrated the possibility of modulating magnetization on ultrafast timescales via acoustic pulses generated through femtosecond optical excitation. This magneto-acoustic coupling mechanism has been a strong motivator for the work presented here.

Based on this foundation, Ghita et al. developed a semi-analytical model to determine the amplitudes and lifetimes of perpendicular acoustic phonon resonances in freestanding nickel films [60]. Their work provides theoretical support to previous ultrafast magneto-acoustic studies and sets a reference line to our pump-probe analysis. While their study connects acoustic dynamics and magnetic responses, our present investigation remains focused on mechanical aspects of the cavity response.

Motivated by both these experimental and theoretical analysis, we focus here on the optical excitation and acoustic characterization of dome-shaped, freestanding nickel cavities. The starting material is a 230 nm-thick polycrystalline nickel film, thermally evaporated onto a SiO_2 substrate. The laser-induced delamination process results in localized detachment of the Ni layer, forming this bubble-like cavities surrounded by regions of intact film. These structures serve as symmetric (air/Ni/air) acoustic resonators, where the generated longitudinal acoustic pulses reflect between the two Ni/air interfaces, resulting in multiple reflections before decaying.

In the following Subsection 4.1.2, we describe in detail the fabrication technique, including the laser parameters, patterning conditions, and resulting cavity geometries.

4.1.2 Laser delamination fabrication

For several decades, ultrashort laser pulses have been employed as a powerful tool for the precise and efficient fabrication of metallic micro- and nanostructures. Among the earliest and most widely adopted methods is laser ablation, where high-intensity pulses are used to remove material with minimal thermal damage to the surrounding [70]. However, the use of shorter laser pulses for sample irradiation allows for a better material control compared to longer pulses, making them ideal for nanostructuring. [71]. The origins of laser-induced spallation can be traced back to the 1970s, when nanosecond pulse lasers were first used to generate stress-induced delamination in thick metallic films [72]. This process, which relies on shockwave-induced tensile stress at the film–substrate interface, opened the door to non-contact mechanical manipulation of thin films.

In this work we focus on laser delamination, a non-destructive technique. Contrary to other techniques such as ablation, it offers a more controlled fabrication procedure ensuring that the material is not damaged. In particular, a fs-laser pulse enables the separation of a thin film from the substrate. This delamination procedure on ferromagnetic Ni films was first implemented by V. Temnov et al. in 2020 [69]. With their approach, they managed to pattern periodic arrays of closed cavities irradiating a 300 nm Ni film. This process allows for a fine tunability and a high precision presenting in their work elongated cavities with periodicities ranging from 3 to 30 μm and heights up to 200 nm in the center. Figure 4.1 (a) shows a differential interference microscopy image of an array of elongated cavities, each narrow line corresponds to a single cavity. Using surface interferometry, a surface profile of several cavity cross sections is provided. This analysis shows both the height and width of different cavities, proving a consistent and reproducible fabrication procedure, see Figure 4.1 (b).

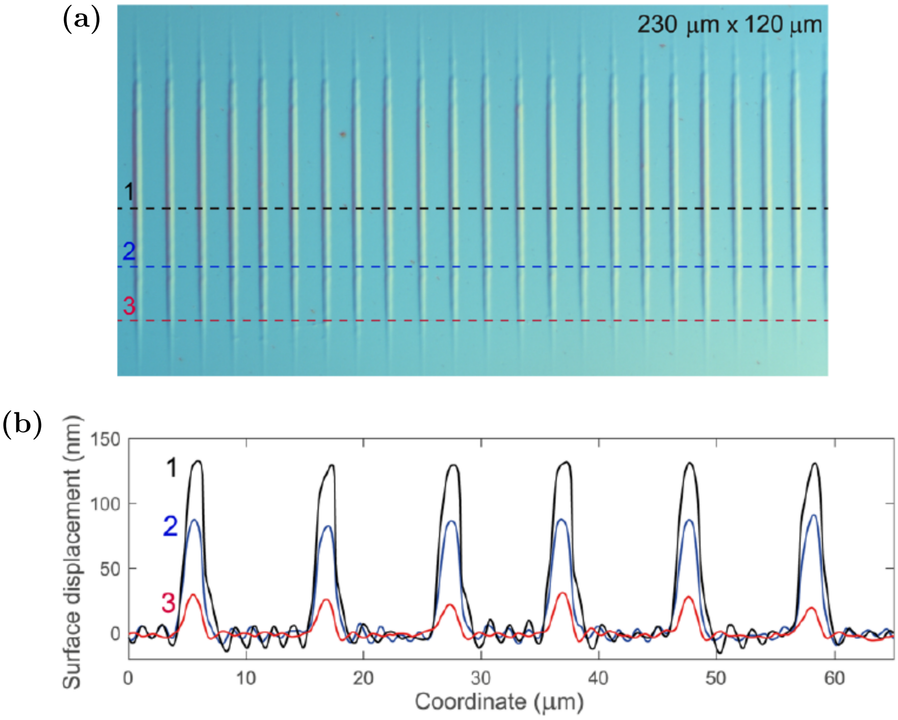

Figure 4.1: *(a) Interference microscopy tow view image of a periodic array of elongated cavities fabricated under fs-spallation. (b) Surface profile corresponding to different cross-sections of the cavity array, marked in black, blue and read. Figure taken from [69].*

Our sample was fabricated by V. Temnov et al. following a similar delamination technique at the *Institute Polytechnique de Paris*. In our case, we start from a 230 nm nickel film evaporated on top of a SiO_2 substrate. To fabricate the cavities, a commercial 30 ps pulsed laser was used, EKSPLA, at 1064 nm and with a repetition rate of 10 kHz. The pulsed laser beam strikes the substrate at a 45 degree angle, focused by a 20 cm lens. The sample is scanned by moving its position through the line focus at a constant speed of 1 mm/s. As a result, sequences of nearly identical structures separated equidistantly by 100 μm are fabricated. As seen in Figure 4.2 panel (a), which presents an overall view of the sample taken with scanning electron microscope (SEM), several lines of structures were fabricated. Each line corresponds to a different delamination pulse energy [μJ], therefore obtaining cavities of different dimensions. This pulse energy is tuned by a motorized λ-half waveplate and a polarizer. In order to obtain closed structures the used laser fluence should be slightly below, a few percent, than the Ni ablation threshold (13.6 μJ). Figure 4.2, panel (b) shows two sketches corresponding to different structure lines: sketch 1 refers to the structures in the second row, while sketch 2 corresponds to the structures in the eighth row. As mentioned above, when the applied laser fluence exceeds the ablation threshold, the film is damaged, resulting in well-defined holes, as illustrated in sketch 1. For this reason, the cavities analyzed in this work were those in the eighth row where closed cavities are observed, as depicted in sketch 2.

A zoom into one of the cavities located in that row is shown in Figure 4.3. To better appreciate its shape it is circled in white. The lateral dimensions are as well indicated in the figure, having a total length of approximately 20 μm and width of 9.4 μm. It is worth mentioning that the rectangular structure placed on top of the cavity corresponds to a platinum layer only used to perform a focused ion beam (FIB) to later image with SEM the vertical profile of the cavity. This Pt layer is deposited by ion-beam induced deposition and acts as protection for the structure and prevents the cavity from damage during FIB cutting.

Figure 4.4 shows the transversal profile of nickel on top of the substrate before any processing, panel (a), hereafter referred to as the "film", and the transversal profile of the free-standing nickel, referred to as the "cavity", in panel (b). Both insets show a zoom image into the crystal structure, allowing to observe the appearance of large crystal grains after the delamination procedure in the cavity case. This could potentially affect the opto-acoustic signal in the cavity compared to the film. A deeper insight into the propagating acoustics is discussed in the analysis Section 4.2. These cross-section SEM images were obtained at *CIC nanoGUNE* using a Helios NanoLab 450S (ThermoFisher) at an accelerating voltage of 2-5 kV and a beam current of 50-100 pA.

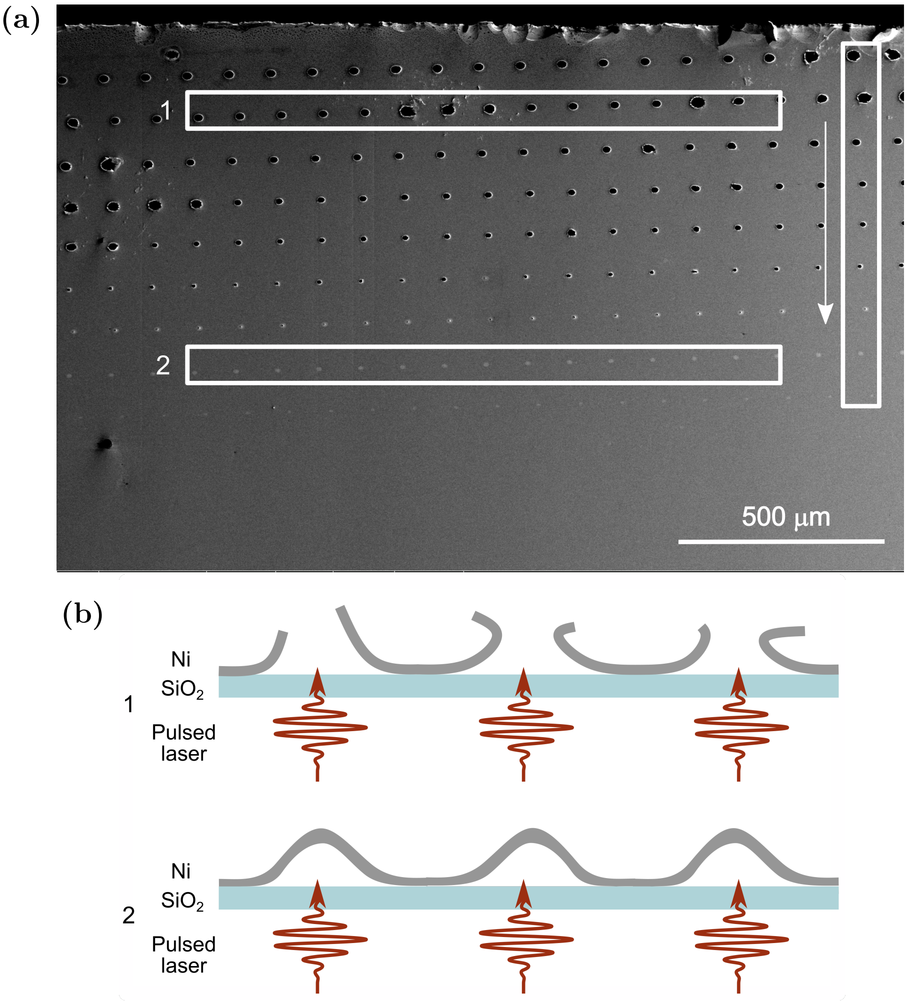

Figure 4.2: *(a) SEM image of the entire nickel sample, showing nine rows of structures fabricated by laser delamination with decreasing fluence values, as indicated by the vertical rectangle on the right. (b) Corresponding sketches of selected structure lines highlighted in panel (a). Sketch 1 corresponds to the region in rectangle 1, where the laser fluence above the ablation threshold produced well-defined holes in the film. Rectangle 2 encloses the closed-cavity structures characterized in this work.*

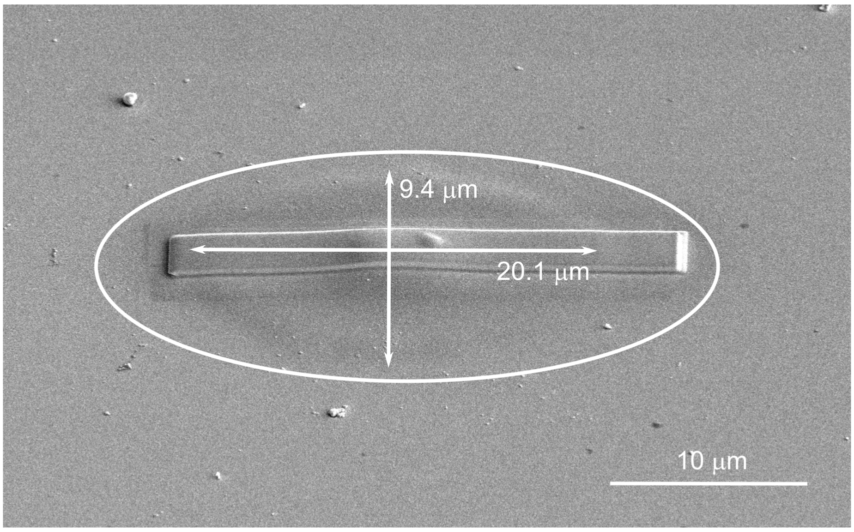

Figure 4.3: *Top-view SEM image of a single nickel cavity, circled in white. The vertical and longitudinal marks indicate the lateral dimensions. The rectangle on top is a Pt layer deposited to perform FIB.*

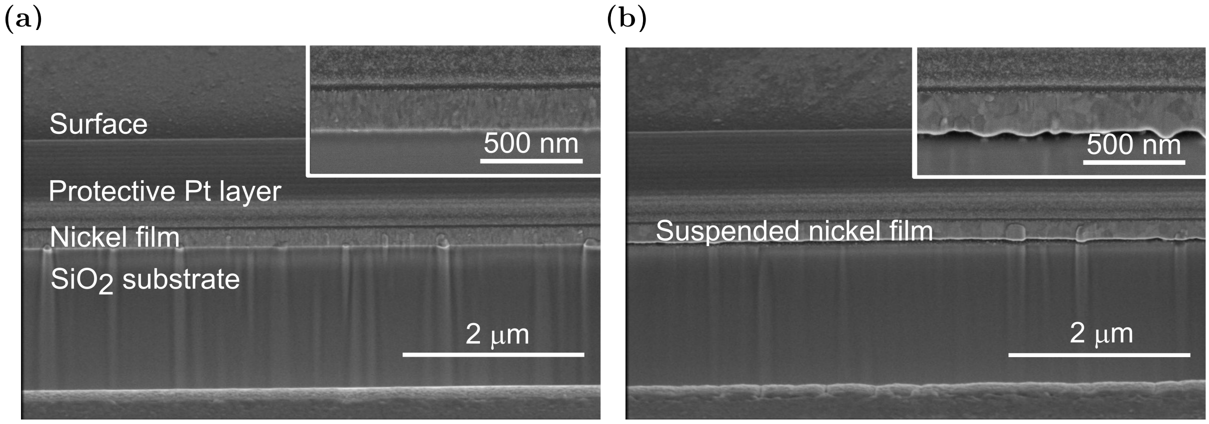

Figure 4.4: *SEM image of cross-section cuts of both film, (a), and cavity, (b). The insets show a magnified image of these transversal cuts where a different crystal structure is observed. This figure is reproduced from reference [73], licensed under a Creative Commons Attribution (CC BY) license.*

4.2 Experimental and numerical analysis

In this section, we present a comprehensive investigation of the opto-acoustic dynamics in free-standing nickel cavities fabricated upon laser delamination, combining experimental measurements supported by computational methods. Time-resolved pump-probe spectroscopy is employed to measure the transient reflectance variations resulting from laser excitation, enabling the detection of coherent acoustic dynamics (Subsection 4.2.1). To analyze the vibrational modes contributing to the acoustic wavepacket, Fourier transform analysis (FFT) was applied to the measured temporal signals. These results were complemented by finite element multiphysics simulations, which provide insight into the eigenmode structure, damping behavior, and energy confinement within the cavity compared to reference nickel film on a substrate (Subsection 4.2.2). The combined experimental and numerical approach allows us to assess the mechanical quality of the fabricated structures.

4.2.1 Time-resolved reflectivity measurements

To experimentally excite, pump, and track, probe, the opto-acoustic dynamics of the bare film and cavity, we have used the custom-made pump-probe scheme discussed on Section 3.4. Both pump and probe are focused on the sample, either the nickel film or a single cavity, with the help of the reflective objective included in the experimental setup (see Figure 4.5 (a)). In this way, it can be confirmed that we are probing the desired area. To verify the specific dimensions of both of our beams, we have retrieved the beam profile at the sample position of the pump (left) and the probe (right), shown in Figure 4.5 (b). The lateral dimensions indicate a spot size of approximately 20 μm for the pump and 5 μm for the probe beam. Having such small spot sizes is necessary to isolate the opto-acoutic response of just a single cavity, whose dimensions have already been described in Figure 4.3.

From a descriptive point of view, once the pump hits the sample at the air-nickel interface, it causes a thermally induced expansion generating a time-dependent strain that travels back and forth along the nickel film/cavity, depending on the structure that has been pumped. The second laser pulse, the probe, studies the propagation and the subsequent reflections of this acoustic pulse along each structure till decay. This is sketched in Figure 4.6. The pump-induced change

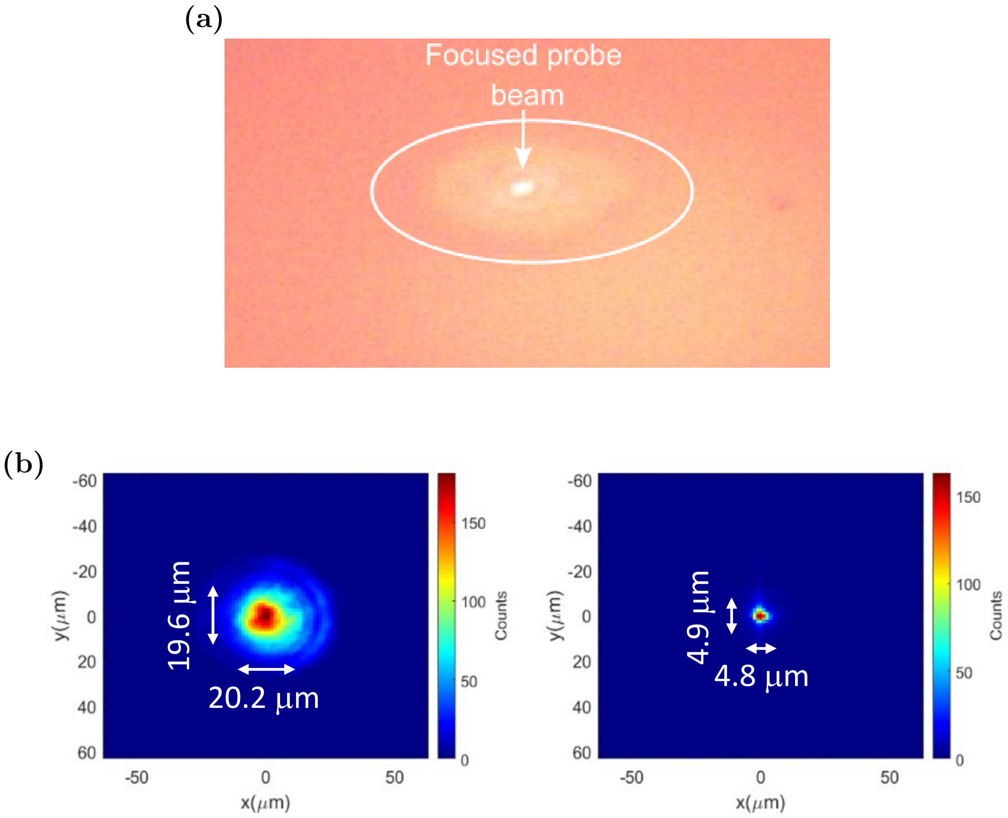

Figure 4.5: (a)Top view image of a cavity, circled in white, taken with the reflective objective included in the experimental setup. This image proves we are probing the center of the structure, the focused probe beam is also indicated in the image. (b) Beam profile image of pump (left) and probe (right) at the sample position. The lateral dimensions of each focused beam are indicated in white.

in transient reflectivity is defined as:

$$\frac{\Delta R}{R} = \frac{R_t - R_0}{R_0} \tag{4.1}$$

where R_t denotes the reflectance after excitation at a certain pump-probe time delay and R_0 the system steady-state reflectance.

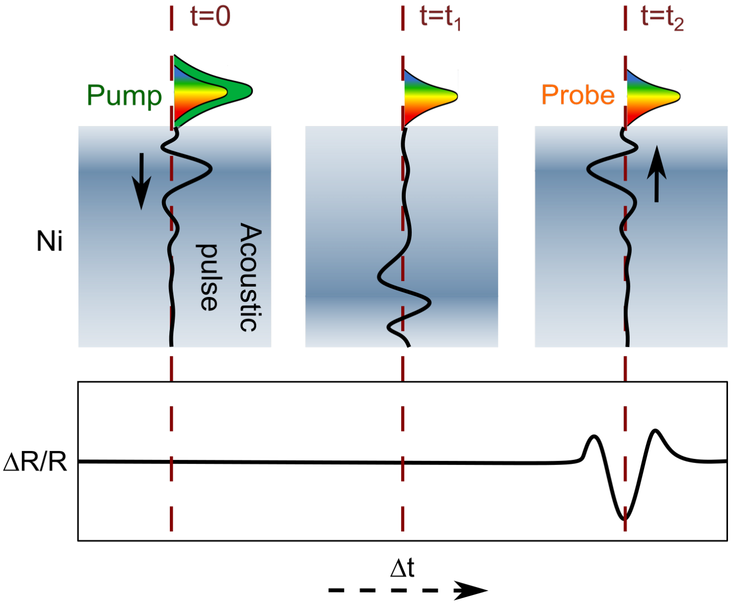

Figure 4.6: *Sketch of the differential reflectance change ($\Delta R/R$) of a nickel thin film. The opto-acoustic response dynamics is tracked as function of pump-probe time delay (ΔT). At t=0, the pump pulse thermally excites the nickel as result, an acoustic pulse is generated and and propagates throughout the nickel (t=t_1). The acoustic pulse is reflected at the sample interface and comes back where the change of reflectance is detected, after each round trip, by the probe beam (t=t_2).*

More specifically, as pump beam we use the SHG (515 nm), of the laser fundamental (1030 nm), modulated at half repetition rate, 50 kHz. As probe, we use a WLSC which provides a broadband pulse from 500 up to 950 nm, modulated at 100 kHz. The results presented here were performed with a pump fluence of 5 mJ$/cm^2$. This value was set after a fluence-dependent pump-probe measurement was performed in a single cavity, under the same conditions, until saturation. These fluent-dependent measurements are presented in Figure 4.7. For fluence values higher than the saturation limit, some damage could be observed on the surface of the cavity.

In Figure 4.8 (a) we show the transient reflectance measurements performed for a cavity, in red, and film, in blue, measured under identical excitation conditions. In both cases, the acoustic mode traveling back and forth along the nickel result in equidistantly separated echoes.

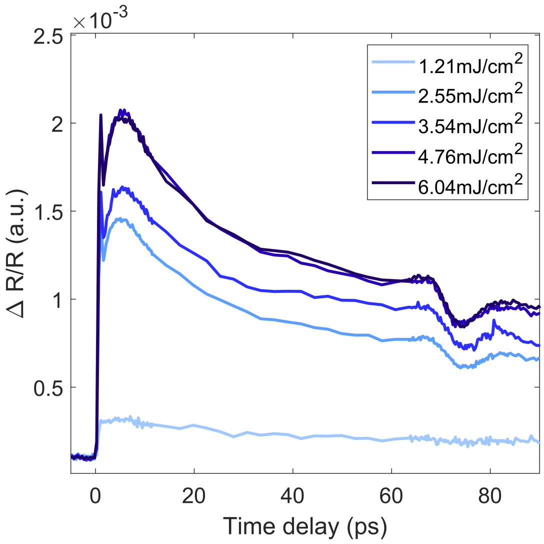

Figure 4.7: *Fluence-dependent pump-probe measurement performed on a single nickel cavity. Saturation limit is reached for a fluence value close to 5 mJ/cm*^{2}.

These echoes are the result of the pump thermal excitation of the first 30-50 nm of material (the penetration depth of the pump pulse, 515 nm, is shorter than the nickel thickness). This local thermal excitation triggers longitudinal acoustic waves that will travel along each of the structures until decay. More precisely, once the longitudinal acoustic wave is generated on the surface, it will reach the lower boundary, Ni/air (cavity) or Ni/SiO_2 (film), where it will be reflected back to the first boundary, Ni/air, where the probe pulse detects the acoustic strain effect on the transient optical response. Therefore, the periodicity of these echoes is directly related to the material thickness and the sound velocity in nickel. For given thickness of 230 nm, in both cavity and film structures, and a sound velocity of longitudinal acoustic waves of 6.04 nm/ps [74] we get a periodicity of 76 ps. Looking again at Figure 4.8 (a), this number matches in the case of the film however, a slight delay of a few picoseconds, around 3, is observed in the cavity case. This means a shorter round trip, our first guess is that this delay can arise from a thinning of the nickel during the cavity fabrication process although this is difficult to verify considering it goes below the resolution of the performed SEM measurements. Additionally, and as previously observed and discussed in Figure 4.4, the formation of large crystal structures after the cavity fabrication could induce a slight change in the sound velocity for the cavity case [75]. In order to isolate the acoustic echos of both structures, we have filtered out the exponential decay contribution mainly attributed to electron-electron and electron-phonon scattering. As indicated, the film is fitted with an exponential of third order, and the cavity with an exponential of second order.

Furthermore, a second baseline removal fitting was performed accounting for possible artifacts induced by the long scanning delay line. More specifically, a polynomial correction was applied to completely isolate the acoustic response in this way. This is represented in Figure 4.8 (b), where for better data visualization the curve corresponding to the nickel cavity has been displaced, the zero level is indicated by a purple dashed line. Each echo was individually fitted with a decaying sinusoidal, and the resulting fits were superposed to serve as a guide to the eye. The overall fitted curve is shown in the figure as a continuous line. For a time delay of 480 ps, up to six acoustic echoes are observed in the cavity whereas five for the film case, suggesting a weaker damping of the acoustic pulse in the cavity than in the film. We have performed a Fourier analysis of the experimental data of both structures to further compare and understand the differences between the acoustic response propagation and damping. This analysis is described in next Subsection 4.2.2.

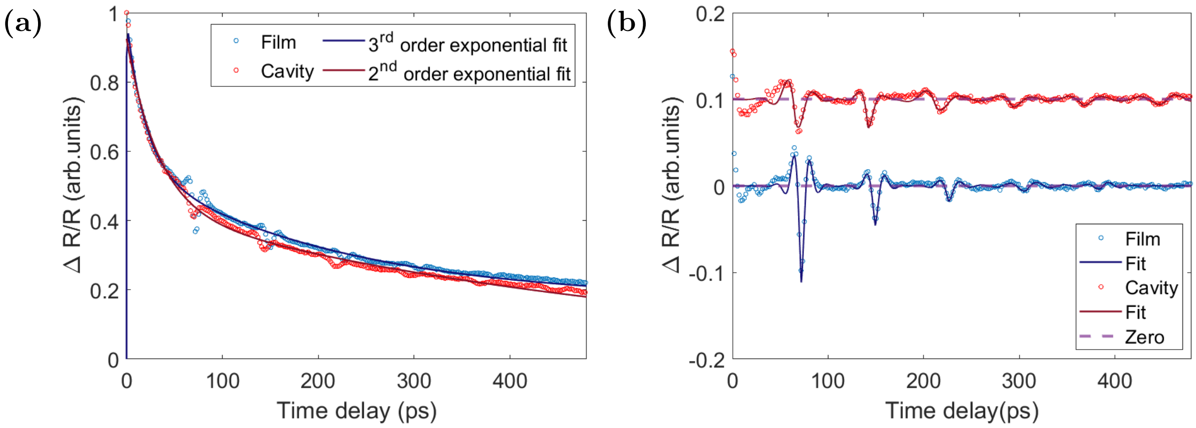

Figure 4.8: *(a) Experimental transient reflectance measurement of the film, in blue, and cavity, in red, plotted using circled markers. The baseline exponential fit is plotted as a continuous in blue and red, respectively for film and cavity. (b) Transient reflectance measurements after baseline removal for isolation of the opto-acoustic response. Again, the experimental data is plotted using circled markers and the fit, a superposition of decaying sinusoidal (following a similar procedure to the one used in Eq. 14 [60]), with a solid color line.*

Following the same measurement parameters and performing the same data analysis, we measured the transient reflectance of four more different cavities placed in the same line of structures as the one just described. These measurements are plotted in Figure 4.9. For reference, the red curve represents the same cavity as before. For visualization purposes, each pump-probe trace has been displaced one above the other with enough separation to independently visualize the response of each structure.

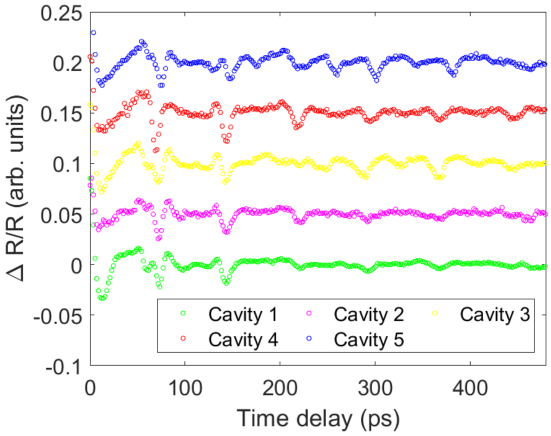

Figure 4.9: *Experimental transient reflectance of five identically fabricated cavities. As reference, the "Cavity 4" curve corresponds to the same cavity of previous figures.*

Although the fabrication process demonstrated a high degree of reproducibility in terms of cavity geometry and dimension, by looking at the experimental data, several differences in the transient reflectance response from cavity to cavity are observed. These differences are likely linked to local changes in the crystal structure at the nickel–substrate interface introduced during laser delamination, as previously noted in the analysis of Figure 4.4. Such variations can result in subtle shifts in the acoustic damping, mode lifetimes, or signal amplitude in the pump–probe measurements; see Appendix B for a more detailed discussion. Thus, more optimization studies are needed to control the microstructure and roughness of the produced membranes to allow for a good reproducibility of the structures. This remains a future suggestion for next studies therefore, to ensure a clear and consistent interpretation of the data, the present study focuses on the opto-acoustic analysis of a single representative cavity.

4.2.2 Analysis of the acoustic eigenmodes

To complement the experimental measurements and further compare the opto-acoustic response of cavity and film configurations, we performed a Fast Fourier Transform (FFT) of the transient reflectivity curves. The resulting spectra are shown in Figure 4.10, with the cavity and film data represented in red and blue, respectively. In both cases, a series of well-defined peaks is observed, each corresponding to the acoustic eigenmodes contributing to the coherent acoustic wavepacket propagating in the structures. In the case of the cavity, panel (a), up to five distinct peaks are identified, while for the film, panel b, six peaks are distinguished. Notably, the cavity response is dominated by lower frequency modes, indicating stronger confinement and reduced damping relative to the film-on-substrate configuration.

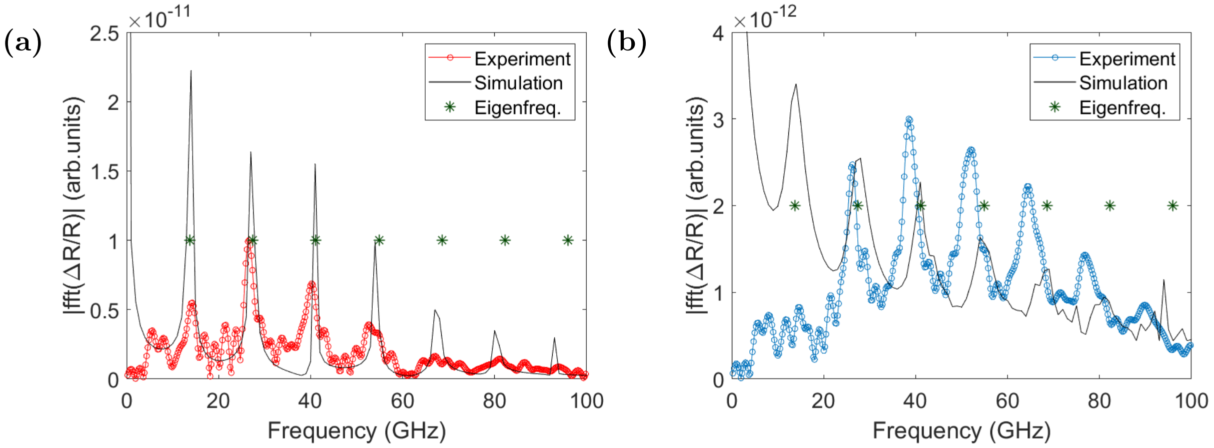

Figure 4.10: *Modulus of the Fourier transform of the experimental pump-probe reflectivity for the freestanding nickel cavity (a) and the nickel film on substrate (b). Asterisks indicate the expected eigenfrequencies of longitudinal acoustic modes, calculated using a sound velocity of 6.04 nm/ps and assuming a perfectly homogeneous nickel layer with a thickness of 230 nm. The continuous lines are the results from the numerical multiphysics simulations calculated with FEM.*

To identify and interpret these spectral features, an opto-thermo-mechanical multi-physics model, solved with Finite Elements Method (FEM) implemented in *COMSOL Multiphysics®* has been developed by Marco Gandolfi [76]. In order to do so, the cavity is treated as a homogeneous nickel layer of thickness h with free external faces. Under this approximation, the eigenfrequencies satisfy the following relation [77]:

$$f_n = \frac{v_l}{2h} n, \quad n = 1, 2, 3, \ldots \tag{4.2}$$

where v_1 is the longitudinal sound velocity. The film was modeled as a nickel layer deposited on top of a semi-infinite $\mathrm{SiO_2}$ substrate. In this configuration, mechanical energy is partially transmitted into the substrate, resulting in complex eigenfrequencies $\tilde{f}$, whose imaginary part represent the acoustic damping. Since the acoustic impedance of Ni, ($\mathrm{Z_{Ni}} = 5.37$ kg m^{-2} s^{-1}), is higher that of the $\mathrm{SiO_2}$, ($\mathrm{Z_{SiO_2}} = 1.31$ kg m^{-2} s^{-1}, the real part of the eigenfrequencies obeys Equation 4.2 as well [78]. The estimated eigenfrequencies for both models are highlighted as green asterisks in Figure 4.10. Their strong agreement with the experimentally observed peaks confirms that the measured modes correspond to confined longitudinal acoustic waves propagating in both the freestanding cavity and the film.

Considering the same parameters as in the experiment, pump wavelength and fluence, the model also enabled the extraction of the electronic and phononic temperature dynamics within the nickel. Due to the limited optical penetration depth of the pump pulse, less than 30 nm in nickel, energy deposition is highly localized. Immediately after pump photoexcitation, the electronic temperature rapidly rises, reaching values up to 800 K in the irradiated region. Subsequently, energy is transferred from the electrons to the lattice (phonon) system, causing the phononic temperature to increase, reaching approximately 150 K within the first 2 ps after excitation (see Figure 4.12). After this time, this localized heating results in the thermal expansion of the Ni top region, triggering the generation of a coherent acoustic pulse that propagates through the structure till the bottom Ni interface where it will be back reflected. In the film configuration, the acoustic wave reaches the Ni/SiO_2 interface, where it is partially reflected due to the mismatch in acoustic impedance. In contrast, for the freestanding cavity, the pulse reflects off the Ni/air boundary, leading to near-total reflection. Following reflection, the acoustic wave propagates back towards the top interface, where it reenters the optically sensitive region ($<$30 nm), enabling detection by the probe pulse as a transient change in reflectivity. This is schematically represented in Figure 4.11.

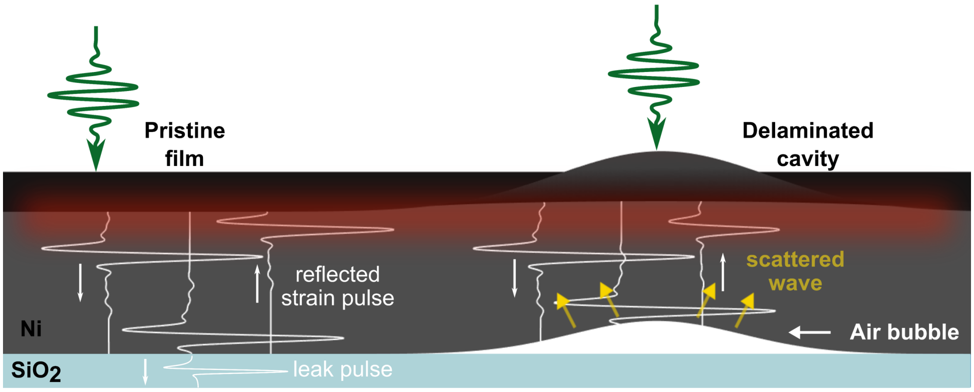

Figure 4.11: Sketch of the excitation of an acoustic pulse in the pristine film/delaminated cavity after interaction with the pump pulse (green). The pump-induced localized heating (red) generates thermoelastic stress, launching acoustic phonons which propagate through the film or across the cavity interface. The sketch illustrates the subsequent acoustic reflection, mode confinement, and damping due to energy leakage or scattering at boundaries. This figure is adapted from reference [73], licensed under a Creative Commons Attribution (CC BY) license.

The FFT of the longitudinal displacement, calculated using finite element method (FEM) simulations, is overlaid as a black solid line in Figure 4.10, panels (a) and (b), for the cavity and film, respectively. These simulations show good qualitative agreement with the experimental Fourier spectra, reproducing the main spectral features observed in both configurations. However, small discrepancies are observed between the experimentally extracted eigenfrequencies and the simulated results. These differences are likely due to the idealized assumptions made in the simulations, which consider a perfectly homogeneous polycrystalline nickel film. In reality, as noted earlier, the cavity presents significant crystalline irregularities introduced during the laser fabrication process, leading to local variations in sound velocity. Grain boundaries, defects, and micro-structural inhomogeneities affect both the propagation and reflection of acoustic waves. These imperfections, which are not included in the model, contribute to a lower effective sound velocity, consistent with findings in recent studies [79].

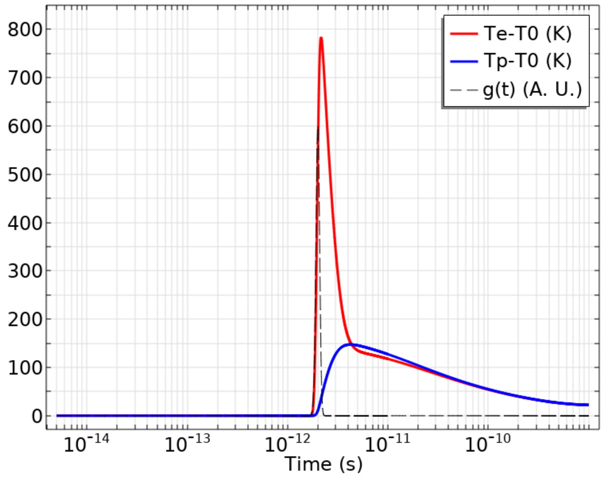

Figure 4.12: *Simulated temporal evolution of the electronic (red) and phononic (blue) temperatures calculated at 10 nm below the top air/Ni interface after pump excitation. The black dashed line, included for reference, shows the temporal profile of the laser pulse.*

To better understand the relative contributions of individual eigenmodes to the acoustic pulse envelope propagating in both the cavity and film configurations, we performed a Fourier analysis of isolated acoustic echoes. Specifically, we manually selected the first five echoes in each time-domain signal by defining time windows centered around the minimum of each echo then, computed the FFT of each selected region independently. This approach allowed us to extract information about the temporal evolution of each eigenmode, how its amplitude and damping change over successive round-trips. The resulting FFT spectra were normalized to the sum of all selected echo FFTs to enable direct comparison across time. The corresponding spectra are shown in Figure 4.13 (a) for the cavity and in Figure 4.14 (a) for the film. For reference, the FFT of the entire experimental time trace is overlaid in both plots as continuous lines in red and blue, respectively. From this global spectrum, we selected specific frequencies (shown as vertical lines), five for the cavity and six for the film, corresponding to the prominent acoustic modes. These frequencies serve as markers to extract the relative amplitude of each mode across the individual echo FFTs. The extracted amplitude values for each mode were then plotted as a function of time in panels (b) of Figure 4.13 and Figure 4.14, cavity and film respectively. A single-exponential decay function was fitted to each data series, from which we obtained the mode-specific damping constants (represented in panels (c)) and initial amplitudes (represented in panels (d)), along with their associated error bars extracted from the fit residuals. This analysis quantifies the attenuation dynamics of each mode and provides a clear spectral signature of the differences in energy dissipation between the two configurations.

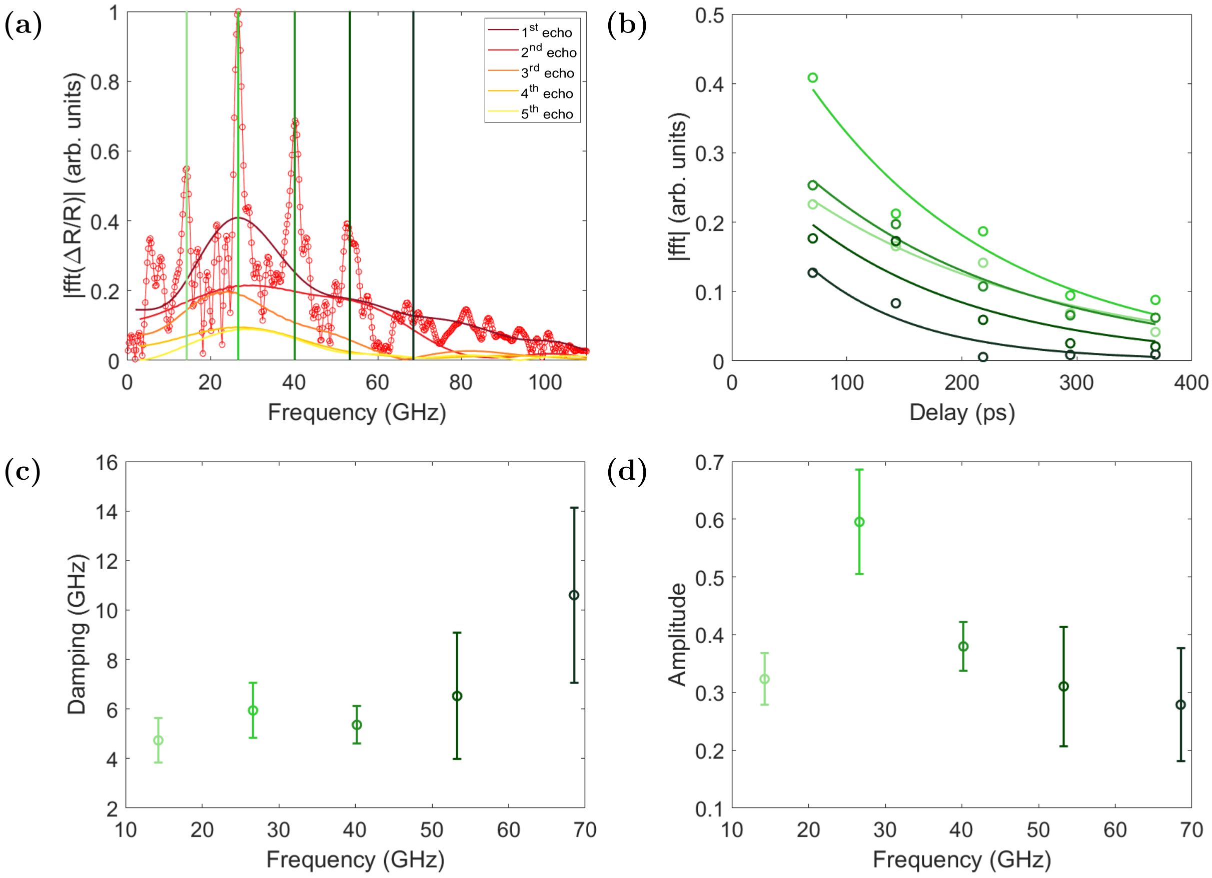

Figure 4.13: *(a) Fourier transform (FFT) of the full experimental time-domain reflectivity (Figure 4.10(a)), overlaid with the FFTs of the first five isolated acoustic echoes from the cavity. (b) Amplitudes of the selected FFT peaks at specific eigenfrequencies, plotted as a function of time delay. The continuous lines represent exponential fits to the amplitude decay. (c) Extracted damping constants for each eigenmode based on the exponential fit. (d) Corresponding initial amplitudes of each mode, obtained from the same fit.*

Clear differences emerge when comparing the Fourier analysis of the cavity and film structures. The most evident contrast is the significantly weaker damping observed in the cavity case, consistent with the greater number of acoustic echoes visible in the time-domain pump–probe trace (see again Figure 4.10). This behavior is likely due to the higher internal reflectivity of the acoustic wavepacket at the Ni/air interface, which effectively confines the energy within the freestanding membrane and minimizes leakage. The cavity response is dominated by low-frequency modes, as shown in Figure 4.13 (a), while the film's acoustic response shows a stronger presence of higher-order eigenmodes (Figure 4.14 (a)). This is consistent with the narrower temporal profile of the strain pulse in the film, where higher-frequency components result in a more compressed acoustic wavepacket. In contrast, the broader temporal profile in the cavity suggests stronger low-frequency content and longer pulse durations. Regarding mode amplitudes, the film exhibits generally higher initial amplitudes than the cavity. One possible explanation is again related to the crystallinity of the nickel film post fabrication. The formation of larger crystal grains during the laser delamination process in the cavity may introduce surface roughness and structural inhomogeneities, which in turn could cause temporal jitter or pulse broadening upon reflection at the cavity interfaces. This effect would reduce the coherence and amplitude of the confined acoustic modes. Similar observations have been reported in previous studies, where broadening of picosecond acoustic pulses was linked to increased surface roughness [80]. These imperfections likely contribute to faster attenuation of high-frequency components, reinforcing the dominance of low order modes in the cavity configuration. In Appendix A we show an alternative analysis approach. There, instead of analyzing the individual echoes as done here, we decompose the pump-probe traces into a series of damped acoustic oscillators. This provides an alternative way to extract the damping, amplitude and frequency values for the various eigenmodes of the film and cavity. Remarkably, the results we obtain following this second approach agree well with the analysis reported here, providing a further validation of our findings.

4.3 Conclusions

In this work, we performed an ultrafast pump–probe spectroscopy study of coherent acoustic phonons excited by femtosecond laser pulses and confined within freestanding nickel cavities fabricated via laser delamination. By comparing these structures to reference nickel thin films on SiO_2 substrates of identical thickness (230 nm), and combining Fourier transform analysis with finite element numerical simulations, we demonstrated that the freestanding cavities exhibit

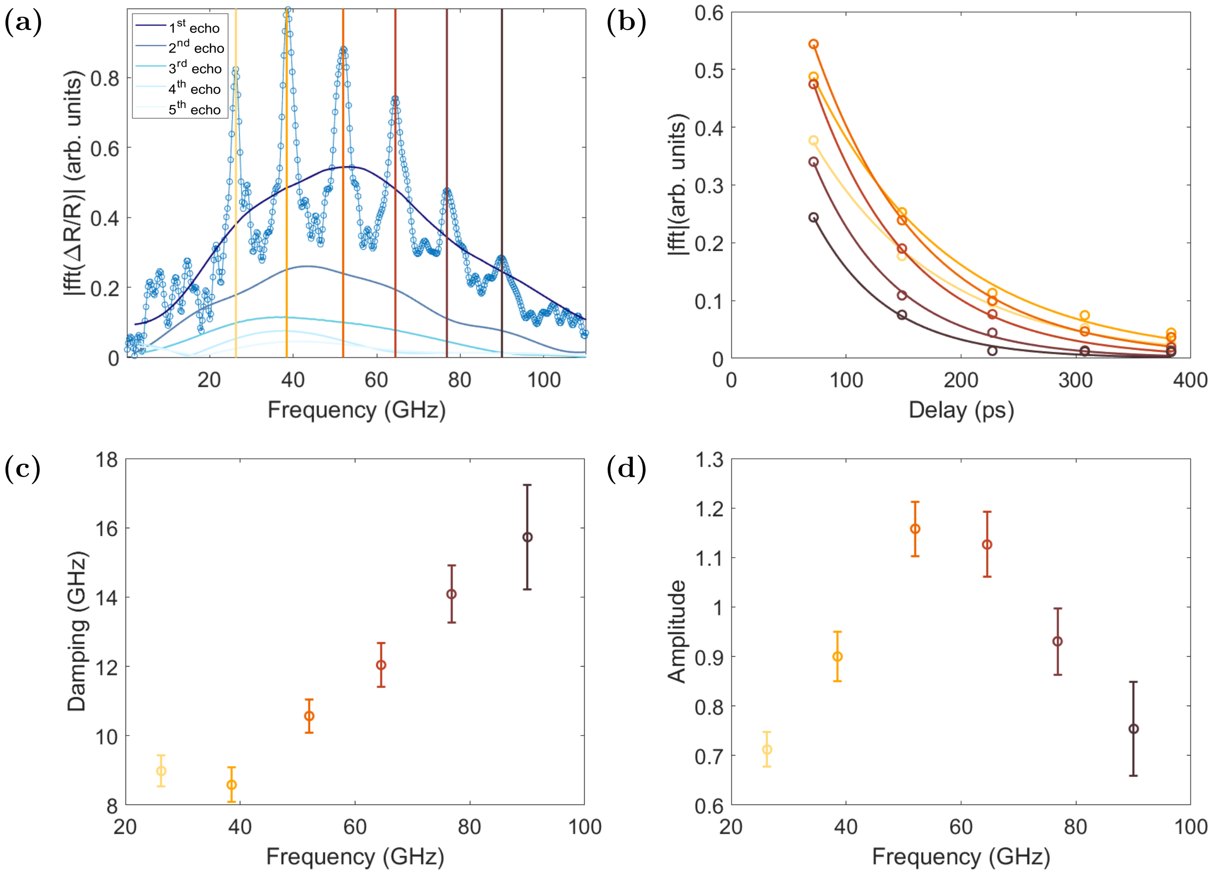

Figure 4.14: *(a) Fourier transform (FFT) of the full experimental time-domain reflectivity (Figure 4.10(b)), overlaid with the FFTs of the first five isolated acoustic echoes from the film. (b) Amplitudes of the selected FFT peaks at specific eigenfrequencies, plotted as a function of time delay. The continuous lines represent exponential fits to the amplitude decay. (c) Extracted damping constants for each eigenmode based on the exponential fit. (d) Corresponding initial amplitudes of each mode, obtained from the same fit.*

markedly reduced acoustic damping and more persistent phonon confinement. This difference is attributed to the nearly total internal reflection of the acoustic wavepacket at the Ni/air interface in the cavity, in contrast to the energy leakage into the substrate observed in the supported film.

Although further work is needed to optimize the crystallinity and surface roughness of the cavity that influence high-frequency damping, the current results show that laser delamination offers a simple, scalable, and mask-free alternative for fabricating high-performance nano-acoustic resonators. These freestanding metal cavities are not only relevant for fundamental studies of picosecond acoustics, but may also serve as a viable platform for GHz-range RF filters, often referred to as thin-film bulk acoustic resonators (FBARs) [81], already used in mobile communication devices, but with simplified fabrication.

Finally, the fact that these cavities are composed of a ferromagnetic material (nickel) opens exciting opportunities for exploring multi-physics coupling phenomena, such as magneto-acoustics, magneto-photonics, and ultrafast magnetization dynamics. The combination of magnetic functionality and opto-acoustic performance makes these structures a promising playground for future studies in hybrid nanoscale devices [82].

5

Opto-acoustics in resonantly pumped MIM cavities

In last Chapter 4 we have reported on the enhancement of opto-acoustic properties of thin nickel films obtained via ps-laser delamination. As already discussed, optimized propagation of acoustic waves in a ferromagnetic material like nickel might lead to control of magnetization dynamics on ultrafast timescales via the magnetostrictive effect. In fact, low-damping of acoustic modes is a necessary condition to achieve efficient transfer between phononic and magnonic resonances. In this context, an interesting approach is to separate the material platform where the acoustic and magnetic resonances are excited, for example stacking a ferromagnetic layer on top of a non-magnetic resonator with optimized opto-acoustic performance. Such approach would have two main advantages. First of all, it would allow to separately optimize the acoustic and magnetic degrees of freedom on different systems. Moreover, in such design the laser-driven excitation of the acoustic pulse would take place on a non-magnetic material, reducing spurious thermal effects on the induced magnetization dynamics. In this context, the investigation of resonators based on epsilon-near-zero materials (systems where the real part of the dielectric function is nearly zero at specific wavelengths), represent a promising candidate to achieve efficient excitation of acoustic modes. Epsilon-near-zero (ENZ) conditions occur naturally in certain materials like transparent conductive oxides [83]. However, these systems offer limited tunability of the spectral position of the ENZ mode. To overcome this, metal-insulator-metal (MIM) nanocavities have recently drawn significant attention. In fact, these metamaterials host epsilon-near-zero modes that can be tuned at will by modifying the thickness of the different layers [84] [85] . Because of the resonant light-matter coupling taking place at the ENZ modes of MIM cavities, we expect that efficient excitation of acoustic modes can be achieved in these structures. To assess this, in this chapter we use pump-probe transient reflectivity spectroscopy to investigate the interplay between the ENZ and acoustic modes in MIM cavities consisting in silver (Ag) - insulator (Al_2O_3) - silver multilayers.

The analysis of these cavities is similar to the one performed in Chapter 4. There we used an intense optical pump pulse to excite an acoustic wave in a nickel cavity. The acoustic pulse was then monitored through transient changes in the reflectivity of the sample, using a weak probe beam with variable delay. Finally, we performed a Fourier analysis to gain insight about the propagation of each acoustic mode sustained by the cavity. Compared to previous chapter, where the pump excitation was non-resonant with the nickel cavities, here we design our pump pulse to be resonant with one of the ENZ resonances of our MIM system, exploiting the wavelength tunability of the optical parametric amplifiers discussed in Chapter 2. This allows us to enhance the opto-acoustic response of these systems, offering a promising physical platform for future combination of opto-acoustic resonators and magneto-optical materials.

5.1 Epsilon-near-zero (ENZ) cavities

Over the years natural epsilon-near-zero mode materials have found wide applications in several fields such as ultrafast amplitude or polarization switching, third harmonic generation (THG) and the realization of strongly coupled systems. Recently, artificially fabricated ENZ, such as the nanocavities described here, have shown a particular interest for presenting more than one ENZ frequency, the possibility of exciting these modes either with both transverse magnetic (TM) or transverse electric (TE) polarized light, and their easy tunability of their spectral region by changing the thickness of the dielectric material.

Our MIM cavity can be defined as an engineered multilayered metamaterial that supports ENZ modes. This metamaterial is conformed by a glass substrate, 130 nm of silver (Ag) on top, 435 nm of aluminum oxide (Al_2O_3) and 30 nm of silver as upper layer. This stack configuration has been designed based on previous results by Kuttruff et al. [67] where the ultrafast reflectance modulation of a similar material stack was studied. It is important to note that by modifying the insulator thickness one can control the resonance spectral position; a thinner insulator will blue-shift the resonance, whereas a thicker one will red-shift it. Not only does modifying the geometry affect the final cavity performance, but the choice of metal also plays a significant role. Silver, in our case, offers low optical losses in the visible and near-IR spectral ranges but has the disadvantage that it oxidizes over time. Having considered these tunable parameters, the fabrication process was performed through electron beam evaporation in the case of the metal (Ag). This is a widely used physical evaporation technique commonly employed for depositing metal thin films allowing a precise control of the material thickness. For the deposition of the insulator material, the technique used was sputtering. After fabrication, each layer thickness was measured using a quartz microbalance, verifying that the fabricated sample matches the design. The sample presented and here characterized was fabricated by Garoli et al. at the *Istituto Italiano di Tecnologia*. To verify the expected resonances positions after sample fabrication, a reflectance measurement at normal incidence was performed and the results are plotted in Figure 5.1.

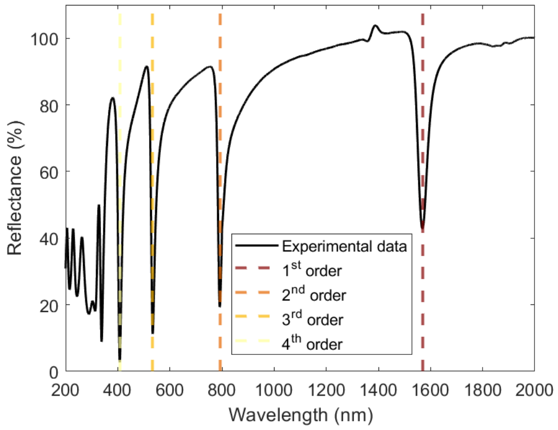

Figure 5.1: *Experimental steady-state reflectance of the MIM cavity at normal incidence, plotted in black. The vertical dashed lines indicate the different Fabry-Perot modes supported by the cavity.*

The reflectance spectrum reveals up to four sharp absorption dips corresponding to the different optical modes supported by the cavity. The first dip around 400 nm corresponds to the natural ENZ mode of Silver, also known as a Ferrell-Berreman mode [84]. In particular, we are interested in studying the ones in the visible and near-IR region, therefore the 2^{nd} and $3^{rd}d$ order Fabry-Perot modes, centered at 792 and 534 nm, respectively. Both of these resonances exhibit strong photon absorption, up to 80%, being the at 792 nm the one with larger width.

5.2 Experimental analysis

To understand the complex interplay among the optical resonances, the differential reflectance variation and the photoinduced acoustic response in the MIM cavity, a series of ultrafast pump-probe spectroscopy measurements were performed. These experiments targeted the visible and

VIS-NIR optical resonances supported by the cavity and are discussed in this section. Particular attention is given to the pump polarization and spectral selectivity. By tuning the pump wavelength and carefully controlling the incident polarization, using both s- and p-polarized configurations, we selectively excited different resonant modes and probed their ultrafast reflectance dynamics. These results are presented in Subsection 5.2.1.

To further interrogate the dynamics beyond the initial electronic response, long time-delay scans up to 400 ps were performed together with a Fast Fourier Transform (FFT) analysis, presented in Subsection 5.2.2, to extract the dominant acoustic frequencies.

5.2.1 Time-resolved reflectivity measurements

In addition to the steady-state reflectance characterization discussed in previous Section 5.1, time-resolved pump-probe spectroscopy was performed on the already presented MIM cavity to investigate its ultrafast optical and opto-acoustic responses. Therefore, we provide insights into both short dynamics (on the order of few picoseconds) and longer relaxation processes (hundreds of picoseconds), providing a deeper understanding of the light-matter interactions supported by the cavity. Our analysis focuses only on the dynamics of the modes in the visible and near-infrared regions, corresponding to the third and second order Fabry-Perot modes.

The pump-probe spectroscopy setup used to carry out the measurements below presented is conformed by a visible or VIS-NIR OPA as pump, depending on the targeted resonance, and a WL supercontinuum as probe. Specifically, to excite the resonance located around 534 nm, we will use the visible OPA while for the one located around 792 nm, we will use the VIS-NIR OPA. Specific details about the setup have already been presented in Section 3.3.1. However, there are several points that one must take into consideration before performing the measurements. Unlike in Chapter 4 where the spot size was crucial for correctly probing our cavity due to its micrometric lateral dimensions, here we do not have such limitation. We therefore relax the focusing conditions on both pump and probe beams, minimizing the risk of damaging the sample. Specifically, the pump spot size is on the order of 65 μm and the probe is around 50 μm. However, the incident beam angle plays an important role for these measurements, since the optical response of the MIM cavity is angle dependent. As previously introduced in the above Section 5.1, the spectral position of each resonance shifts depending on the angle of incidence. Therefore, it was necessary to design a method to verify that we are indeed pumping the desired wavelength regions. From the steady-state reflectance measurement, we obtained information about the spectral positions of each resonance at normal incidence. Based on these results, the sample was mounted in a rotation stage which can be manually tuned. The probe beam reflected from the sample is coupled into the spectrograph, capturing the resonances positions for the selected angle. An overlap of this data, for a small angle of incidence, and the white-light spectrum is represented in Figure 5.2 (a). Once we know the resonance spectral positions we can tune any the of OPAs by slightly changing the phase matching angle. For instance, the pump spectrum used to excite the first observed resonance is plotted in Figure 5.2 (b).

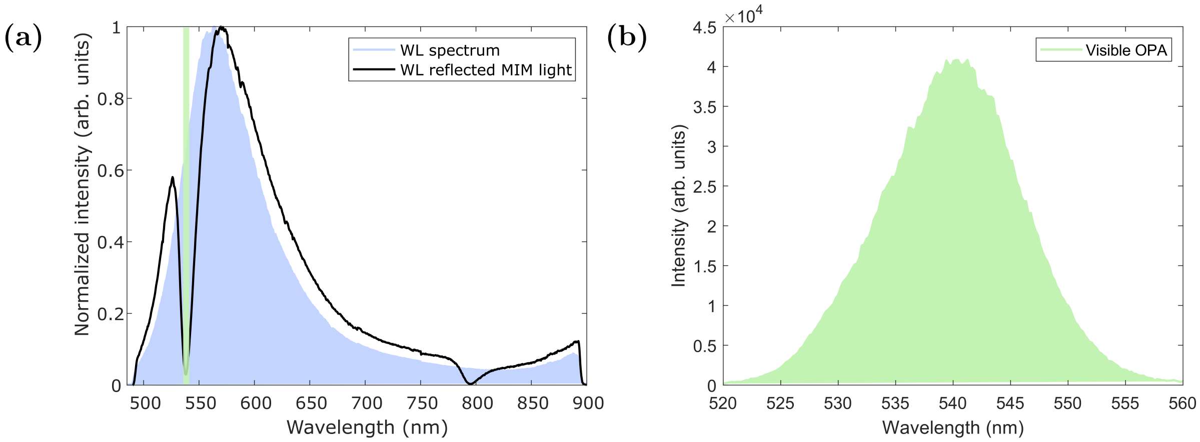

Figure 5.2: *(a) Normalized intensity of the WL spectrum, shown as a blue shaded area. Overlaid is the normalized reflected probe light from the sample (black solid line), where two resonances can be appreciated. The vertical line indicates the first resonance and therefore, the wavelength around which the OPA should be tuned. (b) Spectrum of the visible OPA, tuned to excite the first resonance.*

Having considered these measurement restrictions, we can move to the ultrafast pump-probe spectroscopy results. Following the above Figure 5.2, the first resonance is excited using the s-polarized, visible OPA, centered around 540 nm, with a fluence of 0.5 mJ/cm^2. For probing, we are using the p-polarized, WL supercontinuum (500-900 nm). The probe light covers both resonances, facilitating in this way the detection of possible spectral shifts or resonance broadening induced by the pump beam. The experimental transient reflectance corresponding to the fast dynamics is plotted in Figure 5.3 (a) and in Figure 5.4 (a) the transient reflectance of a longer delay time scan is represented. Additional scenarios, such as different polarization configurations and the case in which the second resonance is pumped, are also considered in this chapter.

Focusing first on Figure 5.3, where the ultrafast time dynamics from 0 to 8 ps is captured. In panel (a), the red color indicates a transient increase of the reflectance, while the blue regions

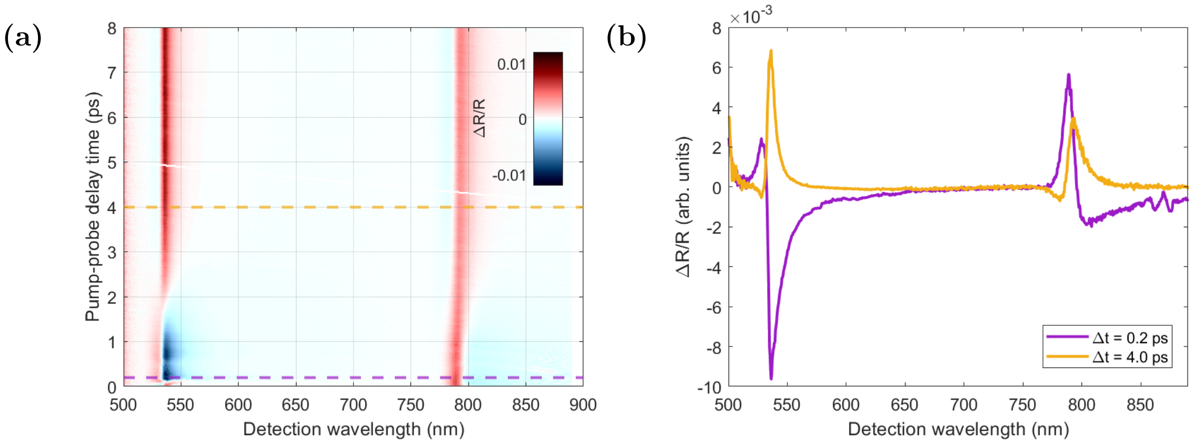

Figure 5.3: *Time-resolved differential reflectance (ΔR/R) of the MIM cavity under s-polarized pump excitation of the* ***first resonance*** *and p-polarized broadband probe. The left panel (a) shows a 2D map of 8 ps delay time across all probe wavelengths. The dashed lines indicate horizontal cuts at specific time delays of 0.2 ps, and 4 ps, plotted in panel (b) in violet and yellow, respectively.*

correspond to either increased absorption or photobleaching. The main feature we observe is an overall increase (red regions) of the reflectance around the second resonance. Also, we observe an intense negative (blue) ΔR/R response lasting the first 2 ps around 540 nm. To gain better insight about the dynamical response of the sample at the two resonant frequencies, we extract two cuts at 0.2 ps and 4 ps, shown in Figure5.3 (b). The short delay cut at 0.2 ps (violet curve) features two positive-negative derivative lineshape centered around 540 nm and 800 nm. Considering the highly asymmetric absorption lineshapes shown in Figure 5.1, we can interpret these results by speculating that, for time delays below 1 ps, pumping the first ENZ mode results in a redshift of both resonances. This is in qualitative agreement with the findings reported in [67], where the few-ps response of a similar MIM structure was investigated and proposed to implement an all-optical switch. In that case, finite-element methods simulations matching the experimental data allowed to attribute the redshift to a local increase of the sample permittivity. In this picture, the effect of the pump pulse is to optically excite electrons in the metallic layer of the MIM cavity. After thermalization due to electron-electron and electron-phonon scattering, a hot thermal distribution of electrons is established. This results in an overall increase of the dielectric function and finally to a spectral shift of the ENZ conditions. While in [67] only the response associated to the low-energy mode of the cavity could be investigated, here we are able to resolve the dynamics of both ENZ resonances. For longer time delays (see cut at 4 ps, orange curve), we observe an overall increase of the reflectance around both ENZ modes. This suggests that, after the initial redshift, the ENZ absorption peaks (see Figure 5.1) are transiently reduced. As expected, among 600 and 750 nm no relevant activity is observed at any specific time delay, since there are no strong resonances present in that range, being the reflectance modulations strongly localized around the two studied resonances.

In Figure 5.4 we investigate how the initial fast electronic dynamics later couples to the acoustic modes of the MIM structure. This is achieved performing a long time delay scan up to 400 ps. The parameters and pump (s-polarized) probe (p-polarized) configuration are identical to those used in previous measurements. In panel (a), a 2D map of the experimental data is shown along with two zoom insets centered on each resonance of interest for a time delay of 200 ps. Similarly to what we observed and analyzed in the previous Chapter 4, we observe the appearance of an optically pump-induced acoustic response. To better visualize these acoustics, panel (b) shows two transversal cuts centered around the wavelengths showing a higher acoustic modulation. At 528 nm, in green, and at 784 nm, in red. Remarkably, the acoustic response is only visible when resonantly probing around the two ENZ modes.

Focusing on Figure 5.4 panel (b), we clearly observe, for each selected wavelength, the appearance of different acoustic components correlated to faster and slower modulations. A detailed Fourier transform analysis addressing the different dominant frequencies for each case is discussed in the following Subsection 5.2.2.

These types of cavities usually exhibit strong polarization dependent coupling, interacting differently with s- or p-polarized light depending on the resonance, specially at non-normal incidence. To investigate the polarization dependence of the resonances in the visible and near-IR ranges, a set of measurements was performed in which the incident pump polarization was changed from s-polarized to p-polarized light. Following this approach, we provide an insight into the different modes symmetry and their coupling efficiency. To rotate the polarization we used a half-waveplate. To account for potential changes in the beam pointing vectors due to the polarization rotation, we performed a fine re-alignment to verify that pump and probe are still overlapping both in time and space. The probe polarization was kept fixed as p-polarized.

To compare these results with those just presented, the used pump fluence was kept at 0.5 mJ/cm^2 with the same angle of incidence. Measurements were carried out for both fast (8 ps) and slow (400 ps) dynamics. These experimental results are shown in Figure 5.5 and Figure 5.6, respectively.

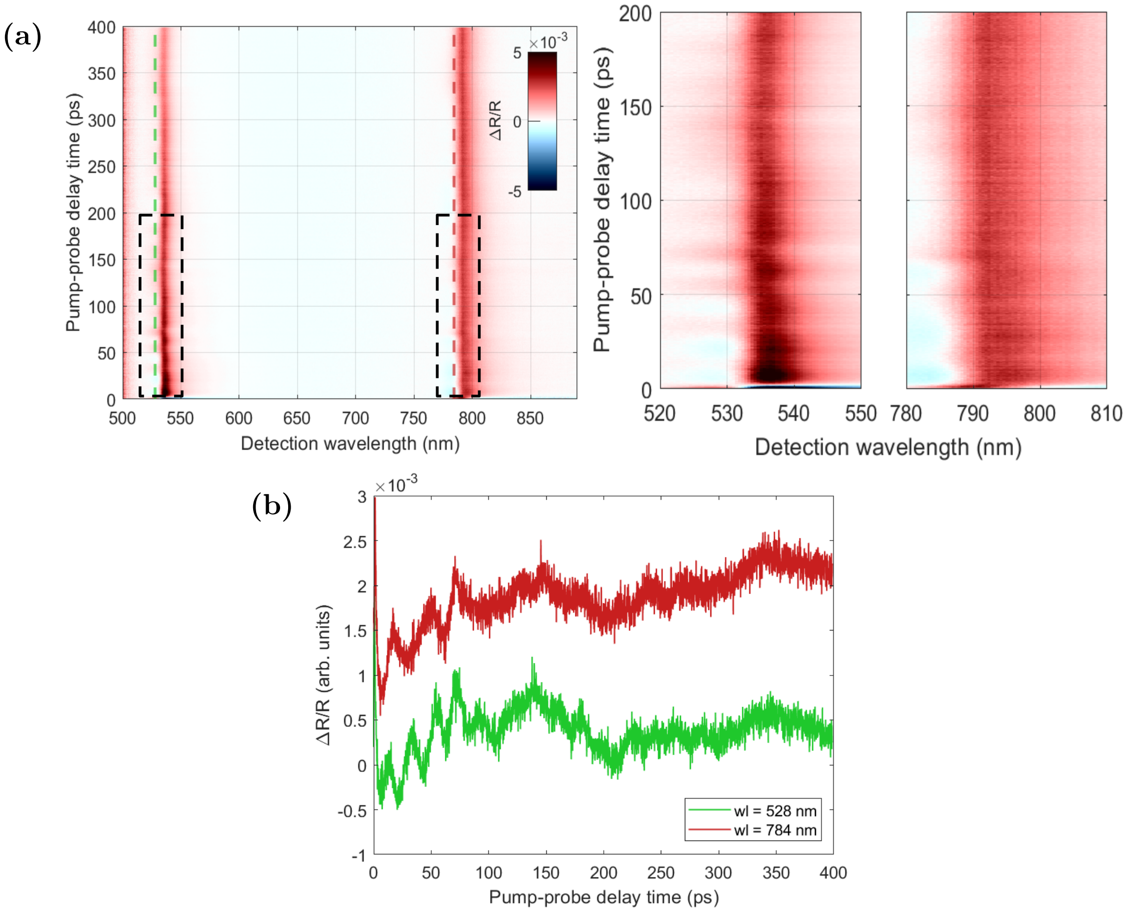

Figure 5.4: *Time-resolved differential reflectance* ($\Delta R/R$) *of the MIM cavity for a time delay of 400 ps, pumping (s-pol.) the* ***first resonance*** *and broadband probing (p-pol). (a) 2D map of the differential reflectance as function of wavelength and time delay, on the left. On the right, two zoom insets of the black dashed regions centered around the two resonances for delay up to 200 ps. (b) Transversal cuts at 528 nm, in green, and 784 nm, in red, extracted from the full 400 ps delay time. For visualization purposes, one plot is displayed with an offset above the other.*

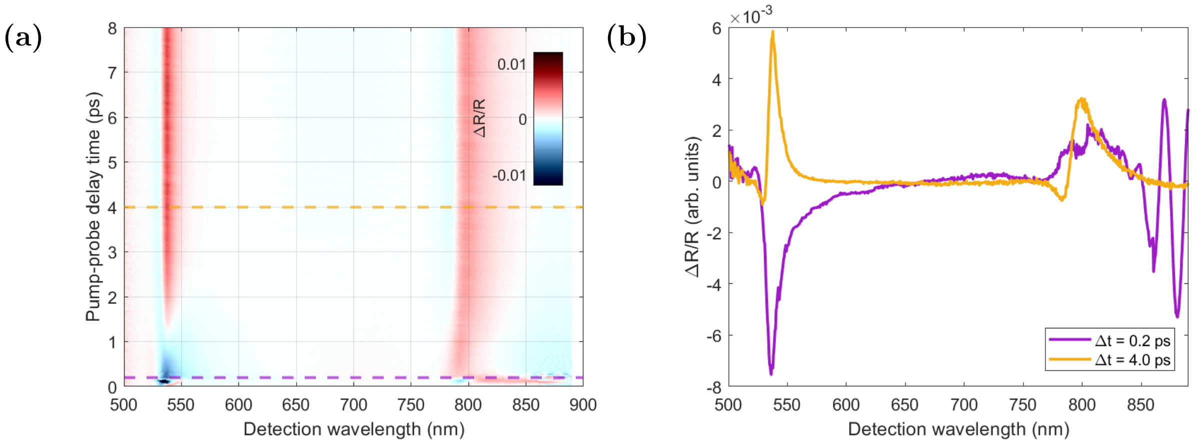

Figure 5.5: *Time-resolved differential reflectance ($\Delta R/R$) of the MIM cavity under p-polarized pump excitation of the **first resonance** and p-polarized broadband probe. The left panel (a) shows a 2D map of 8 ps delay time across all probe wavelengths. The black dashed lines indicate horizontal cuts at specific time delays of 0.2 ps, and 4 ps, plotted in panel (b) in violet and yellow, respectively.*

Looking at the results presented in Figure 5.5 panel (a), we observe that for the first picosecond the differential reflectance is predominantly negative around 540 nm, which differs from the behavior seen in Figure 5.3 panel (a). However, around 800 nm for short time delays and around both resonances for longer time delays, see cut at 4 ps plotted in panel (b), the dynamics appear quite comparable when pumping cross-polarized (Figure 5.3) and same polarized light (Figure 5.5).

To conclude with the polarization dependence analysis, we also tracked the long dynamics using this polarization configuration. Since the dynamics observed in this time frame are mainly acoustic, phonon driven, no significant differences are expected when compared to the cross-polarized pump measurement. The results of this measurement are presented in Figure 5.6.

As expected, from Figure 5.6 panel (b), we observe allmost identical traces to the ones presented in 5.4 panel (b) for both transversal cuts, at 528 and 784 nm. Following the same acoustic dynamics at the same time delays.

These polarization-dependent measurements could be further complemented by angle-resolved spectroscopic ellipsometry, which provides both amplitude and phase information of the reflected (or transmitted) light as a function of the angle of incidence. With this technique, one can retrieve information about the effective refractive index of the MIM cavity as a whole, quantifying its absorption and dispersion. Due to time and equipment constraints, this remains a suggestion

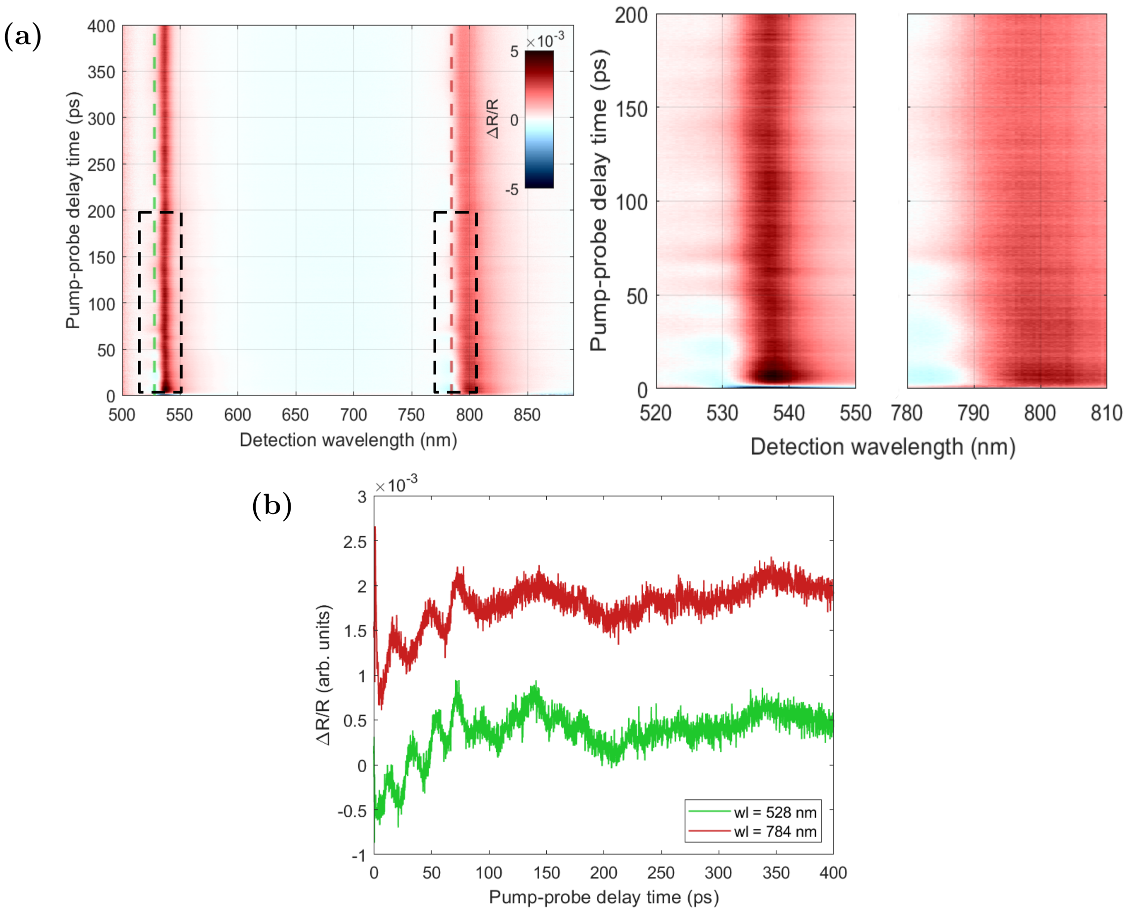

Figure 5.6: *Time-resolved differential reflectance ($\Delta R/R$) of the MIM cavity for a time delay of 400 ps, pumping (p-pol.) the* ***first resonance*** *and broadband probing (p-pol). (a) 2D map of the differential reflectance as function of wavelength and time delay, on the left. On the right, two zoom insets of the black dashed regions centered around the two resonances for delay up to 200 ps. (b) Transversal cuts at 528 nm, in green, and 784 nm, in red, extracted from the full 400 ps delay time. For visualization purposes, one plot is displayed with an offset above the other.*

for a future characterization.

All pump-probe data presented so far was obtained tuning the pump beam around the first ENZ resonance. To explore the selective excitation of the second resonance around 792 nm, we performed additional pump-probe spectroscopy measurements using the VIS-NIR OPA, tuned around 800 nm, as pump. To maintain consistency with previous measurements, the pump beam was s-polarized while the probe beam remained p-polarized. This configuration enables a direct comparison with the previous set of measurements where the first resonance, in the visible range, was excited. For an accurate comparison, we kept comparable fluence values for both pump and probe beams. Analogously to the case presented before, we investigated both fast and slow dynamics by acquiring pump-probe traces over 8 ps and 400 ps respectively. The results of the fast scan are presented in Figure 5.7 (a). To help guiding the discussion we proceed like above and plot two cuts at 0.2 ps and 4 ps in panel 5.7 (b). The differential reflectance around the first ENZ mode features a clear positive-negative derivative trend, again hinting towards a redshift of the resonance frequency. On the other hand, the response around the second ENZ mode appears to be surprisingly structured for the first 0.5 ps. For time delays above 1 ps the differential reflectance signal shows a general increase around the two ENZ frequencies, analogously to what we observed when pumping the first resonance.

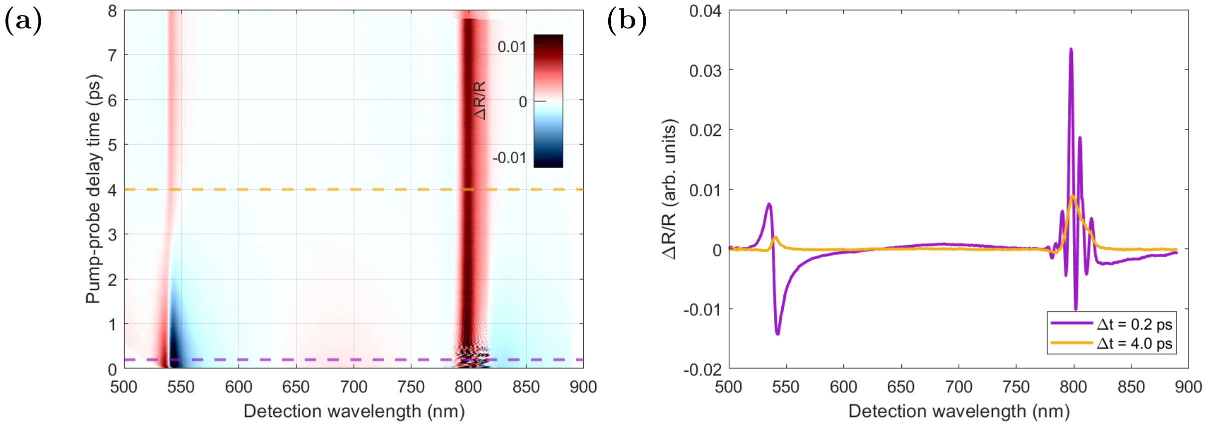

Figure 5.7: *Time-resolved differential reflectance ($\Delta R/R$) of the MIM cavity under s-polarized pump excitation of the* ***second resonance*** *and p-polarized broadband probe. The left panel (a) shows a 2D map of 8 ps delay time across all probe wavelengths. The black dashed lines indicate horizontal cuts at specific time delays of 0.2 ps, and 4 ps, plotted in panel (b) in violet and yellow, respectively.*

The long delay times dynamics are represented in Figure 5.8. Analogously to the case discussed above, the long scan shows a periodic modulation of the pump-probe trace, indicating the excitation of acoustic eigenmodes within the cavity.

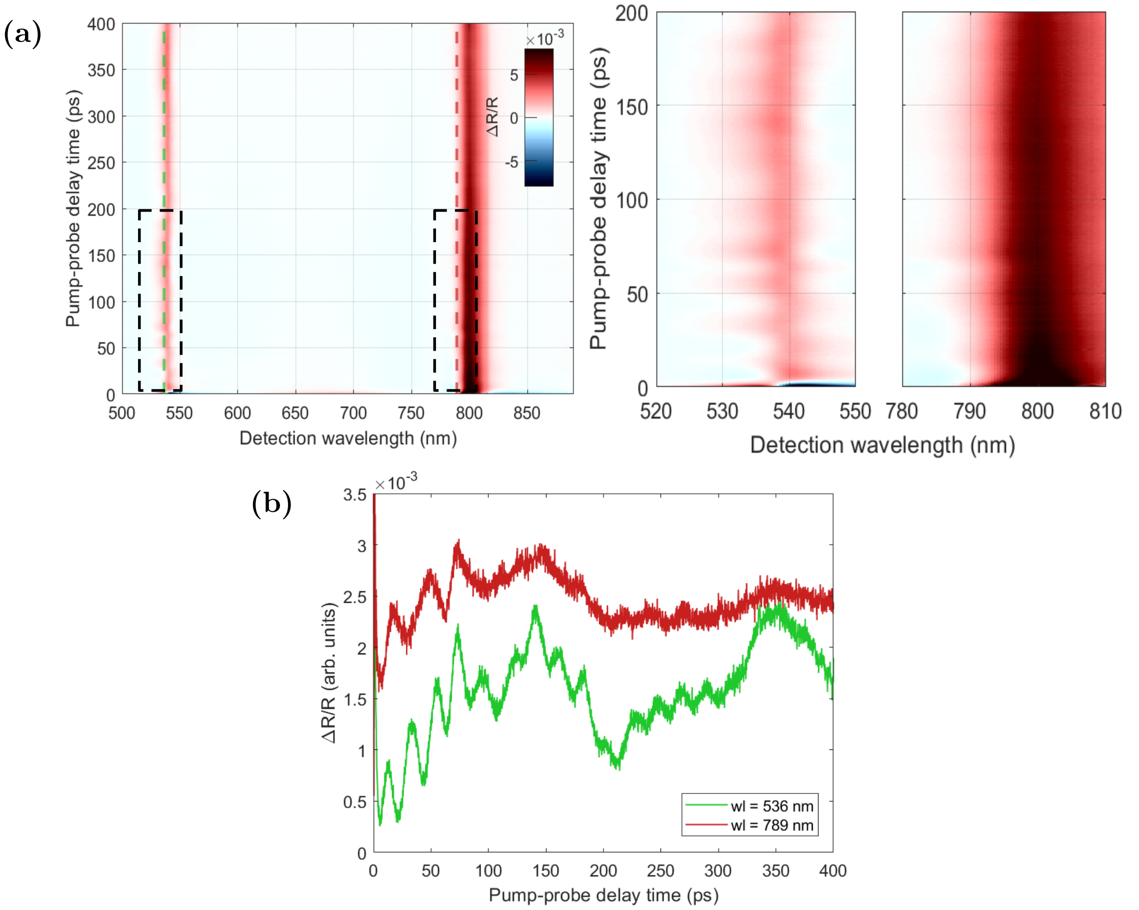

Figure 5.8: *Time-resolved differential reflectance ($\Delta R/R$) of the MIM cavity for a time delay of 400 ps, pumping (s-pol.) the* ***second resonance*** *and broadband probing (p-pol). (a) 2D map of the differential reflectance as function of wavelength and time delay, on the left. On the right, two zoom insets of the black dashed regions centered around the two resonances for delay up to 200 ps. (b) Transversal cuts at 528 nm, in green, and 784 nm, in red, extracted from the full 400 ps delay time. For visualization purposes, one plot is displayed with an offset above the other.*

In order to present a complete analysis, it was intended to perform pump-probe measurements exciting as well the second resonance using both pump and probe beams with p-polarization. This configuration would have allowed for a more complete assessment of the resonances' polarization dependence. However, due to time constraints, this remains to be completed. Additionally, fluence-dependent measurements are planned to determine the MIM cavity saturation threshold for resonance excitation. Finally and to conclude, additional pump-probe measurements could be added pumping this time off-resonant wavelength to verify that the reflectance signal enhancement is indeed resonance dependent.

5.2.2 Fourier analysis

In the previous Subsection 5.2.1 we mainly discussed the initial fast dynamics taking place in the MIM cavity. We have observed that resonant excitation of the cavity induced a transient shift and/or bleaching of both ENZ absorption peaks, due to localized heating in the cavity region. Contrarily to previous works[67], here we also investigate the subsequent dynamics. In Chapter 3 we investigated the slow acoustic dynamics induced by off-resonant excitation of nickel-based nanoresonators. With the help of finite-elements simulations, we showed that localized heating in the topmost layers of nickel resulted in the generation of an acoustic wave propagating in the cavity. As already mentioned when discussing Figures 5.4 5.6 and 5.8, we observe a similar effect when performing long delay scan on the MIM structure. The acoustic dynamics in nickel featured several eigenmodes propagating simultaneously and resulted in the complex pump-probe traces of Figure 4.8. On the other hand, the acoustic dynamics in the MIM cavity seems to be initially dominated by a specific eigenmode. Only after the first 100 ps, when this high-frequency mode is sufficiently attenuated, we can observe the effect of slower and weaker modes on the transient reflectivity trace. To quantitatively analyze the coherent acoustic dynamics in the MIM cavity, we performed a Fourier transform analysis of the time-domain reflectivity signal of the first presented case scenario, in which the first resonance was excited using an s-polarized beam (see Figure 5.4). Here, we analyze the acoustics corresponding to a wavelength cut at 528 nm over a 400 ps delay window. This corresponds to the case where the first resonance is selected for both pumping and probing. By performing a Fourier analysis on the acoustic response we can extract the dominant frequency components of the different oscillations observed in the pump-probe reflection trace. To guide our discussion, the sketch presented in Figure 5.9 illustrates the generation and dynamics of the acoustic response within the MIM cavity structure. Upon pump resonant excitation and subsequent carrier thermalization into a hot-electron population, an acoustic wave is generated at the top Ag layer. This acoustic wave propagates until the Ag/Al_2O_3 interface, where is partly reflected and partly transmitted. The acoustic wave that remains confined within the top Ag layer (blue acoustic pulse in sketch 5.9) is responsible to the high frequency oscillations we observed in the pump-probe trace for the first 100 ps. Repeating the same argument, the reflected light from each interface, represented in different colors, is tracked by the probe at the surface. The multiple reflections from each interface (blue for the

Ag/Al_2O_3, green for Al_2O_3/Ag and magenta for the Ag/Sample interface) ultimately shape the overall acoustic response of the MIM cavity.

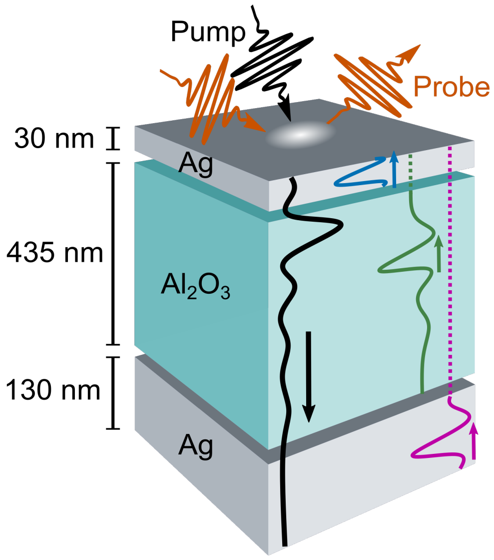

Figure 5.9: *Schematic representation of the ultrafast pump-probe reflectance measurement on the MIM cavity focusing on the acoustic response generation. Upon pump excitation, an acoustic wave is generated that propagates along the whole structure, represented in black. This acoustic wave travels throughout the structure and is reflected at each material interface undergoing partial transmission. Sketched in different colors, blue, green and pink, depending at which interface is reflected. The back reflected light is detected by the probe at Ag/air interface. The thickness of each Ag and* Al_2O_3 *layers are indicated of the left.*

In Figure 5.10 we present a Fourier-space analysis of the acoustic response of the MIM cavity under under resonant pumping and probing around the first ENZ resonance. The resulting FFT frequency spectrum of the overall acoustic signal, both presented in Figure 5.10, shows the presence of different GHz-range acoustic modes which can be associated with standing longitudinal acoustic waves. In panel (a), the experimental time-resolved differential reflectance is plotted (black curve), revealing pronounced oscillations which arise from the pump-induced heating of the top silver layer. To isolate each acoustic contribution, three time windows were selected based on the different time-scale of the observed acoustic oscillations. The first ranging from 0 to 100 ps, in blue, the second from 0 to 200 ps, in green, and the third from 0 to 400 ps, in magenta. To resolve the spectral content of these acoustic oscillations and identify the contributing modes, a Fourier transform analysis was applied to the time-domain signal of the entire experimental data after smoothing, represented in panel (b). Also, we performed a short-time Fourier analysis of each time window selected in panel (a) and plotted in panel (c). By segmenting the response over increasing delay windows, we isolate and track the temporal evolution of different frequency components. This approach enables the identification of acoustic modes associated with specific layer thicknesses and interface reflections, and highlights the role of material damping and interference over extended timescales.

The analysis reveals how different modes dominate the acoustic response of the MIM structure over different timescales. To better isolate the individual modes considered here, for each time window we smooth the experimental data to eliminate spurious spectral components. The top row of panel 5.10 (c) shows the frequency analysis of the first 100 ps, where we can observe a clear oscillation with a period of roughly 20 ps. This acoustic component is responsible for the peak arising around 50 GHz. In the FFT spectrum of this first window we also observe spurious features around 10 GHz, which we attribute to the finite size of the sampling window considered here. Considering that the speed of sound for longitudinal waves in silver is roughly 3 ps/nm [86], we expect that an acoustic mode trapped within the topmost 30 nm layer of Ag in the MIM structure should result in frequency oscillations around 60 GHz. This value is in reasonable agreement with the observed mode at 50 GHz, especially considering experimental uncertainties in the exact thickness of the top Ag layer. In the second row we consider the intermediate dynamics, consisting of time delays up to 200 ps (green curve). To filter out the effect of the fastest oscillations analyzed in the top panel, we smooth the experimental data until the high-frequency oscillations are no longer visible. The smoothed data shows a signal oscillating with a period of roughly 100 ps. The FFT of the smoothed signal indeed shows a peak around 10 GHz. To understand the origin of this acoustic component we can try to estimate what would be the frequency associated to a mode trapped within the first two layers of the MIM structure (green pulse in Figure 5.9). Considering that the nominal thickness of the Al_2O_3 layer in our sample is 435 nm and assuming for the longitudinal speed of acoustic waves a value of 10.5 nm/ps [87], we can expect that a roundtrip within the top Silver and insulating layers of the structure should take 99 ps for a longitudinal wave. This value is in remarkable agreement with the 10 GHz peak we observed. Finally, in the bottom panel we isolate the slowest acoustic dynamics (violet curve), which shows a main peak around 5 GHz. Repeating the argument above, we can estimate that a longitudinal wave excited at the top Silver layer across the whole MIM structure (magenta pulse in figure 5.9) should take around 170 ps. This would correspond to a slow acoustic response at 6 GHz, in very good agreement with our observations.

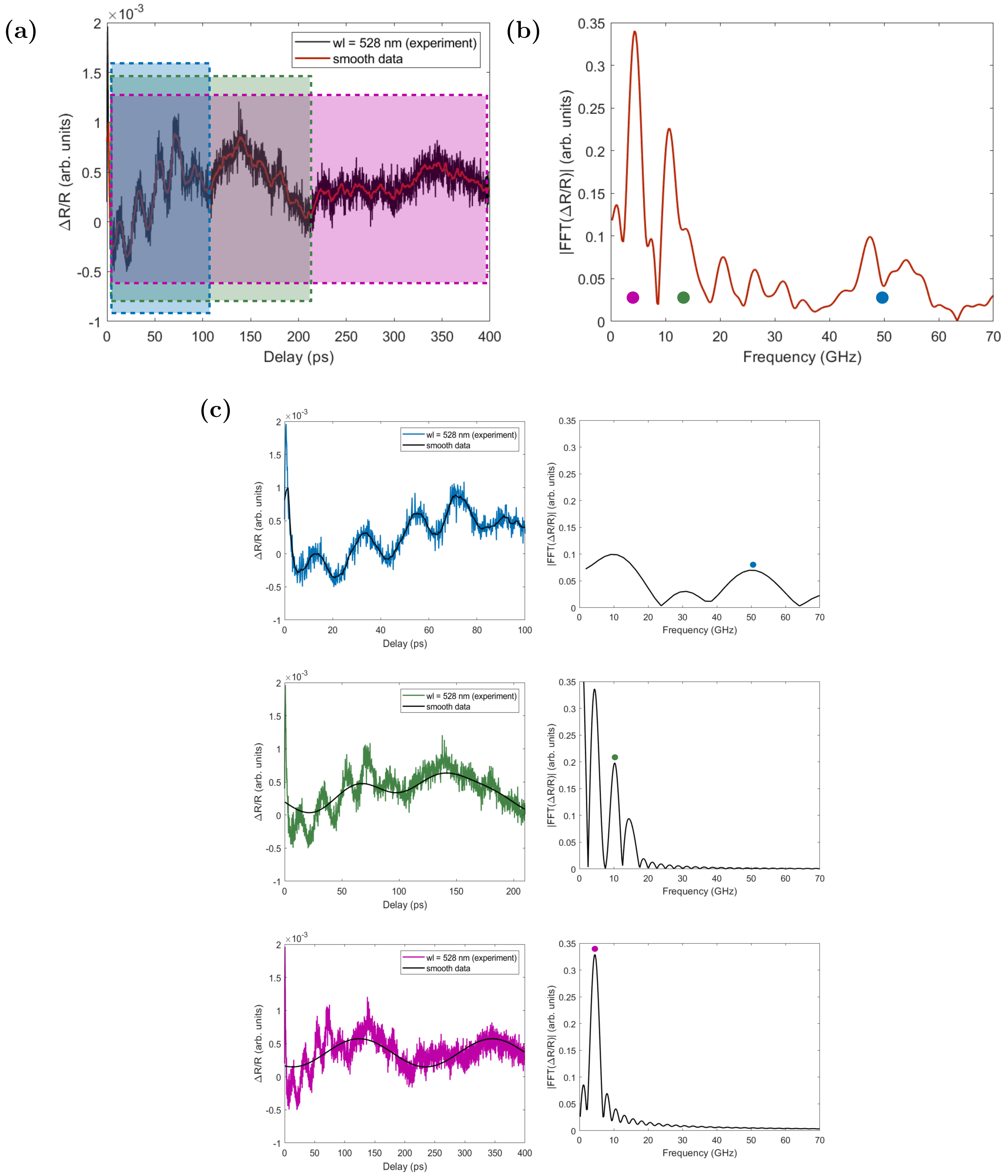

Figure 5.10: *(a) Time resolved reflectance signal at 528 nm over 400 ps time delay. The raw experimental data in shown in black, while a smoothed trace used for the Fourier analysis is shown in red. The acoustic response in segmented into three temporal windows, 0-100 ps (blue), 0–200 ps (green) and 0–400 ps (magenta), to isolate and analyze the different acoustic contributions over time. (b) FFT of the smoothed $\Delta R/R$ signal, revealing multiple frequency components. Colored markers indicate the dominant frequencies corresponding to each segmented time window in (a) and (c). (c) Left panels: acoustic signal segments corresponding to the time windows defined in (a). Right panels: FFT amplitude spectra for each segment, showing how specific acoustic modes evolve over time.*

5.3 Conclusions

In this work, we have presented a comprehensive study of ultrafast pump-probe reflectance measurements on a metal-insulator-metal (MIM) cavity, exploring its optical and acoustic responses across a range of experimental configurations. By tuning the pump wavelength to selectively excite resonances and performing polarization-dependent measurements, we demonstrated the cavity's resonant and polarization sensitive behavior. A summary of the observed dynamics corresponding to each configuration is presented in the following table.

The long delay time measurements, up to 400 ps, enabled us to capture the full temporal evolution of coherent acoustic phonons generated upon pump optical excitation. Fourier analysis of the time-domain data revealed a rich spectrum of acoustic frequencies, corresponding to multiple reflections and mode interferences within the layered cavity structure. These results not only confirm the generation and propagation of high-frequency acoustic modes but also provide insight into the interplay between optical resonances and lattice dynamics.

To support these measurements, complementary characterization techniques such as angle-resolved ellipsometry were suggested to support these measurements in the future, providing insight into the complex refractive index and dispersion characteristics of the multilayered system.

As a future perspective and in relation to the results presented in Chapter 4, the MIM acoustic response findings could be coupled with ferromagnetic resonances in thin nickel films creating a hybrid opto-acoustic cavity. By integrating a Ni layer onto the cavity, where strong acoustic strain fields are present, and tuning its ferromagnetic resonance frequency via an external magnetic field, it would be possible to explore magneto-acoustic coupling phenomena. This could pave the way for the development of hybrid photonic-magnetoacoustic devices capable of controlling spin dynamics with ultrafast acoustic pulses. Such integration represents a promising perfective for future studies in ultrafast magneto-optics and spintronics applications.

6

Sequencing amino-acids for protein identification

In parallel to the opto-acoustic studies presented in Chapters 4 and 5 additional optical characterization work was carried out as part of a multidisciplinary research project focused on the development of a next-generation protein sequencing [88] platform based on ultrafast Raman spectroscopy. This work is part of an European Union funding programme, *HORIZON 2020*, which brings together different universities, academic institutions and companies across multiple fields. The overall goal of this project, named *proID*, is the readout of amino-acid sequences along a protein chain using a combination of ultrafast Ramam spectroscopy [89], nano-optics [90], [91] and advanced data analysis [92].

To achieve this, the project integrates several disciplines: ultrafast optical excitation of single amnino-acids as they translocate through a plasmonic nanopore [93]; time-resolved Raman spectroscopy in combination with high sensitive devices, in particular SPAD (Single Photon Avalanche Diode) arrays [94]; both classical and quantum computational modeling [95] to investigate the nanopore-protein interaction. Finally, to discriminate amino-acid sequences from the collected Raman spectra: bioinformatic approaches relaying on machine learning [96].

These tasks were led by specific experts in the fields. Within this collaborative framework, my contribution was centered on the optical characterization of a custom-designed diffractive component aimed at reducing spectral complexity and enhancing detection speed. The optical element, referred to as Segmented Refractive Optical Element (SROE) [97], was developed to overcome the limitations of conventional Raman spectroscopy, which typically relies on high-resolution diffraction gratings capable of resolving thousands of spectral points but at the cost of slow acquisition times. In contrast, the SROE was engineered to isolate only the most relevant Raman bands required for amino-acid discrimination therefore, improving the optical readout process.

The idea is the following, supposing we want to read a sequence of only two amino-acods (AAs), we chose two Raman spectral bands for each aminoacid based on their vibrational fingerprints. The light scattered out of the nanopre is first spectrally dispersed by a prism and then, with a patterned chromium mask on top of the SROE, filtered to select each specific spectral band associated with each amino acid. These selected bands are then routed to target SPAD pixels by a chirped phase pattern on the back surface of the optical element.

In the following Section 6.1, we present detailed information regarding the design and fabrication of the SROE (Subsection 6.1.1), with particular emphasis on its optical characterization and performance validation (Subsection 6.1.2), to which I contributed most directly.

6.1 Diffractive micro optical component for Raman detection

One of the milestones of *ProID* is protein identification by reading a sequence of a limited number of AAs (2-4): this achievement is fundamental to prove the concept of Raman sequencing and to contribute to mitigate risks. Such identification requires a limited number of Raman peaks to be observed. For instance, to identify 4 different AAs one may need at least 4 specific Raman peaks (1 per AA). Likely, one may need even more, preferably 2 or more peaks per AA. To record only a limited number of Raman peaks, it is not necessary to employ a camera capable of recording hundreds of spectral points. This is a crucial consideration, as a camera that combines high spectral resolution ($\sim$100 points) with extreme temporal resolution ($\sim$100 ns) does not yet exist. To address this limitation, *ProID* conceived an approach based on monitoring a limited number of spectral points (or, equivalently, Raman peaks) [98].

In general terms, this approach relies on refractive optical elements, which are optical components that shape or manipulate light through refraction. A conventional refractive element, such as a lens or prism, bends light by varying its optical path length according to the geometry and refractive index of the material, thereby controlling the propagation, focusing, or intensity distribution of a beam. Building on this concept, segmented refractive optical elements (SROEs) are composed of multiple discrete refractive segments. Each segment contributes to a local refractive effect, and the segments together approximate complex wavefront transformations or generate a tailored intensity/phase profile. The segments may be flat, curved, or otherwise locally shaped, with different orientations or thicknesses, allowing precise control over the transmitted light while simplifying fabrication compared to a single continuous freeform surface.

In what follows, we present the design, fabrication, and optical characterization of the final SROE prototype, which will be employed for Raman detection in the *ProID* approach.

6.1.1 Segmented Refractive Optical Element (SROE): design and fabrication

The final version of this optical element was carried out by Bikash Kumar Bhandari at the *European Bioinformatics Institute (EBI)* who was in charge of the design, in collaboration with Jannis Weinacker at the *Karlsruhe Institute of Technology (KIT)* whose contribution focused on the fabrication [97]. Over the course of the three-year project, the SROE evolved through multiple designs to face emerging challenges and incorporate new ideas. Here, we present the most recent and optimized SROE version, which was adapted to meet the final requirements to achieve amino acid sequence reading.

The final SROE design consists of four independent focusing regions and has a total dimension of 3500 μm x 420 μm, printed on a 2 inch wafer. These four spectral regions were optimized to maximize the information required to identify the amino acid under investigation. After quantifying the information received for different configurations of four spectral regions, two SROE variants were fabricated, optimized for an average of 50 and 100 detected photons emitted by Serine [99]. Both designs cover wavenumbers ranging from 497 cm^{-1} to 1628 cm^{-1}, being the main difference on the spectral region covered by each focusing area. The light in between the selected spectral regions will be refracted along the y-axis, avoiding detection and reducing spectral cross-talk. The SROE is designed with a working distance of 15 mm, ensuring proper focusing onto the entrance of an optical fiber, one per focusing region.

The technique used to fabricate the sample is a commercially available 3D laser nanoprinter by *Nanoscribe*$^{®}$, called *QuantumX* [100] using two-photon grayscale lithography [101] which is suitable for the fabrication of micro-optical components with optical-grade surface quality and high surface precision, on the order of 100 nm [102]. Even though this fabrication process already delivers high quality optical surfaces, further improvement can be achieved through an iterative precompensation routine. This process involves comparing the measured surface topography obtained using a confocal microscope with the original design to identify systematic deviations introduced during the 3D printing stage. Regions where the printed structure is consistently too high or too low can be identified, and the height difference between the designed and fabricated surfaces is used to generate a precompensated design. By incorporating these corrections iteratively, the printed structure approximates to the targeted design.

In this study, six different SROE variants were fabricated and analyzed. Two sets were tested: one optimized for an average of 100 detected photons, and another for 50 photons, the latter being the most likely candidate for implementation in the final experimental setup. Each set includes three levels of precompensation: no precompensation, one iteration, and two iterations of precompensation. Figure 6.1 presents the surface height maps of each variant along with the corresponding histograms of the topographical error. A clear narrowing of the histogram peaks is observed as the number of precompensation steps increases, indicating a progressive improvement in surface fidelity and reproducibility of the optical design.

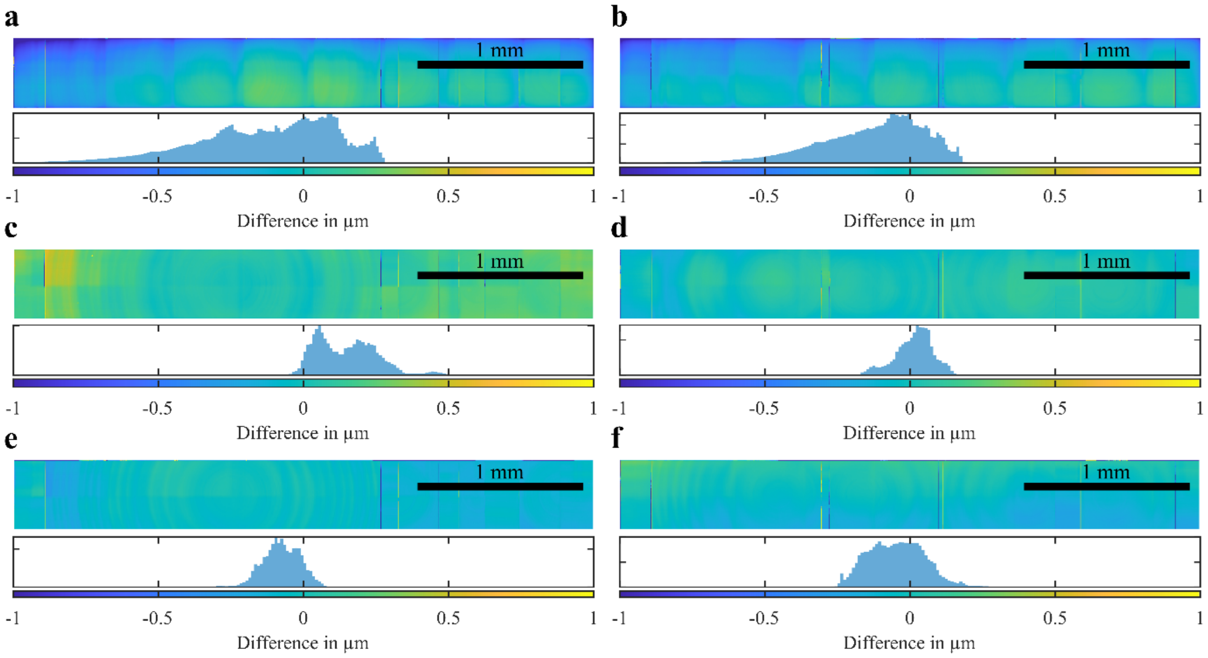

Figure 6.1: *Difference maps showing the deviation between the printed SROE topographies and the original design, along with their corresponding height histograms. The left column corresponds to SROEs optimized for 100 detected photons, while the right column corresponds to those optimized for 50 photon. In panels (a) and (b) no precompensation was performed which leads to larger difference values and a broader histograms. Ppanels (c) and (d) correspond to one step of precompensation, while panels (e) and (f) show two steps of precompensation. The histograms become narrower after already one step of precompensation. Figure taken from [103].*

6.1.2 Optical characterization

In this subsection, we describe the experimental setup used for the optical characterization of all the fabricated versions, above mentioned, of the SROE, including an analysis of the light spectrum for each spectral region. This characterization allows us to verify that each SROE effectively focuses the originally designed spectral regions onto the desired spots.

It is important to recall that in the final ultrafast Raman setup, the spectra of the amino acids will be spectrally dispersed by a diffraction grating. Therefore, the role of the SROE will be to guide and focus selected spectral components onto optical fibers connected to a detector. To simulate the final experimental conditions under which the SROE will operate, a custom-made setup was developed, a sketch is represented in Figure 6.2. The setup, described from right to left, begins with the generation of a white light supercontiniuum (WLG). The resulting spectrum ranges from 500 nm to 950 nm, closely matching the spectrum shown in Figure 3.11 (b). After the white light generation, the light beam is cleaned up and collimated using two lenses with a focal length of 50 mm. The beam is diffracted by a near-IR, 300 grooves/mm, optical grating, followed by a curved mirror with a focal length of 150 mm which focus the light onto the SROE's back plane. The SROE is placed at the focal plane of this mirror, ensuring that the incoming, spectrally dispersed, light hits the SROE perpendicularly.

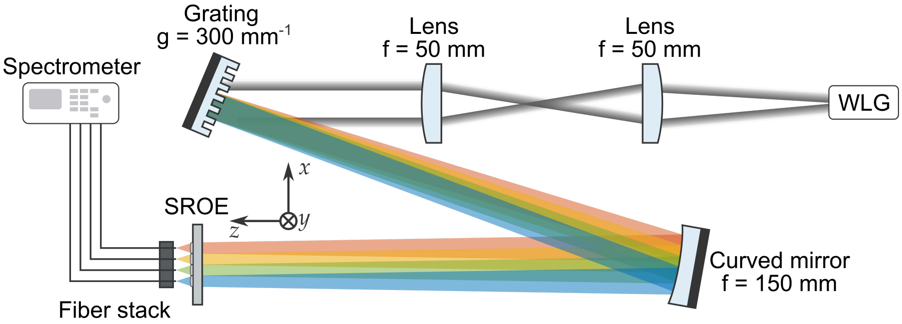

Figure 6.2: *Sketch of the custom-made setup used for the optical characterization. From right to left, the supercontiniuum white light (WLG) is collimated with two lenses of the same focal length, $f = 50$ mm, before hitting the diffractive grating (300 mm^{-1}). The spectrally separated light is then focused with a curved mirror, $f = 150$ mm, onto the SROE. The SROE focuses the spectral region onto four optical fibers connected to a spectrometer. Figure adapted from [104].*

To demonstrate that the SROE works as designed, it is necessary to verify that it covers the correct spectral regions and efficiently couples the light into each fiber channel. As first step, a commercial camera is placed in the image plane of the SROE to image the four foci spots generated by the SROE, each corresponding to a different spectral region. Figure 6.3 presents the collected foci from all the fabricated SROE variants. The images on the left side correspond to the design optimized for an average of 100 detected photons, while those on the right side correspond to the variant optimized for 50 photons, both based on the Raman response of Serine. For each fabrication, we tested different levels of precompensation, introduced during the design process. Panels (a) and (b) show results for uncompensated designs; panels (c) and (d) with one step of precompensation; and panels (e) and (f) with two steps of precompensation. All the intensity values have been normalized to the highest pixel intensity to facilitate the comparison.

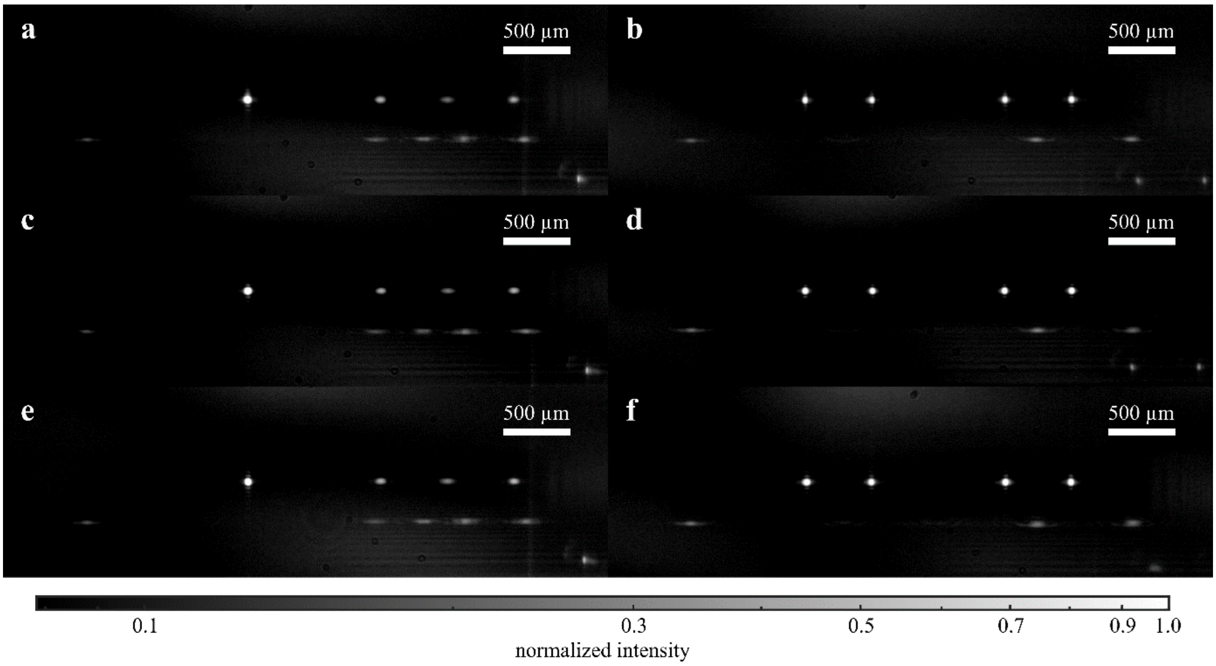

Figure 6.3: *Camera images of all the fabricated SROE versions, taken in the optical setup. Panels on the left column are the samples corresponding to 100 photons and on the right, 50 photons. Panels (a) and (b) show the results for the uncompensated samples. Panels (c) and (d) the samples with one step of precompensation and (e) and (f) two steps of precompensation. Figure taken from [103].*

No clear difference is observed in the performance of the SROE samples depending on the number of precompensation steps.

Following the analysis, the camera was replaced by a 16-fiber stack, although only four (one for each spectral region), were actively used. The core diameter of each fiber is 440 μm and a center to center spacing of 500 μm, for which the SROE was designed. Each focal spot from the SROE was coupled into a separate fiber in parallel. Notably, no realignment was necessary when switching between fibers.

The emerging light from each fiber was directly coupled and analyzed by a spectrometer to verify that the spectral content matched the designed windows. Figure 6.4 presents the measured spectra of the six different SROE versions, i.e. for 100 (left columns) and 50 (right columns) detected photons across the 3 different steps of precompensations (uncompensated, one-step, and two-step). In each plot, the background colored boxes indicate the designed spectral ranges that each detector is supposed to measure and, in the foreground in a darker shade, are the measured spectral profiles.

Overall, a good agreement is observed between the expected and measured spectra, both in terms of central wavelength and bandwidth. Some minor deviations are observed, such as the yellow spectral curve in Figure 3.11 (c), which appears to be wider than the targeted spectral interval. One possible explanation is the limited resolution of the imagining system, being not possible to focus such small spots.

From these measurments, we can conclude that all the fabricated SROEs work accordingly to the design configuration by focusing the designed spectral regions into the equidistant fibers. Indeed, there is no obvious improvement due to the precompensation, indicating that the design of the NIR-SROE is robust towards minor fabrication deviations.

6.2 Conclusions

In this chapter, we presented the optical characterization of a custom Segmented Refractive Optical Element (SROE), developed as part of a multidisciplinary project focused on ultrafast Raman for protein sequencing. The SROE is designed to route selected Raman spectral bands, associated with specific amino acids, onto individual detectors, optical fibers, enabling rapid and targeted spectral readout with minimal photon counts.

Our experimental validation included both camera imaging of the focused spots combined with spectral measurements. These tests confirmed that the fabricated SROEs reliably focus the intended spectral regions onto the correct spatial positions. The measured spectral responses match the design specifications across multiple device versions and photon count conditions. Moreover, no significant performance differences were observed across varying levels of precompensation, indicating robustness in what fabrication process regards.

This optical characterization confirms that the SROE design performs as intended and represents a crucial step toward integrating compact, efficient spectral filtering into the final detection system for protein sequencing.

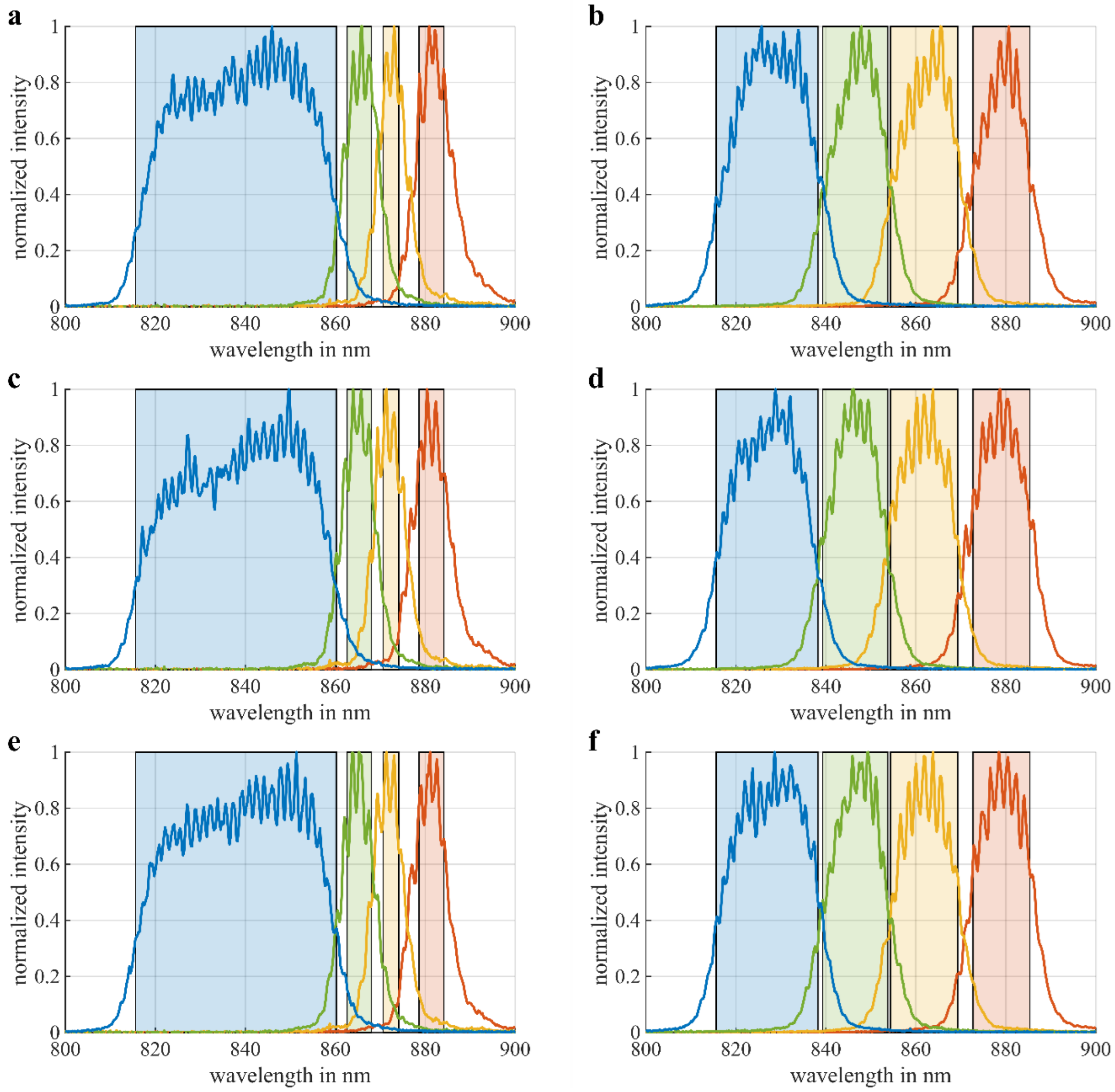

Figure 6.4: *Measured spectra of each lens obtained from the coupling with the fiber, overlaid the designed spectral windows represented with rectangular boxes. Plots on the left columns correspond to 100 photons and on the right to 50. First row shows the results without precompensation, the second one step of precompensation and the third two steps of precompensation. This figure is reproduced from [103], licensed under a Creative Commons Attribution (CC BY) license.*

7

Concluding remarks

This thesis has explored the interaction of ultrashort light pulses with nanoscale structured materials, focusing on the generation, detection, and control of coherent acoustic phonons in multifunctional platforms. Through a combination of experimental ultrafast spectroscopy, based on custom-built optical setups, and theoretical modeling, we have addressed how light can excite, manipulate, and reveal dynamics within matter on the femtosecond to nanosecond timescale.

We began with Chapter 2 with a conceptual overview of ultrafast opto-acoustics and its relevance in condensed matter physics and nanotechnology. By reviewing the principles of coherent acoustic phonon generation, based on the Two-Temperature Model and the interplay between electronic and lattice subsystems, we established a foundation for understanding how stress and strain pulses can be launched with femtosecond lasers. This chapter introduced how nanostructuring, such as suspended geometries or layered heterostructures, modifies the opto-acoustic response and opens new pathways for coupling acoustic waves to magnetic, electronic, or photonic degrees of freedom.

In Chapter 3 we described the ultrafast tools and nonlinear processes that support the experimental techniques used in this thesis. This included a detailed discussion of pump-probe spectroscopy and the custom setup designed and implemented for our measurements. Second- and third-order nonlinear phenomena, specifically second harmonic generation (SHG), third harmonic generation (THG), and white light Generation (WLG), were introduced as tools for pulse conversion and spectral extension. Additionally, the design and function of two home-built optical parametric amplifiers (OPAs), covering the visible and visible-near-infrared regions, were presented.

Chapter 4 presented the central experimental findings of the thesis: the fabrication and characterization of freestanding nickel cavities via picosecond laser delamination. These cavities, compared to reference nickel films, exhibited markedly lower acoustic damping, higher quality factors, and longer-lived resonances. Time-resolved pump-probe spectroscopy, Fourier analysis, and numerical multiphysics simulations demonstrated the existence of confined longitudinal acoustic modes. An appendix further developed a Lorentzian fitting analysis to extract damping trends, showing potential Rayleigh-type loss mechanisms. The findings position nickel cavities as promising platforms for resonant acoustic and magneto-acoustic applications.

In Chapter 5, we shifted focus to metal–insulator–metal (MIM) cavities supporting epsilon-near-zero (ENZ) photonic modes. Pump-probe measurements revealed rapid acoustic modulations associated with field compression and confined phonon resonances. These structures, while optically different from nickel cavities, exhibit similarly rich opto-acoustic dynamics. Their response is highly sensitive to dielectric layer thickness and field distribution, making them promising for ultrafast modulation and sensing, exploiting the high light-matter coupling ensured by the ENZ modes.

As part of a broader collaborative effort, in Chapter 6 we described the design and optical characterization of a Segmented Refractive Optical Element (SROE), intended for ultrafast Raman spectroscopy of amino acids. Using a white-light beam and emulating the final system geometry, we demonstrated spectral filtering and potentially pixel-selective detection of Raman bands. This project highlights the role of custom micro-optics in data-driven spectroscopy, showing the potential for fast, selective, protein identification systems.

The work presented here illustrates how nanostructured geometries not only enhance opto-acoustic responses but also enable multiphysics coupling mechanisms involving strain, heat, magnetism, and photonics. Looking forward, several promising research directions arise:

- **Magneto-acoustics:** The high-Q acoustic modes in freestanding nickel cavities provide a promising basis for strain-assisted control of ferromagnetic dynamics, potentially enabling GHz spintronic applications.

- **Hybrid photonic platforms:** The integration of ENZ photonic cavities with magnetic or opto-mechanical material platforms may yield reconfigurable nanodevices responsive to light, strain, and electromagnetic fields.

- **Bio-integrated optics:** The segmented optical elements developed here can be adapted for broader biosensing contexts, where fast spectral selection and real-time readout are critical.

- **Advanced nanofabrication:** Techniques such as ps-laser delamination and multi-photon printing are effective for producing microscale cavities and should be further explored for scalable, maskless device fabrication.

This thesis thus contributes to the foundational understanding of light–matter interactions in nanoscale platforms and proposes novel tools and approaches for future studies in opto-acoustics, nonlinear optics, and hybrid multi-physics systems.

A

Supplementary data: Acoustic modes in nickel cavities

In this appendix, we present a complementary analysis of the propagating acoustic response in the nickel cavity and film structures. This study was primarily conducted by Andrea Rossetti and is based on the experimental pump-probe data discussed in Chapter 4. Starting from the baseline-corrected transient reflectivity data (see Figure 4.8, panel (b)), we propose a different fitting approach to quantitatively compare the opto-acoustic performance of the freestanding cavity versus the supported film. Following the methodology introduced by Ghita et al. [60], the differential reflectance curves are decomposed into a superposition of damped harmonic oscillators, each corresponding to an acoustic eigenmode of the system. Specifically, the time-resolved differential reflectance signal is fitted with the expression:

$$\frac{\Delta R(t)}{R} = \sum_{n=1}^{N} A_n e^{-\gamma_n t} \cos(\omega_n t + \phi_n) \tag{A.1}$$

where A_n, ω_n and ϕ_n are the amplitude, decay rate, angular frequency, and phase of the n^{th} acoustic mode, respectively, and N is the number of modes considered (five for the cavity and seven for the film). The corresponding fits are overlaid on the experimental data in Figure A.1 panels (a) and (b), showing good agreement in the time domain.

Given the high number of free fit parameters, a reliable initial guess for the fit is needed. We achieve this by first fitting the Fourier Transform (FFT) of the experimental data with a sum of Lorentzian functions. The good agreement between experimental data-points and fit curves in both the time-domain and frequency-domain supports the validity of the harmonic oscillator model for describing the acoustic response (see Figure A.1, panels (c), (d)).

Figure A.2, panel (a), shows the extracted decay rates γ_n as a function of the acoustic

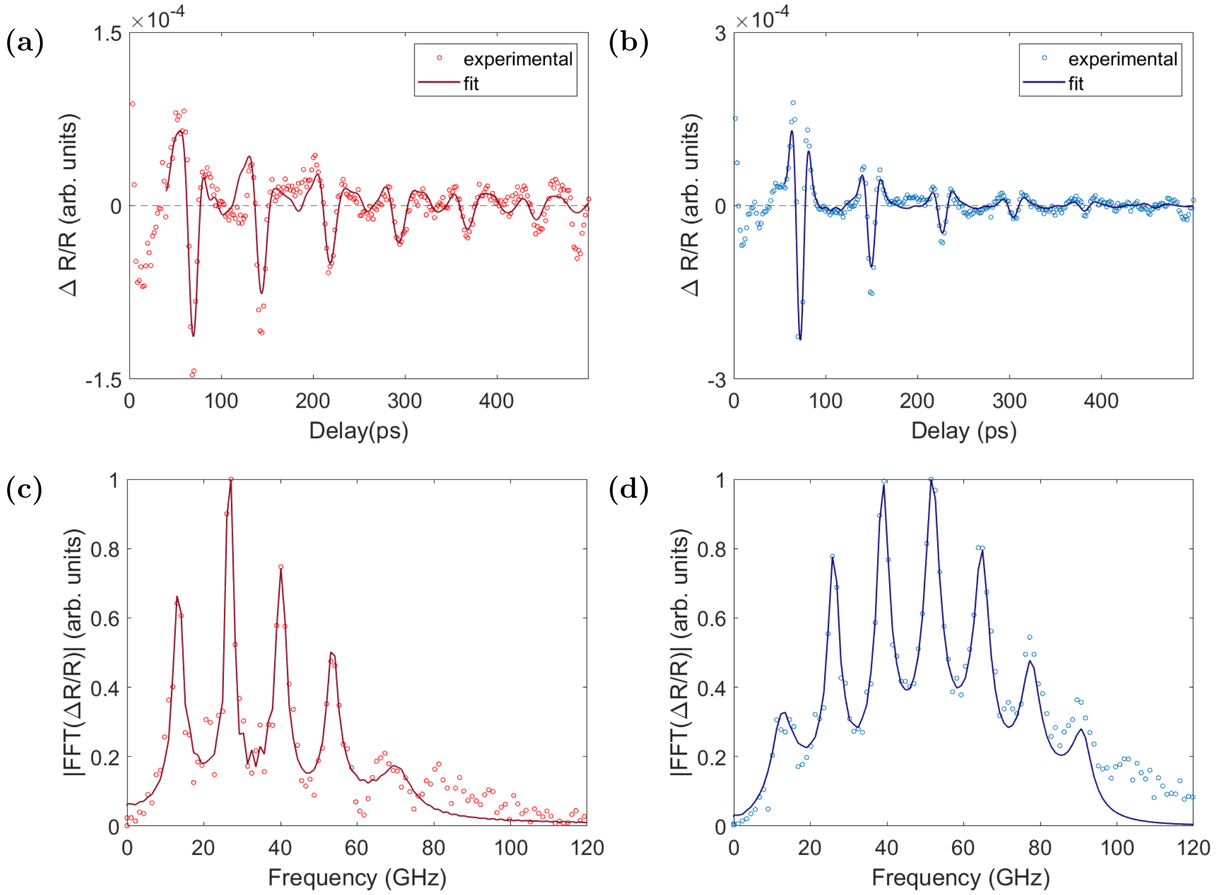

Figure A.1: *(a) Isolated experimental acoustic response for cavity (dots) after the baseline is subtracted. The solid lines show the best fit curve for the pump-probe trace, obtained using as model a superposition of damped harmonic oscillators. (b) same as panel (a), for the film. (c) Fast Fourier transform (FFT) of the experimental (dots) and fitted (solid line) pump-probe traces for the cavity (c) and film (d).*

frequency $f_n = \omega_n/2\pi$, along with error bars from the fitting procedure. As suggested by Ghita et al. [60], a quadratic dependence ($\gamma \propto \omega^2$) typically indicates phonon-phonon scattering as the dominant damping mechanism, which is indeed observed for the film configuration. In contrast, for the cavity configuration, the decay rates are better described by a power law of the form $\gamma = a + b\omega^c$, yielding an exponent $c \approx 4$. This faster-than-quadratic scaling suggests that damping in the cavity is likely dominated by Rayleigh-scattering, which follows a $\gamma \propto \omega^4$ dependence [105], [106]. Figure A.2, panel (b), shows the quality factor $Q_n = \omega_n/(2\gamma_n)$ extracted for each acoustic eigenmode. Notably, the cavity exhibits systematically higher quality factors than the film. Most cavity modes display $Q_n > 15$, underscoring the enhanced acoustic performance enabled by the freestanding geometry. Neglecting the fundamental mode, which is likely affected by grain boundaries and surface roughness effects. The quality factors estimated for the cavity surpass the typical quality factor $Q_G \approx 12$ reported for magnon resonances in nickel [60].

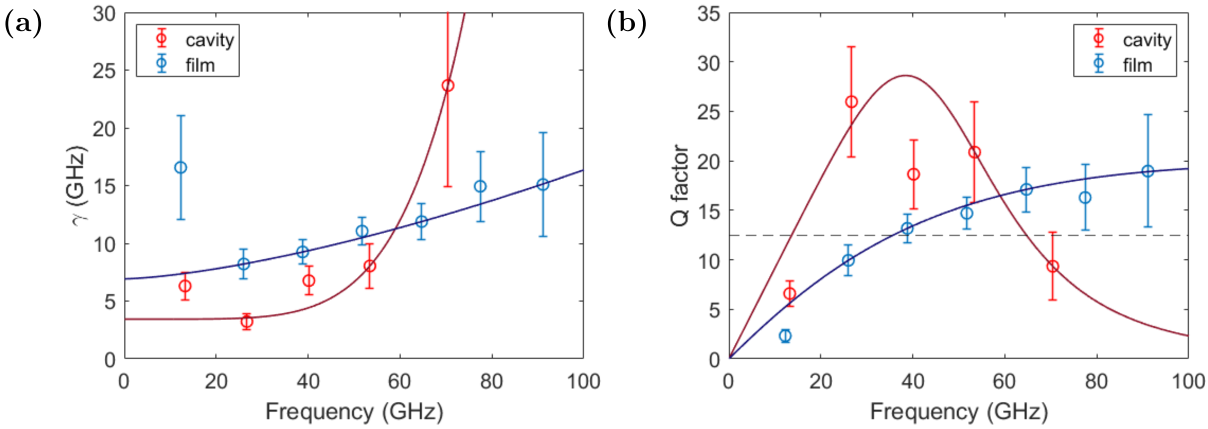

Figure A.2: *(a) Damping as a function of frequency obtained from the fit of the pump-probe data for the film (blue circles) and cavity (red circles). A power law fit* $y = a + bx^c$ *is shown as a solid line as guide to the eye for both cases. (b) Q-factor associated to different eigenmodes for cavity and film. The solid lines are obtained from the fits of panel (a) and shown as guide to the eye. The black dashed line indicates the magnon Q-factor in nickel* $Q_G \simeq 12$ *as discussed in [60].*

These findings position the suspended cavity as a promising opto-acoustic platform, particularly for multi-physics applications such as magneto-acoustic coupling. The enhanced Q-factors achieved via ps-laser delamination [59] represent an important advance toward dynamic control of magnetization through laser-driven strain, potentially enabling coherent coupling between longitudinal acoustic phonons and transverse magnetic modes [107].

B

Time domain analysis on different cavities

In this appendix a complementary analysis of the acoustic response of different cavities is presented, following the time-domain analysis introduced in Appendix A. As shown in Subsection 4.1.2, and in particular in Figure 4.2, each line contains structures fabricated under the same conditions. This raises relevant questions about fabrication reproducibility and, consequently, the opto-acoustic performance of the resulting cavities.

In Figure B.1, panel (a), the pump-probe transient reflectivity of an additional film spot (*"pristine film 1"*, also discussed throughout this thesis) is presented together with four new cavity structures located on the same line as *"delaminated cavity 1"*, the reference structure analyzed in Chapter 4, all measured under identical excitation conditions. While the curves measured on different spots of the pristine film are practically identical (see the two top rows), we observe a different response between delaminated cavities, plausibly due to variations in the corrugation profile of the bottom interface. In general, the delaminated cavities show a smaller attenuation of the acoustic pulse between successive roundtrips. In panel (b), the Fourier transform of the experimental transient reflectance is shown. Each series of peaks corresponds to the different eigenmodes contributing to the overall acoustic wave-packet propagating along the two different configurations.

Disentangling the dynamics of individual eigenmodes provides valuable insight into the experimental observations. To this end, we performed a short-time Fourier transform (STFT) of all measured pump-probe traces, with the resulting spectrograms shown in Figure B.2. For the film, panels (a) and (b), the fundamental eigenmode is only weakly excited and disappears after the first round trip, while the second eigenmode is also comparatively faint. In contrast, modes $n = 3, 4, 5$ dominate the response but still undergo strong attenuation, with amplitudes reduced

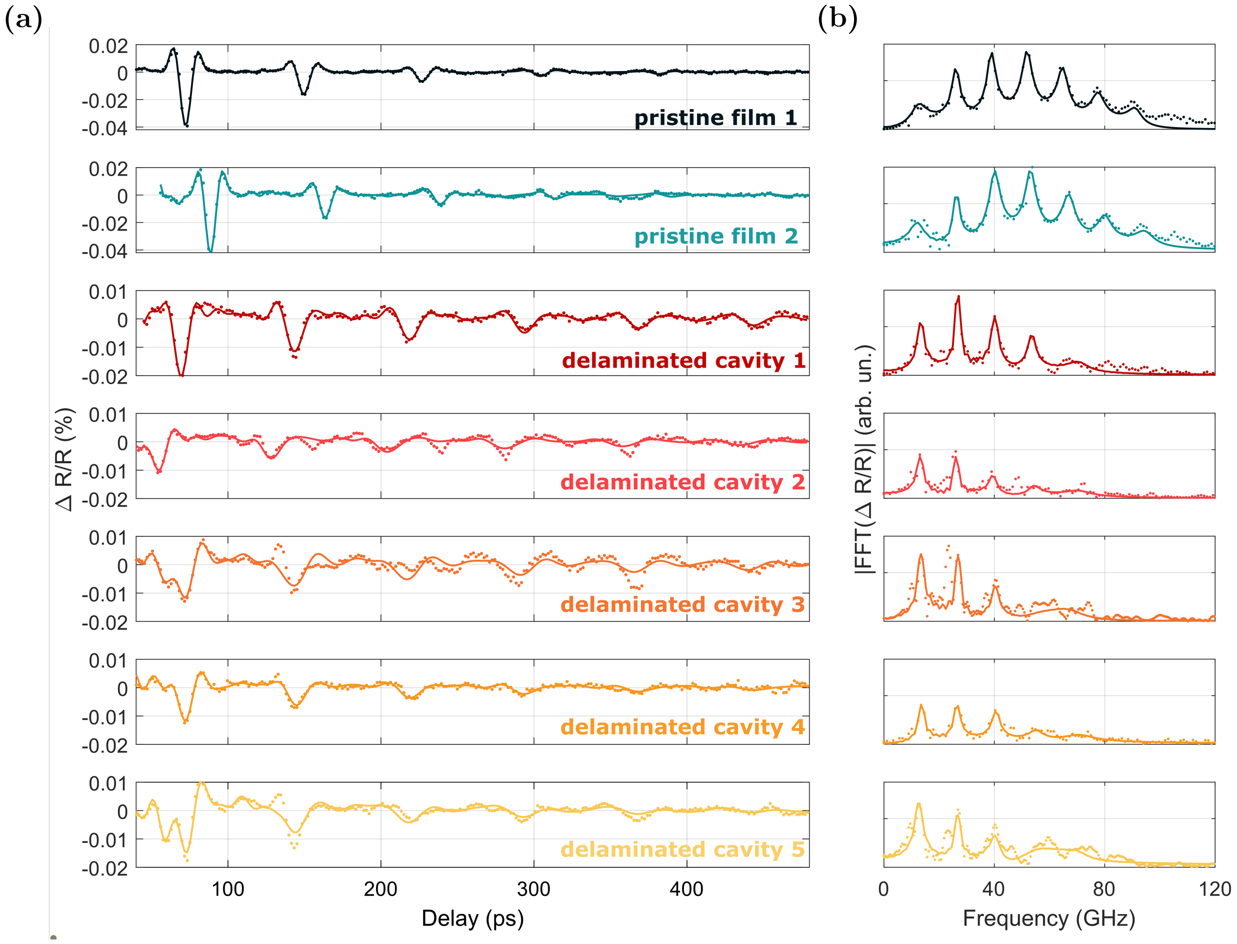

Figure B.1: *(a) Experimental transient reflectivity measurements (dots) and fit (solid line) for two spots on the pristine nickel film and five different delaminated cavities. (b) Fast-Fourier-transform of the curves in (a). This figure is reproduced from reference [73], licensed under a Creative Commons Attribution (CC BY) license.*

by more than 50% after each round trip. In the cavities (panels (c) to (g)) however, the first two eigenmodes are efficiently excited and exhibit considerably longer lifetimes than in the pristine film. Notably, in two cavities (3 and 4), the $n = 2$ mode at 26 GHz dominates the response and propagates nearly unperturbed over the investigated time window. Consistent with our previous discussion, the spectrograms also reveal that the acoustic wave packet in the delaminated cavities lacks high-frequency components above 60 GHz.

To conclude this analysis, Figure B.3, panel (a) summarizes the extracted decay rates γ_n as a function of the frequency f_n for the considered eigenmodes. For the film, the decay rates follow an approximately quadratic dependence, with a power-law fit yielding an exponent of $c \approx 1.5$. In contrast, the delaminated cavities exhibit a much steeper scaling, with $c \approx 4.6 \pm 0.8$. These results are in good agreement with the discussion presented in Subsection 4.2.2 and further

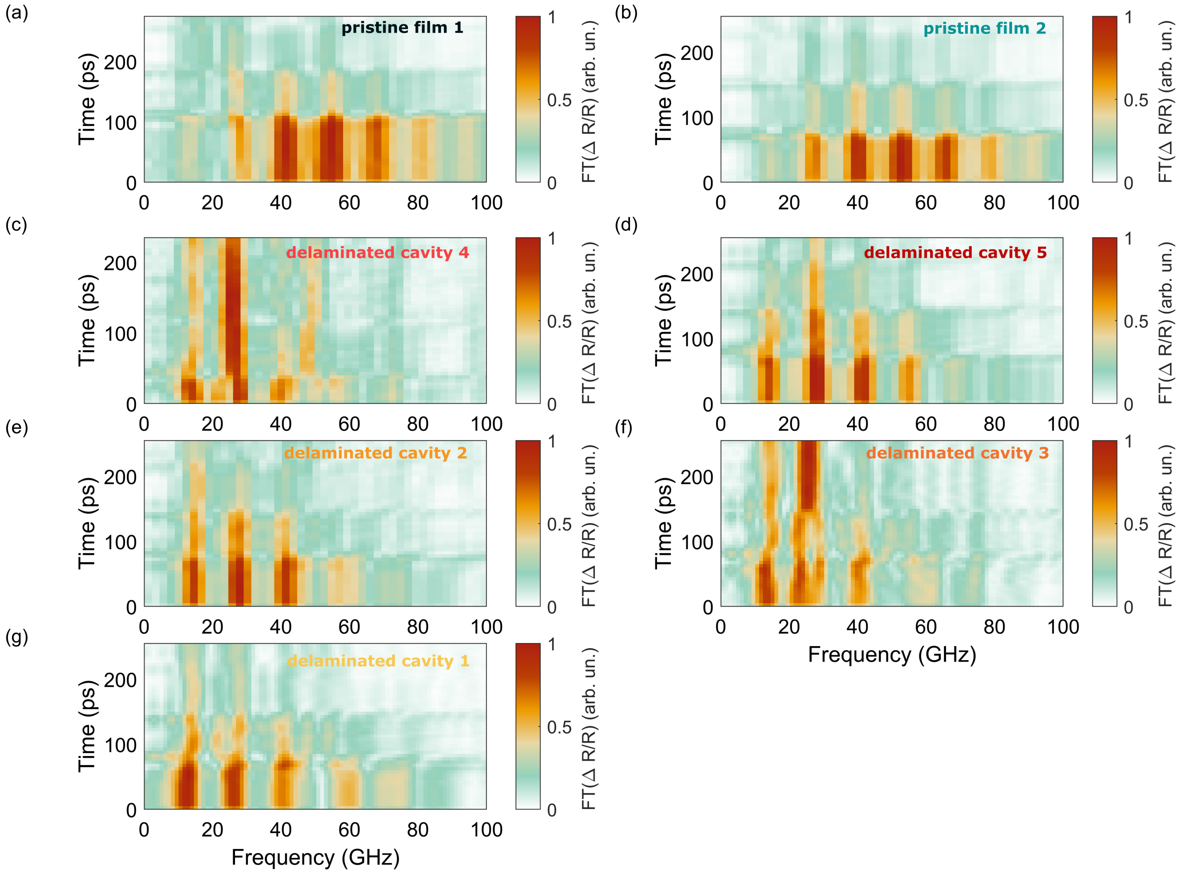

Figure B.2: Spectrograms of acoustic eigenmode propagation for the pristine film (a), (b) and for the delaminated cavities (c)–(g), obtained from the pump–probe traces in Figure B.1 using a short-time Fourier transform algorithm. This figure is reproduced from reference [73], licensed under a Creative Commons Attribution (CC BY) license.

complemented in Appendix A. Panel (b) shows the corresponding quality factors, $Q_n = \omega_n/(2\gamma_n)$, associated with the various eigenmodes. The dashed black line indicates the typical quality factor of magnon resonances in nickel, $Q_G \approx 12$ [69]. The necessary condition, $Q_n \geq Q_G$, for the efficient excitation of magnetization dynamics by acoustic pulses is fulfilled by the second and third eigenmodes in all cavities. This demonstrates that delaminated cavities can indeed sustain acoustic pulses suitable for controlling magnetization dynamics [107] up to 60 GHz, although a decrease in the quality factor is observed beyond this frequency.

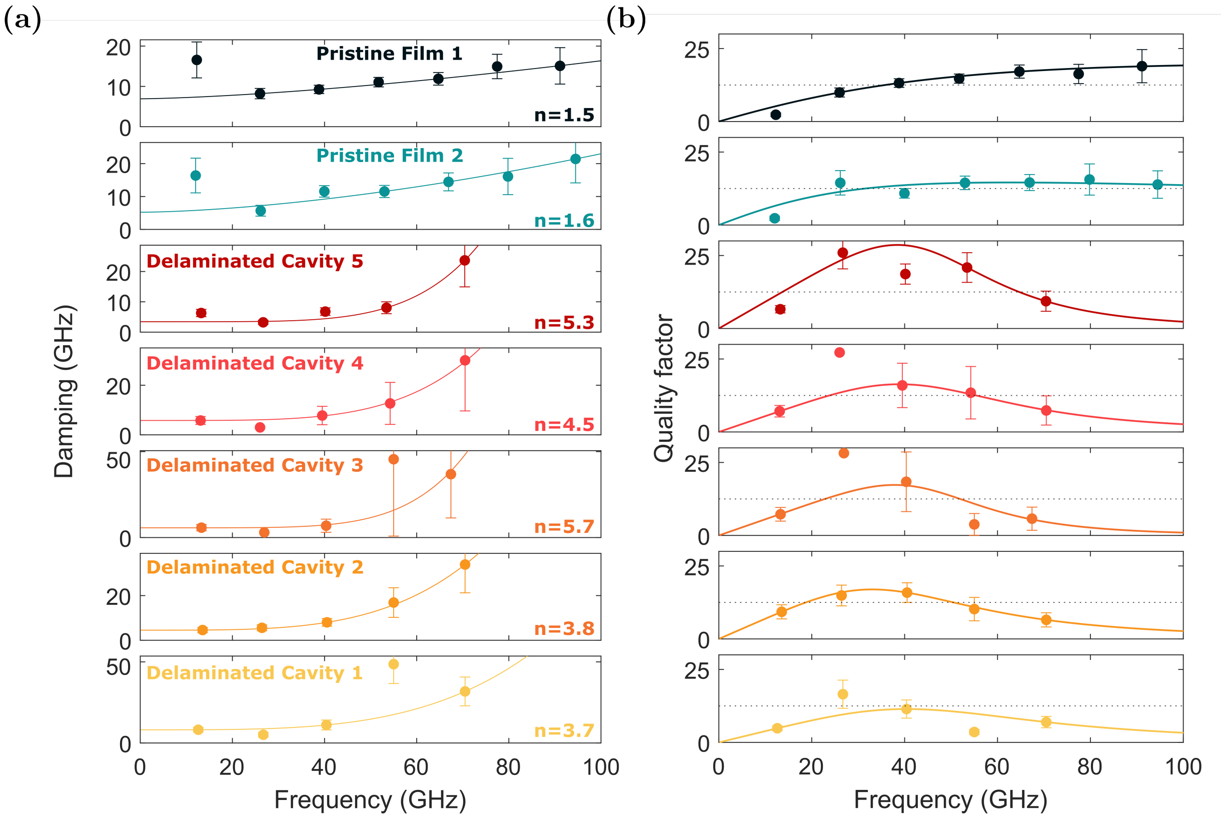

Figure B.3: *(a) Decay rates as a function of frequency extracted from the pump–probe data. Solid lines represent power-law fits ($y = a + bx^c$) and serve as a guide to the eye. (b) Quality factors associated with the different eigenmodes. Solid lines are derived from the fits in panel (a), while the black dashed line marks the typical Q-factor of magnon resonances in nickel, $Q_G \approx 12$ [69].This figure is reproduced from reference [73], licensed under a Creative Commons Attribution (CC BY) license.*

In conclusion, this analysis reinforces the discussion in Chapter 4, demonstrating that delaminated cavities represent a promising platform for ultrafast modulation of acoustic waves at frequencies below 60 GHz.

Bibliography

[1] Pablo Maldonado and Yaroslav O. Kvashnin. Microscopic theory of ultrafast out-of-equilibrium magnon-phonon dynamics in insulators. *Physical Review B*, 100(1):1–16, 2019.

[2] Chihiro Nagura, Akira Suda, Hiroyuki Kawano, Minoru Obara, and Katsumi Midorikawa. Generation and characterization of ultrafast white-light continuum in condensed media. *Applied Optics*, 41(18):3735, 2002.

[3] Bertrand Audoin. Principles and advances in ultrafast photoacoustics; applications to imaging cell mechanics and to probing cell nanostructure. *Photoacoustics*, 31:100496, 2023.

[4] Pascal Ruello and Vitalyi E. Gusev. Physical mechanisms of coherent acoustic phonons generation by ultrafast laser action. *Ultrasonics*, 56:21–35, 2015.

[5] V. S. Vlasov, A. V. Golov, L. N. Kotov, V. I. Shcheglov, A. M. Lomonosov, and V. V. Temnov. The Modern Problems of Ultrafast Magnetoacoustics (Review). *Acoustical Physics*, 68(1):18–47, 2022.

[6] C. Thomsen, J. Strait, Z. Vardeny, H. J. Maris, J. Tauc, and J. J. Hauser. Coherent phonon generation and detection by picosecond light pulses. *Physical Review Letters*, 53(10):989–992, 1984.

[7] T. Saito, O. Matsuda, and O. B. Wright. Picosecond acoustic phonon pulse generation in nickel and chromium. *Physical Review B - Condensed Matter and Materials Physics*, 67(20):1–7, 2003.

[8] P. Babilotte, P. Ruello, D. Mounier, T. Pezeril, G. Vaudel, M. Edely, J. M. Breteau, V. Gusev, and K. Blary. Femtosecond laser generation and detection of high-frequency acoustic phonons in GaAs semiconductors. *Physical Review B - Condensed Matter and Materials Physics*, 81(24):1–14, 2010.

[9] O. Matsuda, T. Tachizaki, T. Fukui, J. J. Baumberg, and O. B. Wright. Acoustic phonon generation and detection in GaAs/Al 0.3Ga 0.7As quantum wells with picosecond laser pulses. *Physical Review B - Condensed Matter and Materials Physics*, 71(11):1–13, 2005.

[10] R. W. Schoenlein, W. Z. Lin, J. G. Fujimoto, and G. L. Eesley. Femtosecond studies of nonequilibrium electronic processes in metals. *Physical Review Letters*, 58(16):1680–1683, 1987.

[11] B.L.; Perel'man T.L Anisimov, S.I.; Kapeliovich. Electron emission from metal surfaces exposed to ultrashort laser pulses. *Soviet Physics - Uspekhi*, 66:776–781, 1973.

[12] Pablo Maldonado, Karel Carva, Martina Flammer, and Peter M. Oppeneer. Theory of out-of-equilibrium ultrafast relaxation dynamics in metals. *Physical Review B*, 96(17):1–13, 2017.

[13] E. M. Landau, L. D. Lifshitz. Physical kinetics: Course of theoretical physics, Vol.10. Pergamon, 1981.

[14] Tudor Gabriel Mocioi, Antonia Ghita, and Vasily V. Temnov. Towards Resonantly Enhanced Acoustic Phonon-Exchange Magnon Interactions at THz Frequencies. *Magnetochemistry*, 9(7), 2023.

[15] Yuta Imade, Vitalyi E. Gusev, Osamu Matsuda, Motonobu Tomoda, Paul H. Otsuka, and Oliver B. Wright. Gigahertz Optomechanical Photon-Phonon Transduction between Nanostructure Lines. *Nano Letters*, 21(14):6261–6267, 2021.

[16] M. Perner, S. Gresillon, J. März, G. Von Plessen, J. Feldmann, J. Porstendorfer, K. J. Berg, and G. Berg. Observation of hot-electron pressure in the vibration dynamics of metal nanoparticles. *Physical Review Letters*, 85(4):792–795, 2000.

[17] J. F. Robillard, A. Devos, I. Roch-Jeune, and P. A. Mante. Collective acoustic modes in various two-dimensional crystals by ultrafast acoustics: Theory and experiment. *Physical Review B - Condensed Matter and Materials Physics*, 78(6):1–7, 2008.

[18] A. Amziane, L. Belliard, F. Decremps, and B. Perrin. Ultrafast acoustic resonance spectroscopy of gold nanostructures: Towards a generation of tunable transverse waves. *Physical Review B - Condensed Matter and Materials Physics*, 83(1):1–7, 2011.

[19] J. Janušonis, C. L. Chang, T. Jansma, A. Gatilova, V. S. Vlasov, A. M. Lomonosov, V. V. Temnov, and R. I. Tobey. Ultrafast magnetoelastic probing of surface acoustic transients. *Physical Review B*, 94(2):1–7, 2016.

[20] B. Koopmans, M. Van Kampen, J. T. Kohlhepp, and W. J.M. De Jonge. Ultrafast magneto-optics in nickel: magnetism or optics? *Physical Review Letters*, 85(4):844–847, 2000.

[21] E. Beaurepaire, J. C. Merle, A. Daunois, and J. Y. Bigot. Ultrafast spin dynamics in ferromagnetic nickel. *Physical Review Letters*, 76(22):4250–4253, 1996.

[22] De Lin Zhang, Jie Zhu, Tao Qu, Dustin M. Lattery, R. H. Victora, Xiaojia Wang, and Jian Ping Wang. High-frequency magnetoacoustic resonance through strain-spin coupling in perpendicular magnetic multilayers. *Science Advances*, 6(38), 2020.

[23] Tlek Tapani, Nils Henriksson, Thomas Deckert, Haifeng Lin, Agne Ciuciulkaite, and Jonas Allerbeck. Ultrafast Plasmon-driven Charge and Spin Dynamics in Au- Ni Magnetoplasmonic Nanostructures. In *Ultrafast and Nonlinear Phenomenon in Plasmonics and Nanophotonics*, number September, pages 10–12, 2024.

[24] Jean Yves Bigot, Mircea Vomir, and Eric Beaurepaire. Coherent ultrafast magnetism induced by femtosecond laser pulses. *Nature Physics*, 5(7):515–520, 2009.

[25] Luca Guidoni, Eric Beaurepaire, and Jean-yves Bigot. Magneto-optics in the Ultrafast Regime : Thermalization of Spin Populations in Ferromagnetic Films. *Physical Review Letters*, 89(1):1–4, 2002.

[26] P M Oppeneer and A Liebsch. Ultrafast demagnetization in Ni : theory of magneto-optics for non-equilibrium electron. *Physics condensed matter*, 16:5519–5530, 2004.

[27] A. Litvinenko, R. Khymyn, V. Tyberkevych, V. Tikhonov, A. Slavin, and S. Nikitov. Tunable Magnetoacoustic Oscillator with Low Phase Noise. *Physical Review Applied*, 15(3):1, 2021.

[28] Wei Gang Yang and Holger Schmidt. Acoustic control of magnetism toward energy-efficient applications. *Applied Physics Reviews*, 8(2), 2021.

[29] Donna Strickland and Gerard Mourou. Compression of amplified chirped optical pulses. *Optics Communications*, 56(3):219–221, 1985.

[30] J. Lloyd-Hughes, P. M. Oppeneer, T. Pereira Dos Santos, A. Schleife, S. Meng, M. A. Sentef, M. Ruggenthaler, A. Rubio, I. Radu, M. Murnane, X. Shi, H. Kapteyn, B. Stadtmüller, K. M. Dani, F. H. Da Jornada, E. Prinz, M. Aeschlimann, R. L. Milot, M. Burdanova, J. Boland, T. Cocker, and F. Hegmann. The 2021 ultrafast spectroscopic probes of condensed matter roadmap. *Journal of Physics Condensed Matter*, 33(35), 2021.

[31] Thomas Elsaesser. Introduction: Ultrafast Processes in Chemistry. *Chemical Reviews*, 117(16):10621–10622, 2017.

[32] Bart G. Borghuis, Duje Tadin, Martin J.M. Lankheet, Joseph S. Lappin, and Wim A. van de Grind. Temporal limits of visual motion processing: Psychophysics and neurophysiology. *Vision (Switzerland)*, 3(1), 2019.

[33] Jongchul Lim, Manuel Kober-czerny, Yen-hung Lin, James M Ball, Nobuya Sakai, Elisabeth A Duijnstee, Min Ji Hong, John G Labram, Bernard Wenger, and Henry J Snaith. Long-range charge carrier mobility in metal halide perovskite thin-films and single crystals via transient photo-conductivity. *Nature Communications*, 13(1):1–9, 2022.

[34] Ahmed H Zewail. Femtochemistry: Atomic-scale dynamics of the chemical bond. *Journal of Physical Chemistry A*, 104(24):5660–5694, 2000.

[35] M. Th Hassan, J. S. Baskin, B. Liao, and A. H. Zewail. Highoral-resolution electron microscopy for imaging ultrafast electron dynamics. *Nature Photonics*, 11(7):425–430, 2017.

[36] T. Abraham, H.; Lemoine. Disparition instantanée du phénomène de Kerr. *Compt. Rend*, 129(206), 1899.

[37] Yuan Zhang, Junfeng Dai, Xiangli Zhong, Dongwen Zhang, Gaokuo Zhong, and Jiangyu Li. Probing Ultrafast Dynamics of Ferroelectrics by Time-Resolved Pump-Probe Spectroscopy. *Advanced Science*, 8(22):1–18, 2021.

[38] Rohit P Prasankumar; Antoinette J Taylor. *Optical techniques for solid-state materials characterization.* CRC Press, 2012.

[39] Margherita Maiuri, Marco Garavelli, and Giulio Cerullo. Ultrafast Spectroscopy: State of the Art and Open Challenges. *Journal of the American Chemical Society*, 142(1):3–15, 2020.

[40] Sterling Backus, Charles G. Durfee, Margaret M. Murnane, and Henry C. Kapteyn. High power ultrafast lasers. *Review of Scientific Instruments*, 69(3):1207–1223, 1998.

[41] Peter J. Delfyett, Dimitrios Mandridis, Mohammad Umar Piracha, Dat Nguyen, Kyungbum Kim, and Shinwook Lee. Chirped pulse laser sources and applications. *Progress in Quantum Electronics*, 36(4-6):475–540, 2012.

[42] Andrea Rossetti. *Development of an ultrafast scanning tunnelling microscope*. PhD thesis, University of Luxembourg, 2024.

[43] Jesse W Wilson, Francisco E Robles, and Warren S Warren. Invited Review Article: Pump-probe microscopy. *Review of Scientific Instruments*, 031101(March 2015):21, 2016.

[44] M. C. Velsink, M. Illienko, P. Sudera, and S. Witte. Optimizing pump-probe reflectivity measurements of ultrafast photoacoustics with modulated asynchronous optical sampling. *Review of Scientific Instruments*, 94(10), 2023.

[45] Robert W. Boyd. The nonlinear optical susceptibility - Chapter 1. In *Nonlinear Optics*, number 1941, pages 1–67. 1961.

[46] Richard L Sutherland, Daniel G Mclean, and Sean Kirkpatrick. *Handbook of Nonlinear Optics*. 2003.

[47] Alexander Grupp, Arne Budweg, Marco P. Fischer, Jonas Allerbeck, Giancarlo Soavi, Alfred Leitenstorfer, and Daniele Brida. Broadly tunable ultrafast pump-probe system operating at multi-kHz repetition rate. *Journal of Optics (United Kingdom)*, 20(1), 2018.

[48] Vytautas Jukna Alex Risos Robertas Grigutis, Gintaras Tamošauskas and Audrius Dubietis. Supercontinuum generation and optical damage of sapphire and YAG at high repetition rates. *Optics Letters*, 45(16):4507–4510, 2020.

[49] Werner Lauterborn and Thomas Kurz. *Ultrafast Optics*. 2003.

[50] Giordmaine J A and Miller R C. Tunable coherent parametric oscillation in LiNbO3 at optical frequencies. *Physical Review Letters*, 14(24), 1965.

[51] Richard A. Baumgartner and Robert K. Byer. Optical Parametric Amplification. *IEEE Journal of Quantum Electronics*, 15(6):432–444, 1979.

[52] D. Brida, C. Manzoni, G. Cirmi, M. Marangoni, S. Bonora, P. Villoresi, S. De Silvestri, and G. Cerullo. Few-optical-cycle pulses tunable from the visible to the mid-infrared by optical parametric amplifiers. *Journal of Optics A: Pure and Applied Optics*, 12(1), 2010.

[53] C. Manzoni and G. Cerullo. Design criteria for ultrafast optical parametric amplifiers. *Journal of Optics (United Kingdom)*, 18(10), 2016.

[54] Giulio Cerullo, Cristian Manzoni, Larry Lüer, and Dario Polli. Time-resolved methods in biophysics. 4. Bbroadband pump–probe spectroscopy system with sub-20 fs temporal resolution for the study of energy transfer processes in photosynthesis. *Photochemical and Photobiological Sciences*, 6(2):135–144, 2007.

[55] D. Eimerl, L. Davis, S. Velsko, E. K. Graham, and A. Zalkin. Optical, mechanical, and thermal properties of barium borate. *Journal of Applied Physics*, 62(5):1968–1983, 1987.

[56] D. J. Armstrong, W. J. Alford, T. D. Raymond, and A. V. Smith. Absolute measurement of the effective nonlinearities of KTP and BBO crystals by optical parametric amplification. *Applied Optics*, 35(12):2032, 1996.

[57] Thomas Deckert, Aline Vanderhaegen, and Daniele Brida. Sub-8-fs pulses in the visible to near-infrared by a degenerate optical parametric amplifier. *Optics Letters*, 48(17):4496, 2023.

[58] Thomas Deckert. *Ultrafast exciton and free charge carrier dynamics in condensed matter studied by multidimensional spectroscopy.* PhD thesis, University of Luxembourg, 2024.

[59] Pavel Varlamov, Jan Marx, Yoav Urbina Elgueta, Andreas Ostendorf, Ji Wan Kim, Paolo Vavassori, and Vasily Temnov. Femtosecond Laser Ablation and Delamination of Functional Magnetic Multilayers at the Nanoscale. *Nanomaterials*, 14(18):1–13, 2024.

[60] Antonia Ghita, Tudor Gabriel Mocioi, Alexey M. Lomonosov, Jiwan Kim, Oleksandr Kovalenko, Paolo Vavassori, and Vasily V. Temnov. Anatomy of ultrafast quantitative magnetoacoustics in freestanding nickel thin films. *Physical Review B*, 107(13), 2023.

[61] Ji Wan Kim, Mircea Vomir, and Jean Yves Bigot. Ultrafast magnetoacoustics in nickel films. *Physical Review Letters*, 109(16):1–5, 2012.

[62] T. J. Grimsley, F. Yang, S. Che, G. A. Antonelli, H. J. Maris, and A. V. Nurmikko. Ultrafast opto-acoustics applied to the study of material nanostructures. *Journal of Physics: Conference Series*, 278(1), 2011.

[63] Guanhao Huang, Alberto Beccari, Nils J. Engelsen, and Tobias J. Kippenberg. Room-temperature quantum optomechanics using an ultralow noise cavity. *Nature*, 626(7999):512–516, 2024.

[64] S. Maekawa J. Puebla, Y. Hwang and Y. Otani. Perspectives on spintronics with surface acoustic waves. *Applied Physics Letters*, 120(22), 2022.

[65] Y. Tsaturyan, A. Barg, E. S. Polzik, and A. Schliesser. Ultracoherent nanomechanical resonators via soft clamping and dissipation dilution. *Nature Nanotechnology*, 12(8):776–783, 2017.

[66] Ji Wan Kim and Jean Yves Bigot. Magnetization precession induced by picosecond acoustic pulses in a freestanding film acting as an acoustic cavity. *Physical Review B*, 95(14):1–6, 2017.

[67] Joel Kuttruff, Denis Garoli, Jonas Allerbeck, Roman Krahne, Antonio De Luca, Daniele Brida, Vincenzo Caligiuri, and Nicolò Maccaferri. Ultrafast all-optical switching enabled by epsilon-near-zero-tailored absorption in metal-insulator nanocavities. *Communications Physics*, 3(1):1–7, 2020.

[68] Yu E. Lozovik and V. A. Sharapov. Excitation of coherent acoustic phonons by a femtosecond pulse. *Physics of the Solid State*, 45(5):969–971, 2003.

[69] Vasily V. Temnov, Alexandr Alekhin, Andrey Samokhvalov, Dmitry S. Ivanov, Alexey Lomonosov, Paolo Vavassori, Evgeny Modin, and Vadim P. Veiko. Nondestructive femtosecond laser lithography of Ni nanocavities by controlled thermo-mechanical spallation at the nanoscale. *Nano Letters*, 20(11):7912–7918, 2020.

[70] S. Nolte F. von Alvensleben A. Tunnermann B.N. Chicbkov, C. Momma. Femtosecond, picosecond and nanosecond laser ablation of solids. *Applied Physics A*, 63:109–115, 1996.

[71] Francesco Ruffino and Maria Grazia Grimaldi. Nanostructuration of thin metal films by pulsed laser irradiations: A review. *Nanomaterials*, 9(8), 2019.

[72] Jay A. Fox and Dallas N. Barr. Laser-induced shock effects in Plexiglas and 6061-T6 aluminum. *Applied Physics Letters*, 22(11):594–596, 1973.

[73] Alba Viejo Rodríguez, Andrea Rossetti, Marco Gandolfi, Yoav Urbina Elgueta, Evgeny B. Modin, Svetlana Starikovskaia, Tat Loon Chng, Vasily V. Temnov, Maria Antonietta Vincenti, Daniele Brida, Paolo Vavassori, and Nicolò Maccaferri. Anomalous frequency scaling of acoustic phonon damping in freestanding nickel cavities fabricated via laser delamination. *Applied Physics Letters*, 127(7), 2025.

[74] M L Williams. *CRC Handbook of Chemistry and Physics, 84th edition.* 0.

[75] Yûetsu Murakami Michio Kikuchi Hakaru Masumoto, Hideo Saitô. Crystal Anisotropy and Temperature Dependence of Young'S Modulus in Single Crystal of Nickel. *Japan Inst Metals-Trans*, 10(2):119–123, 1969.

[76] Marco Gandolfi, Maria Eugenia Serrano Flores, Jesse Frantz, Jason Myers, Robel Bekele, Jas Sanghera, Anthony Clabeau, Natalia M. Litchinitser, and Maria Antonietta Vincenti. Dynamic light-driven metasurface: Harnessing quasibound states in the continuum for laser-induced selective crystallization. *Physical Review A*, 110(1):1–10, 2024.

[77] L.D. Landau and E.M. Lifshitz. *Theory of Elasticity, Volume 7.* 1986.

[78] Giulio Benetti, Marco Gandolfi, Margriet J. Van Bael, Luca Gavioli, Claudio Giannetti, Claudia Caddeo, and Francesco Banfi. Photoacoustic Sensing of Trapped Fluids in Nanoporous Thin Films: Device Engineering and Sensing Scheme. *ACS Applied Materials and Interfaces*, 10(33):27947–27954, 2018.

[79] Kuan Yu Chou, Chen Ling Wu, Chih Chiang Shen, Jinn Kong Sheu, and Chi Kuang Sun. Terahertz Photoacoustic Generation Using Ultrathin Nickel Nanofilms. *Journal of Physical Chemistry C*, 125(5):3134–3142, 2021.

[80] Vasily V. Temnov, Ilya Razdolski, Thomas Pezeril, Denys Makarov, Denis Seletskiy, Alexey Melnikov, and Keith A. Nelson. Towards the nonlinear acousto-magneto-plasmonics. *Journal of Optics (United Kingdom)*, 18(9):1–19, 2016.

[81] Yu Zhou, Yupeng Zheng, Qinwen Xu, Yuanhang Qu, Yuqi Ren, Xiaoming Huang, Chao Gao, Yan Liu, Shishang Guo, Yao Cai, and Chengliang Sun. Design and Fabrication of 3.5 GHz Band-Pass Film Bulk Acoustic Resonator Filter. *Micromachines*, 15(5):1–10, 2024.

[82] Alexey Kimel, Anatoly Zvezdin, Sangeeta Sharma, Samuel Shallcross, Nuno De Sousa, Antonio García-martín, Georgeta Salvan, and Jaroslav Hamrle. The 2022 magneto-optics roadmap. *Journal of Physics D: Applied Physics*, 55:64, 2022.

[83] Soham Saha, Benjamin T. Diroll, Joshua Shank, Zhaxylyk Kudyshev, Aveek Dutta, Sarah Nahar Chowdhury, Ting Shan Luk, Salvatore Campione, Richard D. Schaller, Vladimir M. Shalaev, Alexandra Boltasseva, and Michael G. Wood. Broadband, High-Speed, and Large-Amplitude Dynamic Optical Switching with Yttrium-Doped Cadmium Oxide. *Advanced Functional Materials*, 30(7):1–7, 2020.

[84] Vincenzo Caligiuri, Milan Palei, Giulia Biffi, Sergey Artyukhin, and Roman Krahne. A Semi-Classical View on Epsilon-Near-Zero Resonant Tunneling Modes in Metal/Insulator/Metal Nanocavities. *Nano Letters*, 19(5):3151–3160, 2019.

[85] Jongbum Kim, Enrico G. Carnemolla, Clayton DeVault, Amr M. Shaltout, Daniele Faccio, Vladimir M. Shalaev, Alexander V. Kildishev, Marcello Ferrera, and Alexandra Boltasseva. Dynamic Control of Nanocavities with Tunable Metal Oxides. *Nano Letters*, 18(2):740–746, 2018.

[86] J G Baker, K Freeman, G Warner, and ... *Handbook of the physicochemical properties of the elements*. 1968.

[87] L. Zhang and A. Chopelas. Sound velocity of Al2O3 to 616 kbar. *Physics of the Earth and Planetary Interiors*, 87(1-2):77–83, 1994.

[88] Laura Restrepo-Pérez, Chirlmin Joo, and Cees Dekker. Paving the way to single-molecule protein sequencing. *Nature Nanotechnology*, 13(9):786–796, 2018.

[89] Francesco Mazza and Dirk Van Den Bekerom. An ultrafast algorithm for ultrafast time-resolved coherent Raman spectroscopy. *Communications Chemistry*, pages 1–9, 2025.

[90] Denis Garoli, Hirohito Yamazaki, Nicolò Maccaferri, and Meni Wanunu. Plasmonic Nanopores for Single-Molecule Detection and Manipulation: Toward Sequencing Applications. *Nano Letters*, 19(11):7553–7562, 2019.

[91] Liang Xue, Hirohito Yamazaki, Ren Ren, Meni Wanunu, Aleksandar P. Ivanov, and Joshua B. Edel. Solid-state nanopore sensors. *Nature Reviews Materials*, 5(12):931–951, 2020.

[92] Reinhard J. Maurer, Christoph Freysoldt, Anthony M. Reilly, Jan Gerit Brandenburg, Oliver T. Hofmann, Torbjörn Björkman, Sébastien Lebègue, and Alexandre Tkatchenko. Advances in Density-Functional Calculations for Materials Modeling. *Annual Review of Materials Research*, 49:1–30, 2019.

[93] Nicolò Maccaferri, Paolo Vavassori, and Denis Garoli. Magnetic control of particle trapping in a hybrid plasmonic nanopore. *Applied Physics Letters*, 118(19), 2021.

[94] Francesca Madonini and Federica Villa. Single photon avalanche diode arrays for time-resolved raman spectroscopy. *Sensors*, 21(13), 2021.

[95] Piero Lafiosca, Luca Nicoli, Luca Bonatti, Tommaso Giovannini, Stefano Corni, and Chiara Cappelli. QM/Classical Modeling of Surface Enhanced Raman Scattering Based on Atomistic Electromagnetic Models. *Journal of Chemical Theory and Computation*, 19(12):3616–3633, 2023.

[96] K Bhandari and Nick Goldman. A generalized protein identification method for novel and diverse sequencing technologies. *NAR Genomics and Bioinformatics*, (v):1–11, 2024.

[97] Jannis Weinacker, Sebastian Kalt, Pascal Kiefer, Pascal Rietz, and Martin Wegener. On Iterative Pre-Compensation of 3D Laser-Printed Micro-Optical Components Using Confocal-Optical Microscopy. *Advanced Functional Materials*, 34(12):1–12, 2024.

[98] Xianli Wang, Chuanzhen Hu, Kaiqin Chu, and Zachary J. Smith. Low resolution Raman: The impact of spectral resolution on limit of detection and imaging speed in hyperspectral imaging. *Analyst*, 145(20):6607–6616, 2020.

[99] S. Jarmelo, P. R. Carey, and R. Fausto. The Raman spectra of serine and 3,3-dideutero-serine in aqueous solution. *Vibrational Spectroscopy*, 43(1):104–110, 2007.

[100] Sofía Rodríguez. Redefining Microfabrication of High-Precision Optics. *PhotonicsViews*, 2020.

[101] R. Ferrini T. Aderneuer, O. Fernández. Two-photon grayscale lithography for free-form micro-optical arrays. *Optics Express*, 29(24):39511–39520, 2021.

[102] H. Giessen L. Siegle, S. Ristok. Complex aspherical singlet and doublet microoptics by grayscale 3D printing. *Optics Express*, 31(3):4179–4189, 2023.

[103] Jannis Weinacker, Bikash Kumar Bhandari, Alba Viejo Rodriguez, Charlotte West, Francesco De Angelis, Francesco Tantussi, Nicolò Maccaferri, Nick Goldman, and Martin Wegener. A Protocol Using Compact 3D Printed Micro-Optical Elements for Protein Identification from Low-Intensity Amino-Acid Raman Signals. *Advanced Materials Technologies*, 2401876:1–7, 2025.

[104] Jannis Weinacker. *Micro-Optical Elements used for Single-Molecule Raman Spectroscopy and as Scintillators*. PhD thesis, Karlsruhe Institute of Technology, 2024.

[105] Shivam Mahajan and Massimo P. Ciamarra. Quasi-localized vibrational modes, boson peak and sound attenuation in model mass-spring networks. *SciPost Physics*, 15(2):1–17, 2023.

[106] J. A. Krumhansl and J. A.D. Matthew. Scattering of long-wavelength phonons by point imperfections in crystals. *Physical Review*, 140(5A):1812–1817, 1965.

[107] M. van Kampen, C. Jozsa, J. T. Kohlhepp, P. LeClair, L. Lagae, W. J.M. de Jonge, and B. Koopmans. All-optical probe of coherent spin waves. *Physical Review Letters*, 88(22):1–227201, 2002.

Copyrights and permissions

1. Reuse and reprint of figure 3.5

   License number: 1663499-1

   ISSN: 2040-8986

   License date: 20-Oct-2025

   Licensed content Publication: Journal of Optics [47]

   Rightsholder : IOP Publishing Limited

   Type of use: Thesis/dissertation

   Format of reuse: Print and electronic

   Institution name: University of Luxembourg

2. Reuse and reprint of figure 4.1 (a) and (b)

   License number: 6133000305604

   License date: 20-Oct-2025

   Licensed Content Publication: Nano Letters [69]

   Licensed Content Publisher : American Chemical Society

   Type of use: Thesis/dissertation

   Format of reuse: Print and electronic

   Institution name: University of Luxembourg